Quantum Dynamics in Rugged Energy Landscapes, and Additional Topics in Disordered Systems

Christopher L. Baldwin

A dissertation
submitted in partial fulfillment of the
requirements for the degree of
Doctor of Philosophy

University of Washington
2018

Reading Committee:
Christopher Laumann, Chair
Boris Spivak
Andreas Karch

Program Authorized to Offer Degree:
Physics

University of Washington

Abstract

Quantum Dynamics in Rugged Energy Landscapes,
and Additional Topics in Disordered Systems

Christopher L. Baldwin

Chair of the Supervisory Committee:
Christopher Laumann
Department of Physics

This thesis concerns the interplay of quantum mechanics with strong disorder, and the novel dynamical phases that are unique to disordered quantum systems. The results that we present apply to systems ranging from spin glasses to granular superconductors to quantum-computational problems.

In the first part, we discuss the isolated quantum dynamics of mean-field spin glass models, using the random energy and p-spin models in a transverse field as tractable examples. We show that the low-energy configurations are organized into clusters separated by macroscopic Hamming distances, and that the tunneling amplitudes between clusters are exponentially suppressed. As a result, we find three distinct dynamical phases. At small transverse field, the system remains trapped within its starting cluster (trapped phase). At intermediate transverse field, the system tunnels between clusters (tunneling phase). At large transverse field, the system is excited out of clusters (excitation phase). We describe the similarities and differences between the trapped phase and a many-body localized phase. We also discuss at length the implications for quantum-computational approaches to "matching" problems, in which one solution to a computational problem is used as a starting point to find others. Only in the tunneling phase can quantum dynamics solve the matching problem. Although necessarily exponentially slow in system size, it may be exponentially faster than simple classical algorithms.

In the second part, we discuss interfering directed paths in disordered media. Important physical realizations are hopping conduction in semiconductors, spin glasses at high temperature, and granular D-wave superconductors. Sign order, defined as the directed path sum having greater probability of being positive than negative at large distance, is a characterization of the role of interference with implications for the response of systems to a magnetic field. We show that path sums are necessarily sign-disordered in two dimensions but may be sign-ordered in three dimensions. Building on this result, we study the behavior of granular D-wave superconductors and show that the superconductivity is enhanced by a magnetic field, even beyond the directed-path regime.

Contents

Acknowledgements

Full confession: I think of the PhD itself as largely a formality. What really matters to me is the things I have learned and the friends I have made over the past five years. They are the ones who have made all this worthwhile.

First and foremost, I want to thank my advisor, Chris Laumann. When I started the PhD, I felt like I was already pretty good at learning from a textbook and doing calculations, but I knew nothing about how to think like a physicist, not even enough to realize how little I knew. I wouldn't presume to claim that I have since figured everything out (I haven't), but I do notice a huge difference in how I now approach problems: I have some intuition to rely on, I am able to consolidate new ideas with my existing knowledge, and I can parse technical research results. All of this, I owe to Chris. Throughout my PhD, he has been willing and able to discuss just about anything I wanted to learn, and has been engaged with my work while still giving me enough space to play with it. Over time, with Chris always there to rely on, things just started to click. I count myself very lucky for having gotten the opportunity to work with him.

I also want to thank all the other physics professors who have helped me along, both in coursework and in just discussing physics. In particular, Boris Spivak has taught me a tremendous amount and been a great person to work with. I also gained a lot of perspective (and enjoyment) from many conversations with the CMT faculty in Boston, especially Anushya, Pankaj, and Anatoli.

Of course, I want to thank my friends throughout the years, both in Seattle and Boston: Adam, Tyson, Paul, Steve, Michelle, Phil, Marin, Rajita, Tamiro, Kaitlyn, Michael, Pranay, and many other people. I've really enjoyed our time together, whether spent rock climbing, hiking, playing board games, taking advantage of MoviePass, trying to be Bruno Mars, cheering with (and then consoling) British expats during the World Cup, or just hanging out. I would say that their support helped me through my PhD, and that would be true, but it would be missing the point. My time with my friends is what really matters, and I value that time with them for its own sake, regardless of any PhD.

Finally, I want to thank my parents. I can say without exaggeration: I would not be where I am were it not for their constant love and encouragement, and I am sure that will continue to be true wherever I go from here.

Part I

Quantum dynamics in rugged energy landscapes

Chapter 1

Introduction

Within the past three decades, no less than four sets of Nobel Prizes in physics have been awarded for the development of experimental techniques to isolate and manipulate microscopic quantum matter [1–4]. Understandably, these powerful experimental methods have reinvigorated interest in the theory of non-equilibrium Hamiltonian dynamics. The systems being studied often either are interacting spins or can be modelled as effective spin degrees of freedom [5–10]. Part 1 of this thesis explores the effects of static disorder on the quantum dynamics of isolated spin systems. By "static disorder" we mean local fields and/or interactions which vary erratically in space. A variety of novel non-equilibrium phenomena emerge under such conditions which cannot be understood through the phenomenology of clean (i.e., disorderless) systems and challenge traditional notions of equilibration. The present chapter introduces essential concepts, motivates the precise questions under consideration, and states the main results.

1.1 Thermalization in closed quantum systems

1.1.1 The eigenstate thermalization hypothesis

A natural question to ask about an isolated system is if the dynamics of the system brings it to internal equilibrium. One has an observable of interest A and wants to know if the value seen at late times agrees with the microcanonical average up to small fluctuations. This thesis will focus on systems evolving under quantum Hamiltonian dynamics, and so we use the following precise formulation. Denote the number of degrees of freedom by N, the Hamiltonian by $\hat{H}$, the state of the system by $|\Psi(t)\rangle$, and the average energy by E (independent of time for an isolated system). We say that equilibration, or "thermalization", occurs if

$$\lim_{\tau\to\infty}\frac{1}{\tau}\int_0^\tau \mathrm{d}t\ \langle\Psi(t)|\hat{A}|\Psi(t)\rangle = \mathrm{Tr}\big[\hat{A}\,\hat{\rho}_{\mathrm{micro}}(E)\big] \equiv A_{\mathrm{eq}}(E), \tag{1.1}$$

$$\lim_{\tau\to\infty}\frac{1}{\tau}\int_0^\tau \mathrm{d}t\ \langle\Psi(t)|(\hat{A}-A_{\mathrm{eq}})^2|\Psi(t)\rangle = O\big(N^{-1}\big). \tag{1.2}$$

In Eq. (1.1), $\hat{\rho}_{\mathrm{micro}}(E)$ is the microcanonical density matrix: it projects uniformly onto those eigenstates with energies in a small window around E.

Eqs. (1.1) and (1.2) are certainly not true for every system which one could consider: non-interacting systems are a trivial example, and those described in Sec. 1.2 are a highly non-trivial one. Nevertheless, the right-hand sides of the equations have been remarkably successful in describing the macroscopic world, so we expect them to hold for typical interacting many-body Hamiltonians. A reasonably generic *ansatz* from which one can derive Eqs. (1.1) and (1.2) is the Eigenstate Thermalization Hypothesis (ETH) [11–13]. In words, the ETH consists of two assertions about the eigenstates of the Hamiltonian: 1) the expectation values of observables in an individual eigenstate are equal to the equilibrium values, and 2) the off-diagonal matrix elements of observables are of comparable scale for all eigenstates. The precise mathematical statement is that for any (local) observable $\hat{A}$,

$$\langle m|\hat{A}|n\rangle = A_{\mathrm{eq}}(\epsilon)\delta_{mn} + \frac{R_{mn}}{e^{Ns(\epsilon)/2}}f(\epsilon,\omega), \tag{1.3}$$

where $|m\rangle$ and $|n\rangle$ are eigenstates with energies $N\epsilon_m$ and $N\epsilon_n$ (i.e., ϵ_m and ϵ_n are energy densities). We define $\epsilon \equiv (\epsilon_m+\epsilon_n)/2$ and $\omega \equiv N\epsilon_m - N\epsilon_n$ for convenience.

The first term in Eq. (1.3) constitutes assertion 1, and the second constitutes assertion 2. $s(\epsilon)$ is the thermodynamic entropy density, and the factor $e^{-Ns(\epsilon)/2}$ can be thought of as a normalization to ensure that $\hat{A}^2$, $\hat{A}^3$, etc. obey their own forms of Eq. (1.3) (required for consistency of the ansatz) [14]. Note that the normalization is independent of the specific eigenstates other than through the entropy density at the energy in question. R_{mn} does vary erratically between eigenstates, but it is assumed to be $O(1)$ with respect to N, unlike the normalization. Finally, $f(\epsilon,\omega)$ is a smooth $O(1)$ function to be discussed momentarily.

Since all eigenstates near a given energy have the same expectation value $\langle\hat{A}\rangle$, Eq. (1.1) follows quite naturally, *irrespective of initial condition*. The only assumption we make is that the standard deviation of $\hat{H}$ in the initial state $|\Psi(0)\rangle$ is much smaller than N, i.e., the quantum fluctuations in the energy density are small[1]. Expand $|\Psi(0)\rangle$ in the eigenstate basis as

$$|\Psi(0)\rangle = \sum_n c_n\,|n\rangle\,, \tag{1.4}$$

where c_n is vanishingly small if $\epsilon_n \neq \epsilon$ but is otherwise arbitrary. Then, using

[1] If the quantum fluctuations in the energy density are not small, then clearly the microcanonical ensemble is not a reasonable description of the system. The restriction to initial states with well-defined energy density is not a limitation of the ETH but rather a requirement for posing the original question of equilibration.

Eq. (1.3),

$$\lim_{\tau\to\infty}\frac{1}{\tau}\int_0^\tau \mathrm{d}t\ \langle\Psi(t)|\hat{A}|\Psi(t)\rangle = \lim_{\tau\to\infty}\frac{1}{\tau}\int_0^\tau \mathrm{d}t\ \sum_{mn} e^{-i(E_n-E_m)t}c_m^* c_n\ \langle m|A|n\rangle$$
$$= \sum_n |c_n|^2\ \langle n|A|n\rangle = \sum_n |c_n|^2 A_{\mathrm{eq}}(\epsilon) = A_{\mathrm{eq}}(\epsilon), \tag{1.5}$$

as claimed. If a quantum system obeys the ETH, then it thermalizes regardless of initial state. The derivation of Eq. (1.2), stating that fluctuations around the equilibrium value are small, is similarly straightforward. One further finds that $|f(\epsilon,\omega)|^2$ is simply the Fourier transform of the autocorrelation function $\langle\hat{A}(t)\hat{A}(0)\rangle$, i.e., $f(\epsilon,\omega)$ describes how $A(t)$ approaches the equilibrium value [15].

It may appear that the ETH is too restrictive an ansatz to apply to real systems: the statement that *every* eigenstate gives the same expectation values may seem to contradict the wide variety of non-equilibrium states observed in nature. Yet keep in mind that the many-body eigenstates of strongly interacting Hamiltonians are complex, highly entangled states. The states which we are familiar with and can access experimentally much more closely resemble product states, superposed from exponentially many eigenstates, and so we can observe numerous non-equilibrium states even if the underlying eigenstates obey the ETH. Indeed, the ETH has been confirmed numerically in many systems, including those of spins, fermions, and bosons (hard- and soft-core) [16–21].

1.1.2 Random matrix statistics

Random matrix theory offers a complementary perspective on strongly interacting many-body systems. Unlike the ETH, it characterizes the correlations among energy levels as opposed to the behavior of observables. Although random matrix theory does not describe thermalization directly, it has close connections and often serves as a useful diagnostic for distinguishing chaotic from non-chaotic dynamics[2].

The use of random matrix theory in physics began with attempts to describe the energy levels of nuclei, in particular quantities such as the distribution of gaps between neighboring levels (called "level spacings"). An immediate obstacle is that one does not know the Hamiltonian for nucleons in a nucleus, and even if one did, the problem would certainly be too complicated to solve in full detail. This motivates a statistical approach to the problem, analogous to statistical mechanics: consider instead an ensemble of random Hamiltonians, and hope that the ensemble average for quantities of interest agrees with the values for the real system [22]. The simplest example is the Gaussian Orthogonal Ensemble (GOE), in which every element H_{ij} of the random Hamiltonian is a

[2]The notion of chaos in quantum systems is subtle and distinct from classical chaos. For this thesis, however, we will be content to use random matrix statistics merely as a sharp indicator of different dynamical phases.

Gaussian-distributed real random variable:

$$P(H_{ii}) = \frac{1}{\sqrt{\pi}} e^{-H_{ii}^2}, \quad P(H_{ij} = H_{ji}) = \sqrt{\frac{2}{\pi}} e^{-2H_{ij}^2}. \tag{1.6}$$

See Ref. [22] for many more details. Remarkably, it was discovered that the distribution of level spacings in the GOE agrees quite well with the experimental data on real nuclei, validating the statistical approach [23].

Keep in mind that Eq. (1.6) is not intended to be an accurate model of the nuclear Hamiltonian. The philosophy is rather that local properties of the spectrum, such as the level spacing distribution and the correlation function between nearby levels, are insensitive to details of specific matrix elements and thus can be inferred from the relatively simple GOE. Many properties of real systems have been calculated in this manner [24–27].

The relevance of random matrix theory is not limited to nuclear physics. GOE statistics have been observed in a wide range of many-body Hamiltonians, particularly in interacting spin systems [28–30] and particles on a lattice [31–33]. Other ensembles of random matrices are possible as well. One common alternative is Poisson level statistics, in which the eigenvalues are distributed independently (as opposed to the underlying matrix elements of the Hamiltonian). Whereas the level spacings in the GOE are distributed to good approximation as [22]

$$P_{\mathrm{GOE}}(s) = \frac{\pi}{2} s\, e^{-\frac{\pi}{4}s^2}, \tag{1.7}$$

where s is the spacing normalized by the mean, the Poisson distribution is instead

$$P_{\mathrm{Pois}}(s) = e^{-s}. \tag{1.8}$$

The difference between the two is stark. $P_{\mathrm{Pois}}(s)$ is finite at small spacings and decays exponentially, while $P_{\mathrm{GOE}}(s)$ vanishes at small spacings and decays much faster at large spacings.

Not only have both distributions been observed in many-body systems, but there can be transitions from one to the other as parameters of the model vary. In all the cases known thus far, the transition coincides with a change from dynamics that leads to thermalization to dynamics that does not (discussed further below). Level spacing statistics serve as an order parameter for distinguishing the different dynamical phases, with GOE statistics corresponding to thermalization and Poisson statistics to the absence. We shall use them as such in what follows.

1.2 Many-body localization

1.2.1 Non-interacting particles

Perhaps counterintuitively, disorder can be a major impediment to thermalization. The phenomenon of "localization" is a dramatic example. Randomness in the potential that a quantum particle feels can localize the particle in space

and completely prevent transport, even without any barriers to confine the particle [34–36].

The simplest context in which to study localization is a single particle hopping on a lattice, e.g., to model an electron hopping between impurity states of a doped semiconductor [37, 38]:

$$H = \sum_i \epsilon_i \left|i\right\rangle \left\langle i\right| - \gamma \sum_{\langle ij \rangle} \left(\left|i\right\rangle \left\langle j\right| + \left|j\right\rangle \left\langle i\right| \right), \tag{1.9}$$

where i and j label sites of the lattice and $\langle ij \rangle$ refers to neighboring sites. The on-site potential ϵ_i is taken to be a random variable, often uniformly distributed in $[-W, W]$ independently for each site. The choice to treat ϵ_i as random is not as artificial as it may seem. In the context of hopping conduction, for example, different impurities may have offset energy levels due to differences in their local environments.

First, however, let us consider two special cases (in 1D for simplicity). Suppose that $\epsilon_0 = -W$ while all other $\epsilon_i = 0$. Site 0 constitutes a potential well, and one knows from elementary quantum mechanics that the bound state in the well has exponentially decaying tails. One can be more concrete in the $\gamma \ll W$ limit by using perturbation theory. As discussed in detail in the body of the thesis, the expansion of the bound state $\left|\phi_0\right\rangle$ takes the form

$$\left|\phi_0\right\rangle = \left(1 + \dots\right)\left|0\right\rangle + \left(\frac{\gamma}{W} + \dots\right)\left|1\right\rangle + \left(\left(\frac{\gamma}{W}\right)^2 + \dots\right)\left|2\right\rangle + \dots, \tag{1.10}$$

where the ellipses denote higher powers of γ. To leading order, the wavefunction amplitude on site j is

$$\left\langle j|\phi_0\right\rangle = \left(\frac{\gamma}{W}\right)^{|j|} = e^{-\frac{|j|}{\xi}}, \tag{1.11}$$

where the localization length is $\xi \equiv (\ln W/\gamma)^{-1}$. Eq. (1.11) is a trivial example of a localized wavefunction. Realistic localized states have more complicated structure, but remain characterized by an exponentially decaying envelope.

Now suppose that every l^{th} site has potential $-W$ as well, i.e., $\epsilon_{nl} = -W$ for $n \in \mathbb{Z}$ while $\epsilon_i = 0$ otherwise. In this case, one knows that the states inside the wells form Bloch waves:

$$\left\langle j|\phi_k\right\rangle = e^{ikj} u_k(j), \tag{1.12}$$

where k is defined up to $2\pi/l$ and $u_k(j)$ is periodic in steps of l. Eq. (1.12) is an example of an extended wavefunction, and it holds *regardless of* γ *and* l. $|\left\langle j|\phi_k\right\rangle|^2$ may be very small in between wells but it does not decay as $|j| \to \infty$, even for arbitrarily weak hopping and distant wells.

Random potentials are much more subtle. On the one hand, they are not periodic and therefore Bloch's theorem does not apply. On the other hand, there exist sites with energies arbitrary close to a given one, and so the concept of isolated wells does not strictly apply either. The study of eigenstates in random potentials is accordingly more complicated, but by now there are ample

results, both analytical [38–40], numerical [41–45], and experimental [46–48]. It is well-established that states are localized in low dimensions or at small hopping, and are extended in high dimensions at large hopping. To heuristically understand localization, note that one must look to larger distances to find sites with energies closer to a given one: if $\epsilon_0 = -W$, the smallest energy within distance 1 is on average $-W/3$, the smallest within distance 2 is $-3W/5$, within distance 3 is $-5W/7$, and so on. Longer-distance jumps have smaller transition amplitudes since the particle must tunnel through the intermediate sites, and so it is possible for the transition amplitudes to be smaller than the energy differences at all distances. In this event, the wavefunctions are localized.

As mentioned above, localized states in a random potential do not have the simple form of Eq. (1.11), but they are bounded by an analogous expression:

$$|\phi_n(x)| \leq \frac{1}{\sqrt{\xi}} e^{-\frac{|x-n|}{\xi}}. \tag{1.13}$$

The label n indicates the localization center of the wavefunction. Although Eq. (1.13) is a statement about eigenstates of the Hamiltonian, one can directly show that initial wave packets do not spread throughout the lattice as a result. Take the initial state to be $|\psi(0)\rangle = |0\rangle$ for simplicity. Write

$$\begin{aligned} \langle \hat{x}(t)^2 \rangle &= \sum_{mn} \langle 0|\phi_m\rangle \langle \phi_n|0\rangle e^{-i(E_n - E_m)t} \langle \phi_m|\hat{x}^2|\phi_n\rangle \\ &= \sum_{mn}\sum_{x} e^{-i(E_n-E_m)t} x^2 \phi_m(0)\phi_m(x)^*\phi_n(0)^*\phi_n(x). \end{aligned} \tag{1.14}$$

Then, using Eq. (1.13),

$$\left| \langle \hat{x}(t)^2 \rangle \right| \leq \frac{1}{\xi^2} \sum_{mn}\sum_{x} x^2 e^{-\frac{|m|}{\xi}} e^{-\frac{|x-m|}{\xi}} e^{-\frac{|n|}{\xi}} e^{-\frac{|x-n|}{\xi}} \leq A\xi^2, \tag{1.15}$$

where A is a numerical coefficient. The width of the wave packet remains finite, even at arbitrarily late times, and thus the particle will always be observed within a distance $O(\xi)$ of its initial position. Contrast this with the behavior of a diffusive particle, for which $x^2 \sim t$.

Before moving on, let us rephrase Eq. (1.13) in language more suitable for many-body problems [49]. Eq. (1.9) for the tight-binding Hamiltonian is expressed in second quantization as

$$H = \sum_i \epsilon_i \, {c_i}^\dagger c_i - \gamma \sum_{\langle ij \rangle} \left({c_i}^\dagger c_j + {c_j}^\dagger c_i \right). \tag{1.16}$$

One can diagonalize the quadratic form through a unitary transformation U:

$$c_m = \sum_i U_{mi} c_i, \quad H = \sum_m E_m {c_m}^\dagger c_m \equiv \sum_m E_m \hat{n}_m. \tag{1.17}$$

So far this is completely general. For a localized system, we further have that

$$|U_{mi}| \leq \frac{1}{\sqrt{\xi}} e^{-\frac{|i-m|}{\xi}}. \tag{1.18}$$

One says that the Hamiltonian has been brought into diagonal form by a quasi-local transformation of the creation operators, where "quasi-local" (i.e., exponentially decaying with distance) indicates that the system is localized.

1.2.2 Interacting particles

Do interactions between localized particles modify or destabilize the behavior described above? This is the defining question of many-body localization (MBL). The MBL field has received a surge of interest over the past decade, in no small part because of modern experimental techniques for isolating and manipulating cold atomic systems. It is now clear that MBL does exist, at least for 1D interacting spin systems, as characterized by a lack of transport throughout arbitrarily long timescales. As in the non-interacting case, the evidence for MBL is both analytical [50–52], numerical [53–58], and experimental [5–7, 10].

A prototypical model for MBL is the random-field Heisenberg chain:

$$H = \sum_{i=1}^{N} \left(h_i \hat{\sigma}_i^z + J \vec{\hat{\sigma}}_i \cdot \vec{\hat{\sigma}}_i \right), \tag{1.19}$$

where $h_i \in [-W, W]$ independently. This model exhibits a transition from delocalized at small W/J to localized at large W/J [28]. The way to understand the MBL phase is analogous to Eqs. (1.17) and (1.18). There exists a *quasi-local* transformation from the "physical" spins $\hat{\sigma}_i^\alpha$ ("p-bits") to "localized" degrees of freedom $\hat{\tau}_i^\alpha$ ("l-bits"), such that the Hamiltonian is diagonal in the l-bit basis [49, 52, 59, 60]:

$$\hat{\tau}_i^\alpha = \sum_{j\beta} K^{(1)}_{i\alpha,j\beta} \hat{\sigma}_j^\beta + \sum_{j\beta,k\gamma} K^{(2)}_{i\alpha,j\beta,k\gamma} \hat{\sigma}_j^\beta \hat{\sigma}_k^\gamma + \ldots, \tag{1.20}$$

$$H = \sum_i J_i^{(1)} \hat{\tau}_i^z + \sum_{ij} J_{ij}^{(2)} \hat{\tau}_i^z \hat{\tau}_j^z + \ldots. \tag{1.21}$$

The ellipses denote higher-body terms of the same structure. Again, the defining feature of the transformation is that all coefficients are quasi-local:

$$\begin{gathered} \left| K^{(1)}_{i\alpha,j\beta} \right| \leq e^{-\frac{|i-j|}{\xi}}, \quad \left| K^{(2)}_{i\alpha,j\beta,k\gamma} \right| \leq e^{-\frac{\max[|i-j|,|j-k|,|i-k|]}{\xi}}, \quad \cdots, \\ \left| J^{(2)}_{ij} \right| \leq e^{-\frac{|i-j|}{\xi}}, \quad \left| J^{(3)}_{ijk} \right| \leq e^{-\frac{\max[|i-j|,|j-k|,|i-k|]}{\xi}} \quad \cdots. \end{gathered} \tag{1.22}$$

The quasi-local nature also holds for the inverse transformation of Eq. (1.20), i.e., $\hat{\sigma}_i^\alpha$ is superposed only from $\hat{\tau}_j^\beta$ within an exponentially decaying envelope around site i.

The l-bit operators obey spin commutation relations and so can be thought of as effective spins. In particular, the eigenvalues of $\hat{\tau}_i^\alpha$ are ± 1. From Eq. (1.21), the eigenstates of the Hamiltonian are simply bitstrings in the $\hat{\tau}^z$ basis, e.g., $|+-+\cdots\rangle_\tau$ or $|-++\cdots\rangle_\tau$. These eigenstates clearly do not obey the ETH. For example, let $|n\rangle \equiv |+++\cdots\rangle_\tau$ be the eigenstate with all l-bits pointing up,

$|m\rangle \equiv |- + + \cdots\rangle_\tau$ have the first l-bit flipped, and $|m'\rangle \equiv |+ + \cdots -\rangle_\tau$ have the last l-bit flipped. The ETH would assert that $\langle m'|\hat{\sigma}_1^z|n\rangle$ and $\langle m|\hat{\sigma}_1^z|n\rangle$ should be of comparable magnitude. Yet one finds that $\langle m'|\hat{\sigma}_1^z|n\rangle$ is exponentially smaller than $\langle m|\hat{\sigma}_1^z|n\rangle$ by a factor $e^{-\frac{N}{\xi}}$, because the decomposition of $\hat{\sigma}_1^z$ into l-bit operators has exponentially small weight on those which flip spin N ($\hat{\tau}_N^x$ and $\hat{\tau}_N^y$). More physically, the excitation created by $\hat{\sigma}_1^z$ cannot spread through the system, since the probability of observing spins around site N to have flipped is only ever exponentially small. Lack of equilibration is a direct consequence of the l-bit phenomenology for MBL.

Numerical diagnostics for MBL are usually defined in constrast to the ETH. For example, in an ETH phase $\langle n|\hat{\sigma}_1^z|n\rangle = 0$ for every $|n\rangle$ in the middle of the spectrum[3] (because the equilibrium value is 0 at infinite temperature), whereas in an MBL phase $\langle n|\hat{\sigma}_1^z|n\rangle$ is close to either $+1$ or -1 depending on the specific state. The level spacing statistics in an ETH phase are GOE, whereas they are Poisson in an MBL phase. Local operators have matrix elements between exponentially many eigenstates in an ETH phase but only $O(1)$ in an MBL phase. All of the models studied numerically in the references above exhibit transitions between an ETH phase at weak disorder and an MBL phase at strong disorder, which makes these quantities useful order parameters for identifying the transitions and understanding the dynamical behavior on either side.

It is worth emphasizing that both the ETH and MBL are statements about the *eigenstates* of many-body Hamiltonians. They do not explicitly reference dynamical behavior. Nonetheless, highly non-trivial results on the dynamics follow directly once one has identified ETH or MBL phases. This is the underlying motivation for studying such eigenstate phases among the non-equilibrium quantum mechanics community.

1.3 Quantum dynamics as an algorithm for solving hard problems

1.3.1 Constraint satisfaction problems

Consider the following "constraint satisfaction" problem, seemingly unrelated to many-body physics or physics in general: is it possible for the logical statement

$$\big(x_1 \vee \neg x_2\big) \wedge \big(\neg x_1 \vee \neg x_3 \vee x_4\big) \wedge \big(\neg x_2 \vee x_3 \vee x_4\big) \wedge \big(x_2\big) \tag{1.23}$$

to be made True? For this specific example, the answer is yes: one possibility is $x_1 = $ True, $x_2 = $ True, $x_3 = $ False, $x_4 = $ True.

From the computer science perspective, such a question is not as artificial as it may seem: an enormous variety of computational tasks can be phrased as attempting to satisfy multiple constraints simultaneously, and any set of logical

[3] An important exception is systems with additional conserved quantities. For example, the Hamiltonian in Eq. (1.19) conserves the total z magnetization. In these cases, one formulates the ETH separately for each corresponding subspace.

constraints can be cast into the above "conjuctive normal form" (OR clauses joined together by ANDs).

From the physics perspective, such a question is not as irrelevant as it may seem: one can directly map the above problem onto an interacting Ising spin system. Replace the Boolean variables with spin variables according to True $\equiv$ $+$ and False $\equiv -$. Whether Eq. (1.23) can be made True is equivalent to whether the classical[4] Hamiltonian

$$H = \left(\frac{1-\sigma_1^z}{2}\right)\left(\frac{1+\sigma_2^z}{2}\right) + \left(\frac{1+\sigma_1^z}{2}\right)\left(\frac{1+\sigma_3^z}{2}\right)\left(\frac{1-\sigma_4^z}{2}\right) + \left(\frac{1+\sigma_2^z}{2}\right)\left(\frac{1-\sigma_3^z}{2}\right)\left(\frac{1-\sigma_4^z}{2}\right) + \left(\frac{1-\sigma_2^z}{2}\right) \tag{1.24}$$

has a ground state with energy zero (otherwise the ground state energy is positive). Furthermore, each assignment of truth values to the $\{x_i\}$ is in one-to-one correspondence with a configuration of the $\{\sigma_i\}$. The number of assignments yielding True equals the number of zero-energy states, and the number of OR clauses which an assignment fails to make True equals the energy of the corresponding configuration. It is clear that this mapping holds not just for the given example but for any problem of satisfying a logical statement in conjunctive normal form, referred to as a "satisfiability" problem.

Note three features of the Hamiltonian obtained from the satisfiability problem. First, many interaction terms are higher-body than two. A clause with K variables corresponds to a K-body interaction. Second, the allowed interaction terms are not limited by any spatial structure. One refers to the interactions as "infinite-range", since any spin can in principle interact with any other. This is quite natural from the computer science perspective: a satisfiability problem derived from, e.g., links between internet websites need not lie on a simple lattice with nearest-neighbor interactions. Third, the interactions are frustrated. Some terms bias a spin to point up, while others bias it to point down. These features make the physics of computationally-inspired spin systems different from that of traditional condensed matter systems, and the statistical physics community is actively researching the unique behavior that results [61–65].

The goal in such problems is to find the ground state. This is very hard to do for a generic spin glass, and in fact, satisfiability problems were the first to be proven NP-complete[5]. As of yet, there is no known algorithm that can solve arbitrary satisfiability problems in polynomial time.

Physics-inspired approaches [66–68] have the advantage of being general-purpose but, as with all other algorithms, come with their own set of weaknesses and limitations. Simulated annealing is the most prominent example. One starts in a random configuration, which will almost certainly be well above the ground state, and runs a Monte Carlo simulation at progressively lower temperatures.

[4] By "classical", we mean a spin Hamiltonian which is diagonal in the $\hat{\sigma}^z$ basis.

[5] An NP-complete problem is one onto which any NP problem can be mapped efficiently. Thus being able to solve an NP-complete problem efficiently would enable one to solve any NP problem efficiently.

Assuming the system remains in equilibrium at each stage in the process, it will be in the ground state once zero temperature is reached. Simulated annealing works spectacularly well when the Hamiltonian has a single global minimum without any local minima: in this case, one can set the temperature to zero at the start and simply "walk downhill". Real problems do have local minima, but annealing continues to succeed as long as the local minima are not too numerous and the energy barriers are not too large. Unfortunately, hard constraint satisfaction problems, including but not limited to the satisfiability problem, have famously "rugged" energy landscapes with many deep local minima [69–74]. Annealing generically requires exponentially long times to find the ground states of such systems. In this sense, constraint satisfaction problems are particularly dramatic examples of spin glasses which fail to equilibrate.

One can define ruggedness more carefully through the concept of "clustering". Two solutions to a constraint satisfaction problem are said to be in the same cluster if one can be transformed into the other, changing only a single bit at a time, without ever leaving the set of solutions. Said differently, solutions within the same cluster can be connected by a path in configuration space which lies entirely within the solution set. If no such path exists, the solutions belong to different clusters. One can identify clusters not just of solutions but of states at any energy density: simply replace the phrase "solution set" with "states at energy density ϵ" and use the same definition. As an example, suppose the solutions to a (classical) problem involving four bits are

$$|++++\rangle\,, \quad |+++-\rangle\,, \quad |-+++\rangle\,, \quad |+-++\rangle\,, \quad |+---\rangle\,. \tag{1.25}$$

These solutions separate into clusters as

$$\underbrace{|++++\rangle\,, \quad |-+++\rangle\,, \quad |+-++\rangle}_{\text{Cluster 1}}, \quad \underbrace{|+++-\rangle\,, \quad |+---\rangle}_{\text{Cluster 2}}. \tag{1.26}$$

$|-+++\rangle$ can be transformed into $|+-++\rangle$ by way of $|++++\rangle$, but there is no way to transform $|-+++\rangle$ into $|+++-\rangle$.

We say that an energy landscape is rugged if there is some threshold energy density ϵ_d below which the states are organized into exponentially many clusters. Many difficult problems have particularly rugged landscapes. Not only are there numerous clusters, but energy barriers of height $O(N)$ separate them and $O(N)$-many bits must be flipped to pass from one cluster to another.

Rugged energy landscapes are an obstacle not just to simulated annealing but to every known general-purpose algorithm. If an algorithm is designed to find ground states for arbitrary Hamiltonians, it is hard to imagine any approach other than simply proposing moves that lower the energy based on the current environment. Once the algorithm finds itself in a local minimum, the only way to progress further is to return to energies above ϵ_d and repeat the process, hoping to find a lower minimum on the next iteration. It should come as no surprise that this is often a very slow procedure.

1.3.2 The p-spin model and the random energy model

Given the ubiquity of rugged energy landscapes in constraint satisfaction problems, it pays to consider toy models that exhibit the salient physics. The p-spin model is the most well-studied. It consists of N spin-1/2s with random all-to-all p-body interactions. Although originally introduced as a mean-field model for physical spin glasses [75–77], it has since received attention for its connection to constraint satisfaction problems [63, 78] (and to structural glasses as well [79, 80]). The versatility of the p-spin model is due to the particularly simple Gaussian correlations between the energy levels. It serves as an analytically tractable model of rugged landscapes.

The p-spin Hamiltonian is

$$H_p = \sum_{(i_1 \cdots i_p)} J_{i_1 \cdots i_p} \sigma^z_{i_1} \cdots \sigma^z_{i_p}. \tag{1.27}$$

The sum is over all p-tuples of the N spins. Each coupling $J_{i_1 \cdots i_p}$ is an independent Gaussian random variable of mean 0 and variance $\frac{p!}{2N^{p-1}}$. Note that as an operator, H_p is trivially diagonal in the $\hat{\sigma}^z$ basis (i.e., is "classical"). Our discussion of energy landscapes focuses on H_p as a function of $\hat{\sigma}^z$ eigenstate. It is analogous to the landscape formed from a potential energy $U(x)$, which is trivially diagonal in the position basis. One studies dynamics within the landscape by adding non-commuting terms to the Hamiltonian (e.g., $\hat{p}^2/2m$).

Before discussing Eq. (1.27), let us establish notation which we shall use throughout the thesis. $\mathbb{E}[\,\cdot\,]$ will denote an average over the random couplings $J_{i_1 \cdots i_p}$. To denote bitstrings in the $\hat{\sigma}^z$ basis (e.g., $|+-+\cdots\rangle$ or $|-++\cdots\rangle$), we will often simply write σ, where the i^{th} spin has value $\sigma_i = \pm 1$. Finally, a useful measure of distance between two states σ and σ' is the Hamming distance $x(\sigma, \sigma')$, i.e., the fraction of spins which differ between the two states:

$$x(\sigma, \sigma') \equiv \frac{1}{2}\left(1 - \frac{1}{N}\sum_{i=1}^{N} \sigma_i \sigma'_i\right). \tag{1.28}$$

From Eq. (1.27), it is straightforward to evaluate the average energy of a configuration and the covariance matrix:

$$\mathbb{E}\big[H_p(\sigma)\big] = \sum_{(i_1 \cdots i_p)} \mathbb{E}\big[J_{i_1 \cdots i_p}\big] \sigma_{i_1} \cdots \sigma_{i_p} = 0, \tag{1.29}$$

$$\begin{aligned}
\mathbb{E}\big[H_p(\sigma) H_p(\sigma')\big] &= \sum_{(i_1 \cdots i_p)} \sum_{(i'_1 \cdots i'_p)} \mathbb{E}\big[J_{i_1 \cdots i_p} J_{i'_1 \cdots i'_p}\big] \sigma_{i_1} \cdots \sigma_{i_p} \sigma'_{i'_1} \cdots \sigma'_{i'_p} \\
&= \sum_{(i_1 \cdots i_p)} \frac{p!}{2N^{p-1}} \sigma_{i_1} \sigma'_{i_1} \cdots \sigma_{i_p} \sigma'_{i_p} \\
&\sim \frac{N}{2}\Big(1 - 2x(\sigma, \sigma')\Big)^p.
\end{aligned} \tag{1.30}$$

These expressions summarize why the p-spin model is a useful testbed for disordered systems: the energy landscape is Gaussian-correlated with correlations that depend only on the Hamming distance.

The parameter p sets the strength of the correlations and is a useful parameter to vary. In particular, as $p \to \infty$,

$$\mathbb{E}\left[H_p(\sigma)H_p(\sigma')\right] \to \frac{N}{2}\delta_{0,x(\sigma,\sigma')} = \frac{N}{2}\delta_{\sigma,\sigma'}. \tag{1.31}$$

The energies are independent and distributed as

$$P_1(E) = \sqrt{\frac{1}{\pi N}}e^{-E^2/N}. \tag{1.32}$$

In this limit, the p-spin model is referred to as the "random energy model" (REM) [75].

The REM is rightfully known as the simplest spin glass. Since the energy levels are independent, the average density of states is

$$\mathbb{E}\big[\mathcal{N}(\epsilon)\big] = 2^N\sqrt{\frac{1}{\pi N}}e^{-E^2/N} = \sqrt{\frac{1}{\pi N}}e^{N(\ln 2-\epsilon^2)}, \tag{1.33}$$

where $\epsilon \equiv E/N$. Since $\mathcal{N}(\epsilon) \equiv e^{Ns(\epsilon)}$, we can read off the entropy density:

$$s(\epsilon) = \ln 2 - \epsilon^2. \tag{1.34}$$

The ground state energy density is $\epsilon_{\mathrm{GS}} \equiv -\sqrt{\ln 2}$: the number of states at $\epsilon > \epsilon_{\mathrm{GS}}$ is exponentially large, whereas the number at $\epsilon < \epsilon_{\mathrm{GS}}$ is exponentially small. One has that

$$\frac{1}{T} = \frac{\partial s}{\partial \epsilon} = -2\epsilon, \tag{1.35}$$

and thus ϵ_{GS} occurs at a finite temperature $T_c \equiv 1/2\sqrt{\ln 2}$. As trivial as it may seem, we have identified a phase transition in the REM. At temperatures above T_c, the system is in a paramagnetic phase in which the Gibbs distribution is spread over exponentially many states. At temperatures below T_c, however, the system is in a glass phase. The Gibbs distribution is frozen onto $O(1)$-many states, all of which are at energy density ϵ_{GS}. Sec. 3 of the thesis discusses the interpretation of this low-temperature phase further.

The above analysis, although simple, is sloppy in that it neglects possible fluctuations in $\mathcal{N}(\epsilon)$. Said differently, $\mathbb{E}[\mathcal{N}(\epsilon)]$ may not represent the typical value of $\mathcal{N}(\epsilon)$ seen in most instances, especially since it is a sum of exponentially many rare events. This happens often in spin glass models. However, the fluctuations are known to be small in the REM. See Ref. [63] or Sec. 3 of this thesis for details.

There is one important aspect of the REM which is hidden in the thermodynamic analysis: the ruggedness of the energy landscape. Suppose that state σ has energy density $\epsilon < 0$, and consider the states obtained by flipping one spin. There are N such states, but since the probability of a state having $\epsilon \neq 0$

is exponentially small (independently of all others), those N states will have energy density $\epsilon' = 0$ with high probability. The cost of flipping a single spin is $O(N)$, namely $N(0-\epsilon) = N|\epsilon|$, starting from any state at $\epsilon < 0$ (i.e., at finite temperature, see Eq. (1.35)). In other words, every finite-temperature state lies in an energy well which is $O(N)$ deep. Such an energy landscape is extremely rugged. Imagine running a Monte Carlo simulation with single-spin-flip update rules, e.g., Metropolis. The rate at which the system is kicked out of state σ is $e^{-\Delta E/T} = e^{-N|\epsilon|/T}$, and thus the timescale on which the system equilibrates is exponentially long *at any finite temperature*. Even though the equilibrium properties of the REM are paramagnetic above T_c, it would be more accurate to say that the system is dynamically frozen (a "dynamical glass") at all finite temperatures. It is important to keep this fact in mind, that equilibration may be exponentially slow even in a putatively "high-temperature" phase.

1.3.3 Quantum algorithms

So far, everything discussed in this subsection has been classical: we have examined classical spin Hamiltonians, described the hardness of finding low-energy states through the classical energy landscape, and considered algorithms implemented on classical computers. Quantum computing approaches have the potential to circumvent some of the difficulties inherent in classical algorithms.

Consider quantum annealing, intended to be analogous to simulated annealing [78, 81–83]. Given a classical spin Hamiltonian H_p for which one desires the ground state, one applies a time-dependent transverse field $\Gamma(t)$, so that the full Hamiltonian is

$$H(t) = H_p - \Gamma(t) \sum_i \hat{\sigma}_i^x. \tag{1.36}$$

Initially, $\Gamma(0) \gg 1$ and the system is prepared in the corresponding ground state, i.e., with all spins aligned along the field. The field is decreased to 0 over a time τ, so that $H(\tau) = H_p$, and during this period the system evolves via its quantum dynamics. The adiabatic theorem states that the system will remain in the instantaneous ground state, which at time τ is the desired ground state, if $\tau \gg \max_\Gamma V/\Delta(\Gamma)^2$, where $\Delta(\Gamma)$ is the energy gap between the lowest and first excited states at field Γ and V is a constant with units of energy [84]. As with simulated annealing, quantum annealing succeeds if one ramps sufficiently slowly but fails if one ramps too quickly. The required runtime is of order $\max_\Gamma V/\Delta(\Gamma)^2$.

Unfortunately, there is no known example in which quantum annealing unambiguously solves a hard constraint satisfaction or optimization problem in polynomial time [85–88]. Furthermore, the picture of quantum annealing developed over the past two decades is purely in terms of the spectrum as a function of Γ. We have a much more limited understanding of the explicit dynamical processes that cause quantum annealing to succeed or fail.

A somewhat simpler context in which to study the potential of quantum dynamics is "matching" problems. For example, suppose that a traveling salesperson wants not just one efficient sales route but many, each distinct from the

others so that she may pick the one which suits her best. The salesperson has no choice but to labor for days to find even one satisfactory route. However, once she has found that first route, perhaps she can use it to generate others faster than from scratch. This is the matching problem: given an optimization problem *and one solution*, find others that are sufficiently distinct.

There are multiple reasons why one would want a representative collection of solutions to a problem, and thus be interested in efficient matching: one may desire solutions with additional properties, a larger set of solutions is more robust to parameter perturbations, and a representative set gives insight into underlying structure in the problem. However, it is intuitively clear that ruggedness in the energy landscape makes a matching problem difficult for the same reason as the original optimization problem. Furthermore, certain matching problems are themselves NP-complete [89].

Quantum dynamics provides an "algorithm" for matching problems that is even more straightforward than annealing: apply a *static* transverse field, i.e.,

$$H = H_p - \Gamma \sum_i \hat{\sigma}_i^x, \tag{1.37}$$

initialize the system in the given solution $|\sigma\rangle$, and wait. The matching problem is solved if the system is later found in a different state $|\sigma'\rangle$ which is also a solution, an event occuring with probability $|\langle\sigma'|e^{-iHt}|\sigma\rangle|^2$. Hamiltonian dynamics conserves energy, and so starting in the state $|\sigma\rangle$ biases the system to explore configurations with the same energy as $|\sigma\rangle$ (although keep in mind that the total energy $\langle H\rangle$ rather than $\langle H_p\rangle$ is conserved). Furthermore, being quantum mechanical, hopefully the system will tunnel between the energy barriers that separate states in a reasonable amount of time. One can thus understand the performance of this algorithm by understanding the tunneling amplitudes between low-energy states.

We can now establish the connection to Secs. 1.1 and 1.2 of the thesis: the ability of quantum dynamics to solve matching problems is closely related to its ability to thermalize the system. If the system cannot tunnel between low-energy states, then it cannot come to equilibrium. Conversely, if the system does tunnel efficiently, then one has a strong indication that the system does thermalize. However, this thesis shall make clear that the relationship between ETH, MBL, and matching problems is nonetheless subtle.

1.4 Motivation and summary of results

Part 1 of the thesis is based on the work in Refs. [89–91], motivated by previous results in Ref. [92]. The goal is to identify the dynamical phases of the quantum p-spin and random energy models, and use the results to draw conclusions about the potential of quantum dynamics for solving computational tasks such as matching problems. The quantum models are of the form in Eq. (1.37). The

quantum p-spin model is

$$H = H_p - \Gamma \sum_i \hat{\sigma}_i^x, \tag{1.38}$$

with H_p given by Eq. (1.27), and the quantum random energy model is

$$H = H_{\text{REM}} - \Gamma \sum_i \hat{\sigma}_i^x, \tag{1.39}$$

where H_{REM} has independent energy levels in the $\hat{\sigma}^z$ basis distributed from Eq. (1.32).

We ask three broad questions:

1. **Do the quantum p-spin and random energy models obey the ETH? Do they exhibit MBL?** We find that these models only obey the ETH in a high-energy portion of the spectrum. However, the remaining portion is not many-body localized either. This new non-ergodic or "trapped" phase is intermediate between ETH and MBL, in a sense which we make precise in Chap. 4. We understand the new phase in terms of the clustering defined above. States below a certain ϵ_d are divided into distant clusters, in which a non-zero fractional Hamming distance separates clusters (i.e., a non-zero *fraction* of the spins must be flipped) and the energy barriers throughout the distance have $O(N)$ height. We find that the effective tunneling amplitudes between clusters can be sufficiently small for the eigenstates of the quantum Hamiltonian to remain bound to single clusters, violating the ETH. At the same time, the eigenstates do hybridize within their individual clusters, which has no analogue in an MBL phase.

2. **What is the timescale for thermalization when it does occur?** In the trapped phase, thermalization does not occur, even for a finite-size system and for arbitrarily late times. Furthermore, we show that it proceeds exponentially slowly in a portion of the ETH phase. In the $N \to \infty$ limit, the system remains dynamically frozen and qualitatively indistinguishable from the non-ergodic phase over any finite timescale. This highlights a major limitation of the ETH: it makes no guarantees as to the timescale on which equilibration occurs.

3. **Can quantum tunneling be viable/efficient for solving matching problems?** Tunneling is severely constrained in the p-spin and random energy models. If the transverse field is too weak, the system is in the trapped phase and does not tunnel out of the cluster in which it was initialized. Matching fails because the system does not explore the full range of low-energy states (namely those in other clusters). However, if the transverse field is too strong, the spins are forced parallel to it. The reduction in the transverse energy $-\Gamma \langle \hat{\sigma}^x \rangle$ must be accompanied by an increase in the classical energy $\langle H_p \rangle$, i.e., the system is no longer exploring

configurations which sufficiently optimize the original constraint satisfaction problem. Matching fails here as well. We show that an intermediate-field "sweet spot" can exist, but that the timescale for tunneling between clusters and thus for solving the matching problem is necessarily exponential in system size. In this sense, quantum dynamics is never efficient. Yet all known classical algorithms also require exponential runtime, and we do show that quantum dynamics can outperform standard (and in some cases near-optimal) classical approaches.

The most important conclusion is that none of the results listed above are specific to the toy models under study. They rely only on ruggedness in the energy landscape as characterized by three features: the low-energy states are organized into exponentially many disconnected clusters, the fractional Hamming distance between any two clusters is non-zero, and the energy barriers that separate clusters are $O(N)$. Such features are present in the vast majority of hard constraint satisfaction and optimization problems (see Ref. [63] and references therein). Thus the results demonstrated here are of direct relevance to the quantum computing field.

Chapter 2

Quantum dynamics in the random energy model

We begin our study with the simple quantum random energy model (QREM), given by Eq. (1.39):

$$H = H_{\text{REM}} - \Gamma \sum_i \hat{\sigma}_i^x. \tag{1.39}$$

The Hilbert space is that of N spin-1/2s. H_{REM} is diagonal in the $\hat{\sigma}^z$ basis, with each diagonal element drawn from a Gaussian of variance $N/2$:

$$H_{\text{REM}} |\sigma\rangle = E |\sigma\rangle, \quad P(E) = \sqrt{\frac{1}{\pi N}} e^{-E^2/N}. \tag{2.1}$$

Sec. 2.1 provides the thermodynamic behavior of the QREM as a reference point. Sec. 2.2 gives a description of the eigenstate phases, and Sec. 2.3 the tunneling dynamics, both using perturbation theory in Γ. Sec. 2.4 then presents numerical evidence validating the analytic results.

2.1 Thermodynamics

The thermodynamic phase diagram of the QREM is shown in Fig. 2.1, both in the canonical and microcanonical ensembles. It was calculated in Ref. [93] using the replica trick on an imaginary-time representation of the partition function (which we will not elaborate on further). See also Ref. [85] for a simple derivation of parts of the diagram.

The QREM has three equilibrium phases:

- The classical paramagnet. The free energy density is

$$f_{\text{CPM}} = -T \ln 2 - \frac{1}{4T}. \tag{2.2}$$

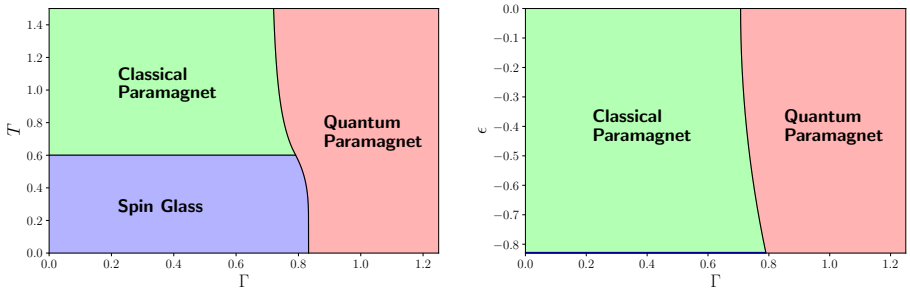

Figure 2.1: The thermodynamic phase diagram of the QREM, in the canonical Γ-T plane (left) and the microcanonical Γ-ϵ plane (right). The spin glass phase in the microcanonical diagram lies solely on the horizontal line $\epsilon = -\sqrt{\ln 2}$, at the bottom of the figure.

Note that f_{CPM} is identical to the Legendre transform of Eq. (1.34), the entropy of the *classical* REM. Thus all thermodynamic quantities are equal to those of the classical model and unaffected by the transverse field.

- The spin glass. The free energy density is simply

$$f_{\mathrm{SG}} = -\sqrt{\ln 2}, \tag{2.3}$$

identical to the classical REM [75]. As discussed in Sec. 1.3.2, the system is frozen onto $O(1)$-many states, all at energy density $\epsilon_{\mathrm{GS}} = -\sqrt{\ln 2}$ (hence the spin glass phase is not visible in the microcanonical diagram). Again, the transverse field has no effect on this picture.

- The quantum paramagnet. The free energy density is

$$f_{\mathrm{QPM}} = -T \ln 2 - T \ln \left(\cosh \frac{\Gamma}{T} \right). \tag{2.4}$$

Note that f_{QPM} is the free energy density for non-interacting spins in a field Γ. It is now the random energy term in the Hamiltonian which does not affect the thermodynamics. The transition between the classical phases (paramagnetic or spin glass) and the quantum paramagnetic phase is first-order: the transverse magnetization jumps discontinuously as Γ increases.

The essence of the phase diagram is that the system exhibits either "REM physics" or "non-interacting physics", without anything in between. REM physics results from an otherwise structureless system freezing into an $O(1)$ number of configurations, whereas non-interacting physics is that of uncoupled spins in a magnetic field. The QREM does not compromise between these two behaviors. At least thermodynamically, there is no hint of an external field in

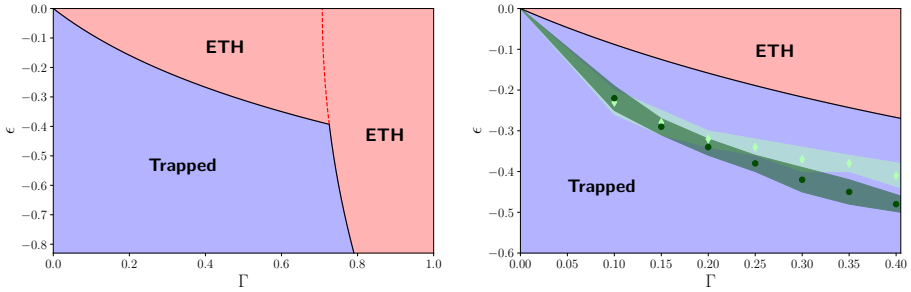

Figure 2.2: The eigenstate phase diagram of the QREM. The left panel shows the analytic estimate for the phase boundary (black line), as discussed in Sec. 2.2, alongside the thermodynamic boundary for reference (dashed red line). The right panel includes finite-size numerical estimates for a zoomed-in portion of the diagram, as discussed in Sec. 2.4. The light green markers are results from numerical forward-scattering calculations, and the dark green markers are from exact diagonalization (shading indicates the uncertainties).

the classical phases and no hint of interactions in the quantum paramagnetic phase.

Below, we shall focus on values of Γ and ϵ lying within the classical paramagnetic phase. As we discuss, the trivial thermodynamics of this phase belies highly non-trivial *dynamical* behavior which is particularly relevant for quantum computing algorithms.

2.2 Eigenstate phases

Fig. 2.2 shows the eigenstate phase diagram of the QREM, to be compared with the thermodynamic diagram. To understand the distinction between the "trapped" and "ETH" phases, keep in mind that at $\Gamma = 0$, the eigenstates are trivially $\hat{\sigma}^z$ eigenstates. In the trapped phase, the eigenstates remain $\hat{\sigma}^z$ eigenstates up to $O(1/N)$ corrections. Since there are exponentially many states at energies in the paramagnetic phase, such eigenstates clearly do not obey the ETH. As one increases Γ, the eigenstates undergo a transition in which they hybridize among the $\hat{\sigma}^z$ states at the given energy. Although we have not checked whether these eigenstates obey the ETH in the strict sense of Eq. (1.3), they do pass many of the standard tests for thermal eigenstates, and thus we identify this as the ETH phase. It is remarkable that the eigenstate phase transition occurs entirely within the classical paramagnetic phase, with non-trivial functional dependence $\Gamma_{\text{tun}}(\epsilon)$, despite the transverse field having no impact on thermodynamics. Below, we develop an understanding of the transition.

Before presenting the details, let us describe the underlying intuition. Our main analytical tool is perturbation theory in Γ. We consider a $\hat{\sigma}^z$ state $|\sigma\rangle$

having energy density ϵ, and think of it as being transformed into an eigenstate $|\Psi_\sigma\rangle$ which has amplitude on other states $|\sigma'\rangle$. The weight on $|\sigma'\rangle$ depends on the energy density and distance from $|\sigma\rangle$. Recall that we define distance to be the fraction of spins which differ between the two configurations:

$$x(\sigma,\sigma') \equiv \frac{1}{2}\left(1 - \frac{1}{N}\sum_{i=1}^{N}\sigma_i\sigma_i'\right). \tag{1.28}$$

We argue that the effective coupling between $|\sigma\rangle$ and $|\sigma'\rangle$ is exponentially small, which we write as $e^{-N\gamma(x,\epsilon)}$. Another important quantity is the *distance-resolved* density of states, i.e., the number of configurations at distance x with energy density ϵ. It is also exponential, written as $e^{Ng(x,\epsilon)}$.

$|\Psi_\sigma\rangle$ has large weight on a given state $|\sigma'\rangle$ only if the effective coupling to that state is larger than the unperturbed difference in energies between $|\sigma\rangle$ and $|\sigma'\rangle$. The smallest energy difference will be on the order of the level spacing around ϵ, which at distance x is $e^{-Ng(x,\epsilon)}$. Thus there exist configurations on which the eigenstate has large weight only if $g(x,\epsilon) > \gamma(x,\epsilon)$ for some $x \in (0,1]$. This condition defines the phase boundary $\Gamma_{\text{tun}}(\epsilon)$. At smaller fields, the weight on *every* $|\sigma'\rangle$ is small and $|\Psi_\sigma\rangle \sim |\sigma\rangle$ (the trapped phase). At larger fields, the eigenstate is hybridized among configurations throughout the configuration space and can no longer be identified with an individual $|\sigma\rangle$ (the ETH phase).

2.2.1 The forward-scattering approximation

Using perturbation theory in Γ has precedent in studies of single-particle localization [38,45,94]. To see why it applies here, compare the QREM Hamiltonian,

$$H = H_{\text{REM}} - \Gamma\sum_i \hat{\sigma}_i^x, \tag{1.39}$$

to the toy model for localization from Sec. 1.2.1,

$$H = \sum_i \epsilon_i |i\rangle\langle i| - \gamma\sum_{\langle ij\rangle}\left(|i\rangle\langle j| + |j\rangle\langle i|\right). \tag{1.9}$$

H_{REM} acts as an "on-site" potential in the $\hat{\sigma}^z$ configuration space, analogous to ϵ_i. Recall that the configuration space for N spin-1/2s can be visualized as the corners of an N-dimensional hypercube (see Fig. 2.3 for the $N = 2$ case as an example). Since the action of $\hat{\sigma}_i^x$ in the $\hat{\sigma}^z$ basis is to flip spin i, $-\Gamma\sum_i \hat{\sigma}_i^x$ acts as a hopping term between neighboring sites of the configuration space, analogous to $-\gamma\sum_{\langle ij\rangle}|i\rangle\langle j|$. Thus the QREM can be thought of as a single-particle localization problem on the N-dimensional hypercube. In particular, the "potential" is uncorrelated, just as in the standard version of the single-particle model.

The $\hat{\sigma}^z$ eigenstate $|\sigma\rangle$ is perturbed by the transverse field into an eigenstate $|\Psi_\sigma\rangle$. Denote the unperturbed energy of $|\sigma\rangle$ by E, i.e., $H_{\text{REM}}|\sigma\rangle = E|\sigma\rangle$, and similarly denote the unperturbed energy of any state $|\sigma''\rangle$ by $E(\sigma'')$. Finally,

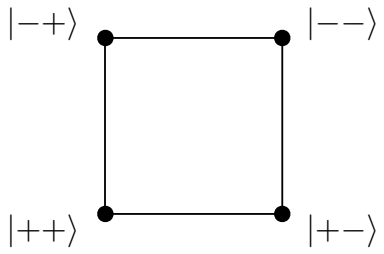

Figure 2.3: The configuration space for two spin-1/2s (black vertices). The label of each vertex is the corresponding $\hat{\sigma}^z$ configuration. One generalizes to more spins by including more dimensions.

write the perturbed energy of $|\Psi_\sigma\rangle$ as $E + \Delta$. Time-independent perturbation theory [95] gives that

$$|\Psi_\sigma\rangle = |\sigma\rangle + \frac{\pi_\sigma}{E - H_{\text{REM}}} \left(-\Gamma \sum_i \hat{\sigma}_i^x - \Delta \right) |\Psi_\sigma\rangle \,, \tag{2.5}$$

where $\pi_\sigma \equiv I - |\sigma\rangle\langle\sigma|$ and Δ is determined self-consistently order by order. Eq. (2.5) can be iterated to obtain a perturbative expansion of $|\Psi_\sigma\rangle$. Writing up to second order explicitly,

$$\begin{aligned} |\Psi_\sigma\rangle = |\sigma\rangle &- \sum_i \frac{\Gamma}{E - E\big(\hat{\sigma}_i^x |\sigma\rangle\big)} \hat{\sigma}_i^x |\sigma\rangle \\ &+ \sum_{i \neq j} \frac{\Gamma^2}{\big(E - E\big(\hat{\sigma}_j^x \hat{\sigma}_i^x |\sigma\rangle\big)\big)\big(E - E\big(\hat{\sigma}_i^x |\sigma\rangle\big)\big)} \hat{\sigma}_j^x \hat{\sigma}_i^x |\sigma\rangle \\ &+ \sum_i \frac{\Gamma\Delta}{\big(E - E\big(\hat{\sigma}_i^x |\sigma\rangle\big)\big)^2} \hat{\sigma}_i^x |\sigma\rangle + \ldots . \end{aligned} \tag{2.6}$$

In particular, consider the amplitude on a different $\hat{\sigma}^z$ state $|\sigma'\rangle$, i.e., $\langle\sigma'|\Psi_\sigma\rangle$. Let the distance between $|\sigma\rangle$ and $|\sigma'\rangle$ be x. Thus the two configurations differ in the values of Nx spins. Note that each application of $\Gamma\hat{\sigma}_i^x$ to $|\Psi_\sigma\rangle$ flips a single spin and comes with a factor of Γ, and each application of Δ leaves $|\Psi_\sigma\rangle$ unaffected and comes with a factor of Γ (since $\Delta \sim O(\Gamma)$). Thus $\langle\sigma'|\Psi_\sigma\rangle$ is zero until the Nx^{th} order of the perturbation series.

At this point, we make the forward-scattering approximation (FSA) [45,92], in which $\langle\sigma'|\Psi_\sigma\rangle$ is approximated by solely the leading Nx^{th}-order terms. The FSA is different from a simple truncation of the perturbation series, since different $|\sigma'\rangle$ require going to different orders (and indeed, we must go to arbitrarily high orders as $N \to \infty$). The energy shift Δ doesn't enter into $\langle\sigma'|\Psi_\sigma\rangle$ at leading order. After some thought, one sees that the only terms which do survive correspond to the *directed* sequences of spin flips transforming $|\sigma\rangle$ into $|\sigma'\rangle$. For

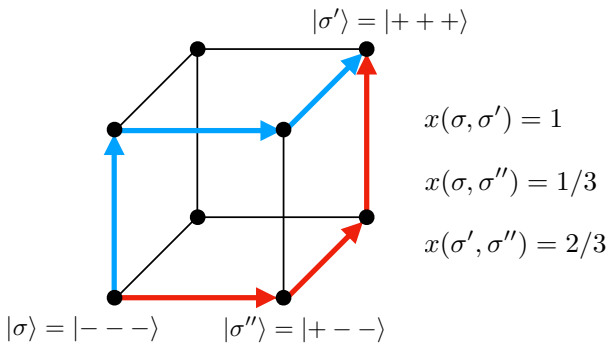

Figure 2.4: The configuration space for $N = 3$, with two directed paths from $|\sigma\rangle$ to $|\sigma'\rangle$ shown in red and blue. $|\sigma''\rangle$ is an intermediate configuration along the red path. Also shown for reference are the Hamming distances between the three indicated states.

example, if $|\sigma\rangle = |+++\rangle$ and $|\sigma'\rangle = |--+\rangle$, the two terms kept by the FSA correspond to flipping spin 1 followed by 2 and flipping 2 followed by 1:

$$\begin{aligned}\langle\sigma'|\Psi_\sigma\rangle \approx &\frac{\Gamma}{\big(E - E\big(|--+\rangle\big)\big)}\frac{\Gamma}{\big(E - E\big(|-++\rangle\big)\big)} \\ &+ \frac{\Gamma}{\big(E - E\big(|--+\rangle\big)\big)}\frac{\Gamma}{\big(E - E\big(|+-+\rangle\big)\big)}.\end{aligned} \tag{2.7}$$

The generalization to higher orders is

$$\langle\sigma'|\Psi_\sigma\rangle \approx \sum_P \prod_{\sigma''\in P} \frac{\Gamma}{E - E(\sigma'')}, \tag{2.8}$$

where the sum is over all $(Nx)!$ directed sequences and the product is over the Nx intermediate configurations along a sequence. The allowed terms can be visualized in configuration space as the directed paths from $|\sigma\rangle$ to $|\sigma'\rangle$. Fig. 2.4 gives an example.

Eq. (2.8) is the forward-scattering approximation to the eigenstates of the QREM. We use it to investigate eigenstate thermalization or the lack thereof. If $\big|\langle\sigma'|\Psi_\sigma\rangle\big| \ll 1$ for all $\sigma' \neq \sigma$, then certainly the eigenstates do not obey the ETH. Furthermore, our use of perturbation theory is consistent in this regime, and we expect it to give an accurate description of the eigenstates. Those $|\sigma'\rangle$ on which $\big|\langle\sigma'|\Psi_\sigma\rangle\big| \geq 1$ are referred to as "resonant" configurations. Strictly speaking, the appearance of resonant configurations does not mean that the eigenstates obey the ETH or are even delocalized. It only shows that perturbation theory cannot describe them. Regardless, we shall use the proliferation of resonances as a reasonable indicator for an eigenstate phase transition, and later support this prediction with exact diagonalization numerics (Sec. 2.4.1).

One can always evaluate Eq. (2.8) numerically for a given realization of H_{REM}, and build statistics over many different realizations. We do this in Sec. 2.4.2, but the QREM is sufficiently simple to allow one to study the problem analytically. We do so first, and use the numerical results as an important validation.

2.2.2 Path statistics

Each $E(\sigma'')$ in Eq. (2.8), which we now write as $N\epsilon(\sigma'')$, is an independent random variable of mean 0. If we replace every $\epsilon(\sigma'')$ by $\mathbb{E}\big[\epsilon(\sigma'')\big]$, we have a particularly simple expression:

$$\big|\,\langle\sigma'|\Psi_\sigma\rangle\,\big| \sim (Nx)!\left(\frac{\Gamma}{N|\epsilon|}\right)^{Nx} \sim e^{-N\gamma(x,\epsilon)}, \tag{2.9}$$

where

$$\gamma(x,\epsilon) \equiv -x\ln\frac{x\Gamma}{e|\epsilon|}. \tag{2.10}$$

Note that $\gamma(x,\epsilon) > 0$ for all $x \in (0,1]$, and thus Eq. (2.9) is exponentially small for all $|\sigma'\rangle$, if $\Gamma < e|\epsilon|$. This would seem to suggest that the eigenstates delocalize at $\Gamma = e|\epsilon|$, but such an estimate turns out to be too crude. Even though $\epsilon(\sigma'')$ is *typically* 0, there are nevertheless exponentially many configurations with $\epsilon(\sigma'') \approx \epsilon$, namely $2^N e^{-N\epsilon^2}$ of them. These configurations contribute small energy denominators which enhance $\langle\sigma'|\Psi_\sigma\rangle$, as we now show.

Every term in Eq. (2.8) ends with a factor $\Gamma/N(\epsilon-\epsilon')$ (where we've defined $\epsilon(\sigma') \equiv \epsilon'$), so factor it out:

$$\langle\sigma'|\Psi_\sigma\rangle = \frac{\Gamma}{N\big(\epsilon-\epsilon'\big)}\sum_P\prod_{\sigma''\in P}\frac{\Gamma}{N\big(\epsilon-\epsilon(\sigma'')\big)} \equiv \frac{V_{\text{eff}}(x,\epsilon)}{N\big(\epsilon-\epsilon'\big)}, \tag{2.11}$$

where the product now omits σ'. $V_{\text{eff}}(x,\epsilon)$ has the interpretation of an effective coupling between configurations separated by distance x at energy density ϵ. If we set every $\epsilon(\sigma'')$ in $V_{\text{eff}}(x,\epsilon)$ to 0, but do not set ϵ' to 0, we have

$$\big|\,\langle\sigma'|\Psi_\sigma\rangle\,\big| \sim \frac{e^{-N\gamma(x,\epsilon)}}{N|\epsilon-\epsilon'|}, \tag{2.12}$$

with $\gamma(x,\epsilon)$ again given by Eq. (2.10). The eigenstate amplitude will be large if

$$|\epsilon-\epsilon'| \lesssim e^{-N\gamma(x,\epsilon)}. \tag{2.13}$$

This applies to a single state $|\sigma'\rangle$ at distance x. Since the unperturbed energy levels in the REM are independent, the average density of states at distance x, denoted $\mathcal{N}(x,\epsilon)$, is straightforward to compute:

$$\mathbb{E}\big[\mathcal{N}(x)\big] = \binom{N}{Nx}e^{-N\epsilon^2} \sim e^{Ng(x,\epsilon)}, \tag{2.14}$$

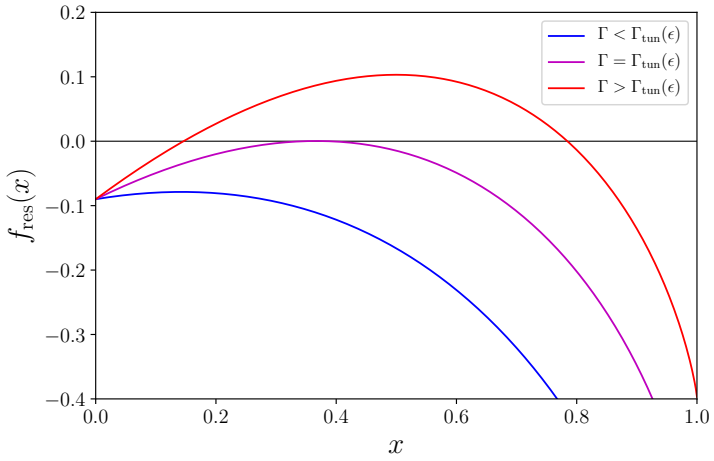

Figure 2.5: The entropy of resonances, $f_{\text{res}}(x, \epsilon)$, as a function of x at $\epsilon = -0.3$. Three different values of Γ are used: $\Gamma = 0.35$ (blue), 0.474 (magenta), 0.60 (red).

where

$$g(x, \epsilon) = -x \ln x - (1 - x) \ln (1 - x) - \epsilon^2. \tag{2.15}$$

Thus the expected number of configurations within energy $e^{-N\gamma(x,\epsilon)}$ of ϵ, i.e., the number of resonant configurations, denoted $\mathcal{N}_{\text{res}}(x, \epsilon)$, is

$$\mathbb{E}\big[\mathcal{N}_{\text{res}}(x, \epsilon)\big] = e^{N\left(g(x,\epsilon)-\gamma(x,\epsilon)\right)} \equiv e^{N f_{\text{res}}(x,\epsilon)}, \tag{2.16}$$

where

$$f_{\text{res}}(x, \epsilon) = x \ln \frac{\Gamma}{e|\epsilon|} - (1 - x) \ln (1 - x) - \epsilon^2. \tag{2.17}$$

If $f_{\text{res}}(x, \epsilon) < 0$ for all $x \in (0, 1]$, then the expected number of resonant configurations is exponentially small throughout the configuration space. In other words, there are *no* resonances except for in a vanishing fraction of realizations[1]. Perturbation theory holds, and the eigenstate $|\Psi_\sigma\rangle$ is simply $|\sigma\rangle$ up to small corrections (a "trapped" eigenstate). If $f_{\text{res}}(x, \epsilon) > 0$ for some $x \in (0, 1]$, then the perturbation theory breaks down. Given the caveat mentioned above and the numerical results in Sec. 2.4.1, we identify this as the ETH phase. Thus the boundary $\Gamma_{\text{tun}}(\epsilon)$ between the trapped and ETH phases is where $\max_x f_{\text{res}}(x, \epsilon) = 0$. The situation is illustrated in Fig. 2.5. We have that

$$\ln \frac{\Gamma_{\text{tun}}}{e|\epsilon|} + \frac{|\epsilon|}{\Gamma_{\text{tun}}} - \epsilon^2 = 0. \tag{2.18}$$

[1] This follows rigorously from Markov's inequality as described in Chap. 3

The resulting $\Gamma_{\text{tun}}(\epsilon)$ constitutes the upper portion of the curve in Fig. 2.2 (the lower portion is discussed momentarily). At small ϵ, the phase boundary goes as

$$\Gamma_{\text{tun}}(\epsilon) \sim -\epsilon + \sqrt{2}\epsilon^2 + O\big(\epsilon^3\big). \tag{2.19}$$

$\Gamma_{\text{tun}}(\epsilon)$ is significantly less than the naive estimate $e|\epsilon|$. Even though the typical eigenstate amplitudes remain small, a subset of configurations become resonant as Γ increases beyond $\Gamma_{\text{tun}}(\epsilon)$. They are precisely those with energy densities particularly close to ϵ.

This derivation also explains the use of the term "trapped" to describe the low-energy eigenstates. As is clear from Eq. (2.17) and Fig. 2.5, $f_{\text{res}}(x,\epsilon)$ is always negative for x close to 0. Even when resonant configurations exist, they lie beyond a minimum distance, and the effective coupling $V_{\text{eff}}(x,\epsilon)$ is exponentially supressed from tunneling through non-resonant intermediate configurations. The trapped phase occurs when the suppression is sufficiently strong for $V_{\text{eff}}(x,\epsilon)$ to be smaller than level spacing at all distances. The system cannot tunnel through the energy barriers and thus remains trapped in state $|\sigma\rangle$.

Notice that in Fig. 2.2, we have cut off the trapped phase by the thermodynamic boundary between the classical and quantum paramagnets. Since the thermodynamic transition is first-order, we cannot detect it using perturbation theory at small Γ. However, it is clear from the numerical results below that the eigenstates are no longer trapped beyond the first-order line, and so we include it in the phase diagram.

Finally, one may rightfully wonder about the validity of replacing $\epsilon(\sigma'')$ by 0 in $V_{\text{eff}}(x,\epsilon)$, given the importance of not setting $\epsilon(\sigma')$ to 0. Fortunately, this replacement is valid. Write Eq. (2.8) as[2]

$$\big|\,\langle\sigma'|\Psi_\sigma\rangle\,\big| = \left(\frac{\Gamma}{N}\right)^{Nx} \sum_P \prod_{\sigma''\in P} \frac{1}{\big|\epsilon - \epsilon(\sigma'')\big|}. \tag{2.20}$$

The remaining product is the only factor which fluctuates between realizations. First consider the possibility of fluctuations which change the factors $|\epsilon-\epsilon(\sigma'')|$ by $O(1)$ amounts (e.g., $\epsilon(\sigma'') = \epsilon/2$). Writing

$$\prod_{\sigma''\in P} \frac{1}{\big|\epsilon - \epsilon(\sigma'')\big|} = e^{-\sum_{\sigma''\in P}\ln\left|\epsilon-\epsilon(\sigma'')\right|}, \tag{2.21}$$

we see that in order for such a fluctuation to scale as anything other than $\exp\big(-Nx\ln|\epsilon|\big)$, it must be that $O(N)$ of the σ'' along a single path P have $\epsilon(\sigma'') \neq 0$. The probability of such an event scales as e^{-cN^2}, with $c \sim O(1)$. Therefore the expected number of paths which contribute anything other than $\exp\big(-Nx\ln|\epsilon|\big)$, denoted $\mathcal{N}_{\text{fluc}}$, is

$$\mathbb{E}[\mathcal{N}_{\text{fluc}}] = (Nx)!\, e^{-cN^2} \to 0, \tag{2.22}$$

[2]Strictly speaking, Eq. (2.20) is an inequality, since $|\sum_P \cdot| \leq \sum_P |\cdot|$. However, we have found from the numerical studies in Sec. 2.4.2 that using $\sum_P |\cdot|$ does not noticeably modify any results. Conceptually, it takes a rare event to change the sign of a path amplitude (one needs $\epsilon(\sigma'') < \epsilon$), and the considerations here show that such events are negligible.

i.e., the expected number of atypical paths vanishes as $N \to \infty$.

There remains the possibility of individual configurations σ'' with energy densities exponentially close to ϵ. They can change the exponent in $V_{\text{eff}}(x, \epsilon)$ by themselves. Suppose that for some σ'' at distance y,

$$\left|\epsilon - \epsilon(\sigma'')\right| \sim e^{-Nd}, \tag{2.23}$$

with $d \sim O(1)$. The expected number of such configurations which lie along the directed paths to σ' is

$$\binom{Nx}{Ny} e^{-N\epsilon^2 - Nd}. \tag{2.24}$$

When one accounts for every path which passes through a single such σ'', the contribution of that σ'' to $V_{\text{eff}}(x, \epsilon)$ is

$$\begin{aligned}(Ny)! \left(\frac{\Gamma}{N|\epsilon|}\right)^{Ny} e^{Nd} \left(N(x-y)\right)! \left(\frac{\Gamma}{N|\epsilon|}\right)^{N(x-y)} \\ = \left(\frac{\Gamma}{N|\epsilon|}\right)^{Nx} (Ny)!(N(x-y))! e^{Nd}.\end{aligned} \tag{2.25}$$

In the top line, the first two factors constitute the sum over paths leading to σ'', the next factor is the contribution of σ'' itself, and the final two factors constitute the paths beyond σ''. Combining Eqs. (2.24) and (2.25), the total contribution from all σ'' on an energy scale e^{-Nd} is

$$\begin{aligned}\binom{Nx}{Ny} e^{-N\epsilon^2} \left(\frac{\Gamma}{N|\epsilon|}\right)^{Nx} (Ny)!(N(x-y))! \\ = (Nx)! \left(\frac{\Gamma}{N|\epsilon|}\right)^{Nx} e^{-N\epsilon^2} = e^{-N\gamma(x,\epsilon) - N\epsilon^2}.\end{aligned} \tag{2.26}$$

The total contribution is exponentially smaller than that from the typical paths, despite smaller energy denominators. This pattern repeats if one considers paths which pass through two exponentially close configurations, or three, and so on. We have shown that $V_{\text{eff}}(x, \epsilon)$ does indeed take the value $e^{-N\gamma(x,\epsilon)}$ in all realizations except for a vanishing fraction.

2.2.3 The high-temperature limit

The above analysis assumes that $\epsilon \neq 0$ and finds an eigenstate phase transition along a non-trivial curve $\Gamma_{\text{tun}}(\epsilon)$. Importantly, the curve is $O(1)$ with respect to system size. We now consider the situation for states $|\sigma\rangle$ in the middle of the spectrum, i.e., $E \sim O(\sqrt{N})$ rather than $O(N)$.

Simple scaling estimates make it clear that such states cannot be trapped at $\Gamma \sim O(1)$. Each energy denominator in Eq. (2.8) is typically $O(\sqrt{N})$, and thus one expects $\langle \sigma' | \Psi_\sigma \rangle$ to scale as

$$\langle \sigma' | \Psi_\sigma \rangle \sim (Nx)! \left(\frac{\Gamma}{\sqrt{N}}\right)^{Nx} \sim \left(\frac{x\Gamma\sqrt{N}}{e}\right)^{Nx}. \tag{2.27}$$

The scale on which the eigenstates delocalize is $\Gamma \sim O(N^{-1/2})$. Obviously, this analysis neglects fluctuations, and so we shall now be more careful.

Take E to be exactly 0 for simplicity, and consider a single path of length L (not necessarily $O(N)$). Denote the amplitude of the path by A:

$$|A| = \prod_{\sigma'' \in P} \frac{\Gamma}{|E(\sigma'')|}. \tag{2.28}$$

To simplify notation, we write this as

$$\ln |A| = L \ln \frac{\Gamma}{D} + Y, \tag{2.29}$$

where

$$D \equiv \frac{\sqrt{\pi N}}{2}, \tag{2.30}$$

$$Y \equiv \sum_{i=1}^{L} \ln \frac{D}{|E_i|}, \tag{2.31}$$

and the E_i are independent Gaussian random variables of variance $N/2$.

A single term in Eq. (2.31), denoted $y_i \equiv \ln D/|E_i|$, has distribution

$$P(y_i) = e^{-\frac{\pi}{4} e^{-2y} - y}, \tag{2.32}$$

which goes as e^{-y} for $y \gg 1$. The distribution $P(Y)$ is a convolution of L $P(y_i)$'s. Assuming $Y \gg 1$, the integration is dominated by having all $y_i \gg 1$, and thus we can evaluate the convolution:

$$P(Y) = \frac{Y^{L-1}}{(L-1)!} e^{-Y}. \tag{2.33}$$

Thus $|A| > 1$, i.e., $Y > Y_c \equiv L \ln \frac{D}{\Gamma}$, with probability

$$\Pr\big[|A| > 1\big] = \int_{Y_c}^{\infty} dY \frac{Y^{L-1}}{(L-1)!} e^{-Y} \sim \frac{Y_c^{L-1}}{(L-1)!} e^{-Y_c} \big(1 + O(Y_c^{-1})\big). \tag{2.34}$$

The expected number of paths to a given site which have large amplitudes is thus

$$L! \frac{Y_c^{L-1}}{(L-1)!} e^{-Y_c} \sim \left(L \frac{\Gamma}{D} \ln \frac{D}{\Gamma} \right)^L. \tag{2.35}$$

If the eigenstates are to remain trapped, Eq. (2.35) must remain less than 1 for all $L \leq N$ as $N \to \infty$. We have the condition

$$\frac{D}{\Gamma \ln \frac{D}{\Gamma}} \geq N, \tag{2.36}$$

which becomes, at large N,

$$\frac{D}{\Gamma} \geq N \ln N. \tag{2.37}$$

The transition from trapped to thermal eigenstates occurs when equality holds. Using the definition of D (Eq. (2.30)), we have that

$$\Gamma_{\text{tun}}(0) = \frac{\sqrt{\pi}}{2\sqrt{N}\ln N}. \tag{2.38}$$

The most important conclusion in this analysis is simply that perturbation theory breaks down for any $\Gamma \sim O(1)$ at infinite temperature. Note also that we did not specify any properties of the final state $|\sigma'\rangle$. Even typical configurations acquire large amplitudes once Γ exceeds $\Gamma_{\text{tun}}(0)$, in contrast with the finite-temperature case.

2.2.4 The large-field limit

Here we briefly describe the opposite limit to that in which our perturbative treatment holds: $\Gamma \gg 1$. We cannot make nearly as much progress in this limit, but we do gain some understanding from a simple analysis.

To zeroth order in H_{REM}, the eigenstates of the Hamiltonian are $\hat{\sigma}^x$ eigenstates with energies $-M\Gamma$ ($M = -N, -N+2, \cdots, N$). The degeneracy of the $-M\Gamma$ level is $\binom{N}{(N+M)/2}$. In this basis, the REM term is dense, i.e.,

$$\langle \sigma'^{(x)} | H_{\text{REM}} | \sigma^{(x)} \rangle = \frac{1}{2^N} \sum_{\sigma} (-1)^{\alpha(\sigma)} E(\sigma), \tag{2.39}$$

where the sum is over all 2^N $\hat{\sigma}^z$ eigenstates and $\alpha(\sigma)$ is either 0 or 1 depending on the specific states in question. The important feature is that every matrix element of H_{REM} in the $\hat{\sigma}^x$ basis is the sum and/or difference of all REM energies, divided by 2^N from normalization. Thus every element is a Gaussian random variable with mean and variance

$$\mathbb{E}\big[\, \langle \sigma'^{(x)} | H_{\text{REM}} | \sigma^{(x)} \rangle \,\big] = 0, \quad \mathbb{E}\big[\, \langle \sigma'^{(x)} | H_{\text{REM}} | \sigma^{(x)} \rangle^2 \,\big] = \frac{1}{2^N} \frac{N}{2}. \tag{2.40}$$

We shall treat H_{REM} as a GOE-distributed random matrix in this basis. However, keep in mind that this is only an approximation because the matrix elements are not strictly independent.

To leading order in perturbation theory (now with H_{REM} as the perturbation), the eigenstates within a subspace of fixed total magnetization M form a band according to Wigner's semi-circle law [22]. This band has a radius of

$$\sqrt{\frac{N}{2^{N+1}}} \sqrt{\binom{N}{\frac{N+M}{2}}} \sim N^{1/4}\, e^{N\left(-\frac{1+m}{4}\ln(1+m) - \frac{1-m}{4}\ln(1-m)\right)}, \tag{2.41}$$

where $m \equiv M/N$ is the average magnetization per spin. Note that the bandwidth is exponentially small for all $m \neq 0$, to be compared with the $O(\Gamma)$ separation between bands. Thus the eigenstates with $m \neq 0$ do not hybridize outside of their initial bands, and each state has a well-defined bulk magnetization. The only bands which do hybridize are those with $m \sim O(N^{-1/2})$.

Since the unperturbed energy densities are proportional to m, the large-Γ situation is analogous to the small-Γ situation: states at $\epsilon \sim O(N)$ (finite temperature) are only weakly dressed by all others, whereas states at $\epsilon = 0$ (infinite temperature) hybridize immediately even for an arbitrarily weak perturbation. However, it is difficult to carry out the large-Γ expansion to higher orders, and so we cannot see the eigenstate phase transition from this side.

2.3 Tunneling dynamics to solve the matching problem

There is much more to the dynamical behavior of a system than the structure of the eigenstates. In particular, our identification of thermal eigenstates in Sec. 2.2 does not give any information on the timescale over which an out-of-equilibrium initial state thermalizes. Here we study the explicit tunneling dynamics of the QREM, using the matching problems described in the Introduction as a concrete motivation.

Our interpretation of the $\hat{\sigma}^z$ eigenstates is slightly different in this section. Those at a specified energy density ϵ represent "marked" states which one is trying to locate out of all possible 2^N. The classical paramagnetic phase is the most interesting to study from this perspective: there are exponentially many marked states (although still an exponentially small fraction of the total configuration space), and the transverse field is not so strong as to wash out the energy landscape. Furthermore, the REM is in a sense the hardest problem of this type. Since the energy levels are independent, there is no pattern among the marked states which could be exploited.

Let us be more concrete about the protocol. We initialize the system in a given state $\hat{\sigma}^z$ state $|\sigma\rangle$ at energy density ϵ: $H_{\text{REM}}|\sigma\rangle = N\epsilon|\sigma\rangle$. The system then evolves under the QREM Hamiltonian. The matching problem is solved at time t if there is a significant probability of observing a different state $|\sigma'\rangle$ at the same *classical* energy density: $H_{\text{REM}}|\sigma'\rangle = N\epsilon|\sigma'\rangle$.

As mentioned in the Introduction, there are two reasons why one might expect this protocol to be efficient: conservation of energy biases the dynamics towards classical states having the same energy as the starting configuration, and quantum fluctuations can tunnel through the energy barriers that separate those states. However, Hamiltonian dynamics conserves the full quantum mechanical energy $\langle H\rangle$, whereas our goal is to find a state with the same classical energy $\langle H_{\text{REM}}\rangle$. Furthermore, the analysis in Sec. 2.2 has shown that the tunneling amplitudes between low-energy are exponentially suppressed. Thus the performance of quantum dynamics in matching problems, and its comparison to classical search algorithms, is non-trivial.

We find three sharp dynamical phases for the QREM, each with distinct implications for the matching problem. The phase diagram is shown in Fig. 2.6. At low ϵ and small Γ, the probability of the system tunneling between clusters vanishes in the thermodynamic limit even at arbitrarily late times. This is the

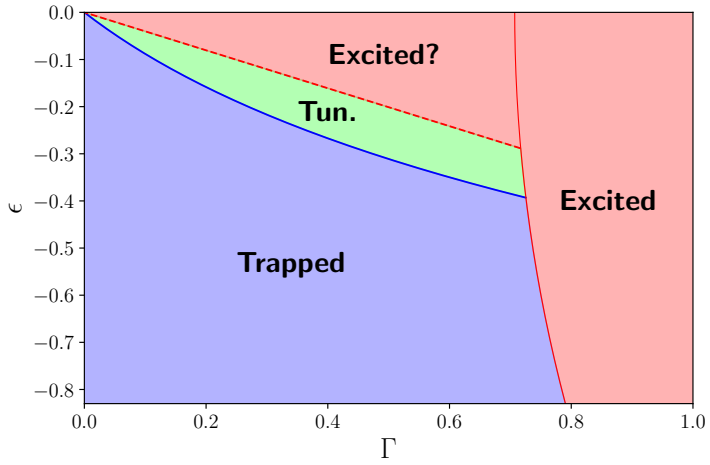

Figure 2.6: The dynamical phase diagram of the QREM. The system tunnels between clusters in the "tunneling" phase (green), remains trapped in a cluster in the "trapped" phase, and is excited out of clusters in the "excited" phase. The trapped, tunneling, and large-Γ excited phases have been confirmed numerically. It is unclear whether the small-Γ excited phase is truly an excited phase or a portion of the tunneling phase in which perturbation theory does not apply.

same "trapped" phase as identified in Sec. 2.2, and matching fails throughout it. At large Γ, the system moves freely out of the initial cluster but is excited to higher classical energies in return for magnetizing along the transverse field. Matching fails in this "excited" phase as well, since the system does not locate states at the desired classical energy. Only at intermediate ϵ and Γ, in the "tunneling" phase, does energy matching succeed by tunneling between clusters while preserving the classical energy density.

The timescale for tunneling is exponential in system size, i.e., quantum dynamics cannot solve the matching problem in polynomial time. On the other hand, classical algorithms also require exponential runtime in these models, and quantum dynamics runs exponentially *faster* than classical spin-flip Monte Carlo at equilibrium. We also compare to a non-local search algorithm in which new configurations are chosen independently at random (the "unstructured search"). The unstructured search is the best possible classical algorithm for matching in the REM since there are no correlations between energy levels. In the QREM, quantum dynamics can succeed as quickly as the unstructured search but no better. However, when we discuss the more realistic p-spin model in Chap. 4, we shall show that there, quantum dynamics is capable of outperforming the unstructured search (and thus all classical algorithms of which we are aware). Furthermore, the quantum algorithm presented here is directly implementable on current experimental platforms [96, 97].

Note that the tunneling phase does not exist at sufficiently low ϵ for the p-spin model. A uniform transverse field cannot solve the matching problem near the classical ground state regardless of the field strength and regardless of runtime.

As we did for the eigenstate phases, we derive these results using perturbation theory in Γ. The central quantities are again the distance-resolved density of states $e^{Ng(x,\epsilon'|\epsilon)}$ and the effective coupling $e^{-N\gamma(x,\epsilon'|\epsilon)}$. However, there are two subtleties which we did not encounter earlier. First, we must consider the energy density ϵ' of the final state as well as the energy density ϵ of the initial state, so as to check whether the system is excited to a different classical energy. Second, configurations with $\epsilon' = \epsilon$ lie only at those distances for which $g(x, \epsilon|\epsilon) > 0$. There is a minimum such distance, i.e., x must be greater than a certain $x^{**}(\epsilon)$, and we will impose this condition on x when relevant.

We shall first show that tunneling between two states occurs only if their classical energies differ by less than the effective coupling between them, i.e., if the states are resonant. This is exactly the condition for eigenstates to hybridize between the two. The requirement for tunneling to occur is thus

$$\max_{x\in[x^{**}(\epsilon),1-x^{**}(\epsilon)]} \left[g(x,\epsilon|\epsilon) - \gamma(x,\epsilon|\epsilon)\right] > 0, \tag{2.42}$$

(Tunneling condition)

as in Sec. 2.2, and the curve $\Gamma_{\text{tun}}(\epsilon)$ defines the boundary between the trapped and tunneling phases[3].

As the initial state evolves in time, the amplitude on any non-resonant state remains exponentially small, of order $e^{-2N\gamma(x,\epsilon'|\epsilon)}$. However, there are exponentially many such states. If the *total* amplitude on states with $\epsilon' \neq \epsilon$ is large, then those states will be observed at later times with high probability and the system excites into classical energy density ϵ'. The requirement for the classical energy density to be preserved is

$$\max_{x\in[0,1]} \left[\max_{\epsilon'} \left[g(x,\epsilon'|\epsilon) - 2\gamma(x,\epsilon'|\epsilon)\right]\right] < 0. \tag{2.43}$$

(Non-excitation condition)

The curve $\Gamma_{\text{exc}}(\epsilon)$ on which the left-hand side equals 0 defines the boundary between the tunneling and excited phases. There is an additional transition into the excited phase which coincides with the thermodynamic transition into a quantum paramagnetic phase at large Γ. We cannot detect this transition within perturbation theory, but we find clear evidence for it numerically as discussed in Sec. 2.4.1.

Eqs. (2.42) and (2.43) are necessary conditions for quantum dynamics to succeed at the matching problem. If both are satisfied, then the time required for matching is simply the inverse tunneling rate between states. We estimate the

[3]Along $\Gamma_{\text{tun}}(\epsilon)$, there exists an x for which $g(x,\epsilon) = \gamma(x,\epsilon)$, and one can show that $\gamma(x,\epsilon) > 0$ for all x. Thus the value of x at which equality holds is necessarily one for which $g(x,\epsilon) > 0$, and the requirement that $x \in [x^{**}(\epsilon), 1 - x^{**}(\epsilon)]$ is automatically fulfilled.

timescale τ_{q} using Fermi's golden rule with the effective coupling and distance-resolved density of states. We find that τ_{q} scales exponentially with exponent

$$\frac{1}{N}\ln\tau_{\mathrm{q}} = \min_{x\in[x^{**}(\epsilon),1-x^{**}(\epsilon)]}\left[2\gamma(x,\epsilon|\epsilon) - g(x,\epsilon|\epsilon)\right]. \tag{2.44}$$

(Tunneling timescale)

In Sec. 2.3.2, we shall compare this timescale against the runtimes for well-known classical algorithms.

2.3.1 The Schrieffer-Wolff transformation

We will continue to use the forward-scattering approximation (FSA) to make the perturbation theory tractable. However, we need additional formalism to explicitly describe time evolution, namely the Schrieffer-Wolff transformation [98].

Let $\mathcal{P}_0$ denote the subspace spanned by $\hat{\sigma}^z$ states having classical energy density ϵ, and let $\mathcal{Q}_0$ denote the orthogonal subspace. Note that the QREM Hamiltonian H couples $\mathcal{P}_0$ and $\mathcal{Q}_0$ through the transverse field, yet it does not directly couple different states in $\mathcal{P}_0$, as multiple spin-flips would be required. The Schrieffer-Wolff transformation is performed by a unitary operator e^{iS} such that $e^{iS}He^{-iS} \equiv H_{\mathrm{eff}}$ does not couple $\mathcal{P}_0$ and $\mathcal{Q}_0$, and instead does have a direct coupling between the states in $\mathcal{P}_0$, which is precisely $V_{\mathrm{eff}}(x,\epsilon)$ from Sec. 2.2. Since

$$\langle\sigma'|e^{-iHt}|\sigma\rangle = \langle\sigma'|\, e^{-iS}e^{-iH_{\mathrm{eff}}t}e^{iS}\,|\sigma\rangle\,, \tag{2.45}$$

the time evolution of $|\sigma\rangle$ into $|\sigma'\rangle$ under H is equivalent to the evolution of $e^{iS}\,|\sigma\rangle$ into $e^{iS}\,|\sigma'\rangle$ under H_{eff}.

To compute the generator S, let P_0 be the projector onto $\mathcal{P}_0$ and similarly for $Q_0 = 1 - P_0$. We determine S by requiring that $P_0H_{\mathrm{eff}}Q_0 = Q_0H_{\mathrm{eff}}P_0 = 0$. For brevity, denote the eigenstates of H_{REM} by $|i\rangle, |j\rangle, \ldots$ with corresponding energies $E_i, E_j, \ldots$. Also denote the transverse field term in the Hamiltonian simply as ΓV, so that $H = H_{\mathrm{REM}} + \Gamma V$.

First, decompose V into diagonal and off-diagonal parts:

$$\begin{aligned} V_d &\equiv P_0VP_0 + Q_0VQ_0, \\ V_{od} &\equiv P_0VQ_0 + Q_0VP_0. \end{aligned} \tag{2.46}$$

Next, define superoperators

$$\hat{S}(\,\cdot\,) \equiv [S\,,\,\cdot\,], \tag{2.47}$$

$$\mathcal{L}(\,\cdot\,) \equiv \sum_{\substack{i\in P_0\\ j\in Q_0}} \left(|i\rangle\,\frac{\langle i|\,\cdot\,|j\rangle}{E_i - E_j}\,\langle j| + |j\rangle\,\frac{\langle j|\,\cdot\,|i\rangle}{E_j - E_i}\,\langle i|\right), \tag{2.48}$$

where $\cdot$ denotes an arbitrary operator. Note that Eq. (2.48) only has off-block-diagonal matrix elements, and thus none of the energy denominators in the Schrieffer-Wolff formalism are small. With this notation, the condition that H_{eff} be block-diagonal gives an equation for the generator S:

$$S = \mathcal{L}\hat{S}(\Gamma V_d) - i\mathcal{L}\hat{S}\cot(\hat{S})(\Gamma V_{od}). \tag{2.49}$$

The effective Hamiltonian is

$$H_{\text{eff}} = H_0 + \Gamma V_d + i \tan\left(\frac{\hat{S}}{2}\right)(\Gamma V_{od}). \tag{2.50}$$

See [98] for the derivation.

Eq. (2.49) is naturally suited to an expansion in Γ:

$$S = \sum_{n=1}^{\infty} \Gamma^n S_n, \tag{2.51}$$

with each S_n a Hermitian operator. From Eq. (2.49),

$$\begin{aligned} S_1 &= -i\mathcal{L}(V_{od}), \\ S_2 &= \mathcal{L}\hat{S}_1(V_d), \\ S_n &= \mathcal{L}\hat{S}_{n-1}(V_d) \;-\; i\sum_{j=1}^{\infty} a_{2j} \sum_{\substack{n_1,\cdots,n_{2j}\geq 1 \\ n_1+\ldots+n_{2j}=n}} \mathcal{L}\hat{S}_{n_1}\cdots\hat{S}_{n_{2j}}(V_{od}), \end{aligned} \tag{2.52}$$

where the last line refers to $n \geq 3$, and a_{2j} is the $2j^{\text{th}}$ Taylor coefficient of $x\cot x$ about 0. Consider the first two orders:

$$iS_1 = \sum_{\substack{i\in P_0 \\ j\in Q_0}} \left(|i\rangle \frac{\langle i|V_{od}|j\rangle}{E_i - E_j} \langle j| + |j\rangle \frac{\langle j|V_{od}|i\rangle}{E_j - E_i} \langle i| \right), \tag{2.53}$$

$$\begin{aligned} iS_2 = &\sum_{\substack{i\in P_0 \\ j\in Q_0 \\ k\in Q_0}} \left(|i\rangle \frac{\langle i|V_{od}|j\rangle \langle j|V_d|k\rangle}{(E_i - E_k)(E_i - E_j)} \langle k| - |k\rangle \frac{\langle k|V_d|j\rangle \langle j|V_{od}|i\rangle}{(E_k - E_i)(E_j - E_i)} \langle i| \right) \\ &+ \sum_{\substack{i\in P_0 \\ j\in P_0 \\ k\in Q_0}} \left(|i\rangle \frac{\langle i|V_d|j\rangle \langle j|V_{od}|k\rangle}{(E_i - E_k)(E_j - E_k)} \langle k| - |k\rangle \frac{\langle k|V_{od}|j\rangle \langle j|V_d|i\rangle}{(E_k - E_i)(E_k - E_j)} \langle i| \right). \end{aligned} \tag{2.54}$$

It becomes very tedious to write higher-order terms, yet one already sees the structure of the expansion. Each term in S_n has a numerator which is a string of matrix elements of V and a denominator which is a string of energy differences. Note that each matrix element can be either V_d or V_{od}, and each energy denominator is between a state in P_0 and a state in Q_0. The same structure holds when we insert the expansion of S into Eq. (2.50) and obtain an expansion of H_{eff} in powers of Γ. For example, two of the fourth-order terms in H_{eff} are

$$\begin{aligned} H_{\text{eff}} = \cdots &+ \frac{\Gamma^4}{2} |i\rangle \frac{\langle i|V_{od}|j\rangle \langle j|V_d|k\rangle \langle k|V_d|l\rangle \langle l|V_{od}|m\rangle}{(E_i - E_l)(E_i - E_k)(E_i - E_j)} \langle m| \\ &+ \frac{\Gamma^4}{2} |i\rangle \frac{\langle i|V_d|j\rangle \langle j|V_{od}|k\rangle \langle k|V_d|l\rangle \langle l|V_{od}|m\rangle}{(E_i - E_l)(E_i - E_k)(E_j - E_k)} \langle m| + \cdots . \end{aligned} \tag{2.55}$$

Thus far, all that we have presented is completely general. Now we show how the above equations, which are ultimately used to determine H_{eff}, are considerably simplified by making the FSA. It is best to first consider a simple toy problem, a 1D nearest-neighbor tight-binding model with open boundary conditions:

$$H = \sum_{i=0}^{L} E_i \left|i\right\rangle \left\langle i\right| - \Gamma \sum_{i=0}^{L-1} \Big(\left|i\right\rangle \left\langle i+1\right| + \left|i+1\right\rangle \left\langle i\right| \Big). \tag{2.56}$$

Suppose that E_0 and E_L are much lower than all other E_i, and we want to study tunneling from site 0 to site L. We take P_0 to project onto $|0\rangle$ and $|L\rangle$, V to be the hopping term, and aim to compute $\langle 0|H_{\text{eff}}|L\rangle$ to lowest order in Γ.

The lowest-order terms are $O\big(\Gamma^L\big)$, since at least L applications of the hopping term are required to couple $|0\rangle$ and $|L\rangle$. However, alongside those L^{th}-order terms which do couple $|0\rangle$ and $|L\rangle$, there are many L^{th}-order terms in H_{eff} which do not. Only terms for which the operator string is $V_{od}{V_d}^{L-2}V_{od}$ contribute to $\langle 0|H_{\text{eff}}|L\rangle$ at L^{th} order, since $\{|0\rangle, |L\rangle\} \in P_0$ and $\{|1\rangle, \ldots, |L-1\rangle\} \in Q_0$. For example, taking $L = 4$, the first term in Eq. (2.55) does contribute to $\langle 0|H_{\text{eff}}|4\rangle$ at 4^{th} order (taking $i = 0$, $j = 1$, etc.) but the second term does not.

In fact, only two terms at L^{th} order have the correct operator string:

$$\begin{aligned}\langle 0|H_{\text{eff}}|L\rangle \sim \frac{\Gamma^L}{2} \Bigg(&\frac{\langle 0|V_{od}|1\rangle \langle 1|V_d|2\rangle \cdots \langle L-2|V_d|L-1\rangle \langle L-1|V_{od}|L\rangle}{(E_0 - E_1)(E_0 - E_2)\cdots(E_0 - E_{L-2})(E_0 - E_{L-1})} \\ &+ \frac{\langle 0|V_{od}|1\rangle \langle 1|V_d|2\rangle \cdots \langle L-2|V_d|L-1\rangle \langle L-1|V_{od}|L\rangle}{(E_L - E_1)(E_L - E_2)\cdots(E_L - E_{L-2})(E_L - E_{L-1})} \Bigg).\end{aligned} \tag{2.57}$$

If $E_0 = E_L$, the final expression is particularly simple:

$$\langle 0|H_{\text{eff}}|L\rangle \sim \Gamma \prod_{i=1}^{L-1} \frac{\Gamma}{E_0 - E_i}. \tag{2.58}$$

Compare to Eq. (2.11) from Sec. 2.2.2 (noting that the toy problem has only one path from 0 to L).

Finally, let us apply this analysis to the QREM. As always, let the distance between $|\sigma\rangle$ and $|\sigma'\rangle$ be x. $\langle \sigma'|H_{\text{eff}}|\sigma\rangle \sim O\big(\Gamma^{Nx}\big)$, and although there are many more terms at Nx^{th} order than in the toy problem, the same arguments hold here. Each surviving term has an operator string of the form $V_{od}{V_d}^{Nx-2}V_{od}$, with the intermediate states constituting a sequence of spin-flips transforming σ into σ'. Thus

$$\langle \sigma'|H_{\text{eff}}|\sigma\rangle \equiv V_{\text{eff}}(x, \epsilon) = \Gamma \sum_{P} \prod_{\sigma'' \in P} \frac{\Gamma}{E - E(\sigma'')}, \tag{2.59}$$

as before. The FSA in the context of Schrieffer-Wolff gives exactly the same expression for the effective coupling as it does in eigenstate perturbation theory.

One might worry about the paths which pass through other states in P_0, giving operator strings $V_{od}{V_d}^{Ny-2}{V_{od}}^2{V_d}^{N(x-y)-2}V_{od}$. However, such paths are

an exponentially small fraction of the total, and thus negligible: out of the $(Nx)!$ paths from σ to σ', the expected number[4] with at least one intermediate configuration having energy density ϵ scales as $Ne^{-N\epsilon^2}(Nx)!$. Note that these atypical paths do not have amplitudes large enough to compensate for the smaller quantity, as the Schrieffer-Wolff formalism ensures that there are no resonant denominators.

Now that we have studied H_{eff}, it remains to consider $e^{iS}|\sigma\rangle$, since this is the state which we evolve under H_{eff}. Write

$$e^{iS}|\sigma\rangle = \cos(S)|\sigma\rangle + i\sin(S)|\sigma\rangle, \tag{2.60}$$

and note from Eq. (2.52) that, order by order, S is off-block-diagonal. Thus $\cos(S)|\sigma\rangle$ lies in $\mathcal{P}_0$ and $\sin(S)|\sigma\rangle$ lies in $\mathcal{Q}_0$. These two components remain in their respective subspaces under time evolution because H_{eff} is block-diagonal.

First, we shall calculate the weight of $\cos(S)|\sigma\rangle$ on $|\sigma'\rangle \in \mathcal{P}_0$. We will continue to work within the FSA, meaning that we compute $\langle\sigma'|\cos(S)|\sigma\rangle$ to lowest non-zero order in Γ. By the same arguments as above, the relevant terms again have the operator string $V_{od}V_d{}^{Nx-2}V_{od}$, which all come from $\frac{1}{2}S^2$ in the expansion of $\cos(S)$. Unlike above, however, there are more terms: the string in the first factor of S must begin on $|\sigma\rangle$ but can terminate on any intermediate $|\sigma''\rangle$, and the string in the second factor must then begin at $|\sigma''\rangle$ and terminate on $|\sigma'\rangle$. Thus

$$\langle\sigma'|\cos(S)|\sigma\rangle \sim \frac{1}{2}\sum_{\sigma''}\sum_{P_{\sigma''}}\prod_{\sigma'''\in P_{\sigma''}}\frac{\Gamma}{N\big(\epsilon-\epsilon(\sigma''')\big)}. \tag{2.61}$$

The outer sum is over all $|\sigma''\rangle$ intermediate between $|\sigma\rangle$ and $|\sigma'\rangle$. The inner sum is over paths $P_{\sigma''}$ that pass through $|\sigma''\rangle$.

Given the analysis from Sec. 2.2, we may take $\epsilon(\sigma''') \to \mathbb{E}\big[\epsilon(\sigma''')\big] = 0$, and

$$\begin{aligned}\big|\langle\sigma'|\cos(S)|\sigma\rangle\big| &\sim \int_0^x N\mathrm{d}y\binom{Nx}{Ny}(Ny)!\big(N(x-y)\big)!\left(\frac{\Gamma}{N|\epsilon|}\right)^{Nx}\\ &= Nx\big(Nx\big)!\left(\frac{\Gamma}{N|\epsilon|}\right)^{Nx} \sim Nxe^{-N\gamma(x,\epsilon)},\end{aligned} \tag{2.62}$$

with $\gamma(x,\epsilon)$ as defined in Eq. (2.10). The extra factor of Nx does not modify the exponential scaling and can be neglected. To obtain the total weight on all $|\sigma'\rangle \in \mathcal{P}_0$, we multiply $e^{-2N\gamma(x,\epsilon)}$ by the distance-resolved density of states $e^{Ng(x,\epsilon)}$ and integrate over all $x \in \big[x^{**}(\epsilon), 1-x^{**}(\epsilon)\big]$. The result is $e^{-Nr(\epsilon)}$ with

$$r(\epsilon) = \min_{x\in[x^{**}(\epsilon),1-x^{**}(\epsilon)]}\big[2\gamma(x,\epsilon) - g(x,\epsilon)\big]. \tag{2.63}$$

We shall show in Sec. 2.3.2 that $r(\epsilon) > 0$ throughout the relevant portions of the phase diagram. This affords us a useful simplification. Since $\cos(S)|\sigma\rangle$ has

[4]By Markov's inequality (see Chap. 3), a typical sample cannot have more than a finite factor times the expected number of paths as $N \to \infty$.

exponentially small weight on all other states $|\sigma'\rangle$, we can take $\cos(S)|\sigma\rangle \sim |\sigma\rangle$ when calculating transition probabilities.

Next, we analogously calculate $\langle\sigma'|\sin(S)|\sigma\rangle$ for $|\sigma'\rangle \in \mathcal{Q}_0$. The forward-scattering operator strings are of the form $V_d{}^{Nx-1}V_{od}$, which come from S in the expansion of $\sin(S)$. There is only one such term in Eq. (2.52), giving

$$\langle\sigma'|\sin(S)|\sigma\rangle \sim \sum_P \prod_{\sigma''\in P} \frac{\Gamma}{N\big(\epsilon-\epsilon(\sigma'')\big)} = \frac{V_{\text{eff}}(x,\epsilon'|\epsilon)}{N\big(\epsilon-\epsilon'\big)}, \tag{2.64}$$

where we have again identified the effective coupling $V_{\text{eff}}(x,\epsilon'|\epsilon)$, now between states at different classical energy densities.

2.3.2 Tunneling rates

We now have enough ingredients to understand the tunneling dynamics in the QREM. The distance-resolved density of states $e^{Ng(x,\epsilon'|\epsilon)}$ was computed using simple combinatorics in Sec. 2.2.2:

$$g(x,\epsilon'|\epsilon) = -x\ln x - (1-x)\ln(1-x) - \epsilon'^2. \tag{2.65}$$

Note that the ϵ variable is superfluous because the states at distance x are uncorrelated with ϵ (it will be useful to keep the label nevertheless). The effective coupling, Eq. (2.59), is computed straightforwardly by taking all $\epsilon(\sigma'') \to 0$, a simplification justified in Sec. 2.2.2. One obtains $V_{\text{eff}}(x,\epsilon'|\epsilon) \sim e^{N\gamma(x,\epsilon'|\epsilon)}$ with

$$\gamma(x,\epsilon'|\epsilon) = -x\ln\frac{x\Gamma}{e|\epsilon|}. \tag{2.66}$$

Here the ϵ' variable is superfluous because the intermediate states along the paths are uncorrelated with it (ϵ enters through the energy denominators).

For brevity, we will often write $g(x,\epsilon)$ and $\gamma(x,\epsilon)$ in place of $g(x,\epsilon'|\epsilon)$ and $\gamma(x,\epsilon'|\epsilon)$. We have also defined $x^{**}(\epsilon)$ by

$$-x^{**}\ln x^{**} - (1-x^{**})\ln(1-x^{**}) - \epsilon^2 = 0. \tag{2.67}$$

Thus $g(x,\epsilon) > 0$ only for $x \in \big[x^{**}(\epsilon), 1-x^{**}(\epsilon)\big]$, i.e., configurations at energy density ϵ lie only within that interval.

Consider two states $|\sigma\rangle$ and $|\sigma'\rangle$ both at energy density ϵ. The effective Hamiltonian has a direct matrix element $V_{\text{eff}}(x,\epsilon)$ between them, and, as noted above, we can take $\cos(S)|\sigma\rangle \sim |\sigma\rangle$ and $\cos(S)|\sigma'\rangle \sim |\sigma'\rangle$. Thus time-dependent perturbation theory [95] immediately gives the transition probability from $|\sigma\rangle$ to $|\sigma'\rangle$:

$$P_{\sigma'\sigma}(t) \equiv \big|\,\langle\sigma'|e^{-iHt}|\sigma\rangle\,\big|^2 = \frac{4V_{\text{eff}}(x,\epsilon)^2}{N^2\big(\epsilon(\sigma')-\epsilon(\sigma)\big)^2}\sin^2\left(\frac{N\big(\epsilon(\sigma')-\epsilon(\sigma)\big)t}{2}\right). \tag{2.68}$$

It is important that we do not set $\epsilon(\sigma')$ exactly equal to $\epsilon(\sigma)$. The smallest energy difference among all σ' is typically of the order of level spacing, which

may be either smaller or larger than $V_{\text{eff}}(x,\epsilon)$ since both scale exponentially with N. The level spacing among $|\sigma'\rangle$ at distance x scales as $e^{-Ng(x,\epsilon)}$, and so if $g(x,\epsilon) < \gamma(x,\epsilon)$, then Eq. (2.68) is exponentially small for every final state at distance x. Furthermore, the total weight on all states at distance x, obtained by summing $P_{\sigma'\sigma}(t)$ over all $|\sigma'\rangle$ having the specified energy density and distance, is exponentially small: those $|\sigma'\rangle$ for which $\epsilon(\sigma') - \epsilon(\sigma) \sim e^{-Nd}$ give a total contribution $e^{-2N\gamma+2Nd} \cdot e^{Ng-Nd} = e^{-2N\gamma+Ng+Nd}$, which increases with d until the smallest possible spacing at $d = g$. Thus the probability of transitioning to any state at distance x vanishes in the thermodynamic limit, for all times t.

Since the states with energy density ϵ lie at distances $x \in \big[x^{**}(\epsilon), 1-x^{**}(\epsilon)\big]$, if $g(x,\epsilon) < \gamma(x,\epsilon)$ for all such x then the system never transitions into a different state, even on exponentially long timescales. This gives the tunneling condition presented above as a necessary condition for quantum dynamics to succeed in matching:

$$\max_{x\in[x^{**}(\epsilon),1-x^{**}(\epsilon)]} \big[g(x,\epsilon) - \gamma(x,\epsilon)\big] > 0. \tag{2.42}$$

(Tunneling condition)

Using Eqs. (2.65) and (2.66), the tunneling condition becomes

$$\max_{x\in[x^{**}(\epsilon),1-x^{**}(\epsilon)]} \left[x \ln \frac{\Gamma}{e|\epsilon|} - (1-x)\ln(1-x) - \epsilon^2\right] > 0. \tag{2.69}$$

We located the curve $\Gamma_{\text{tun}}(\epsilon)$ on which equality holds in Sec. 2.2.2. It now has the interpretation not only of the phase boundary between trapped and thermal eigenstates, but also of the boundary between frozen and tunneling dynamics.

If Eq. (2.42) is satisifed, then Fermi's golden rule gives the *rate* at which the system tunnels between clusters. To ensure that we handle the exponentially small scales in the level spacing and effective coupling correctly, we present a derivation here. Consider $|\sigma'\rangle$ at distance x and fixed time t. If $N\big|\epsilon(\sigma') - \epsilon(\sigma)\big| \ll t^{-1}$, then $P_{\sigma'\sigma}(t)$ behaves as $e^{-2N\gamma(x,\epsilon)}t^2$. If $N\big|\epsilon(\sigma') - \epsilon(\sigma)\big| \gg t^{-1}$ then $P_{\sigma'\sigma}(t)$ has already reached its maximum value and begun oscillating. Thus the portion of the weight at distance x which is growing with time, denoted $P_{\text{tun}}(x,t)$, is obtained by summing $P_{\sigma'\sigma}(t)$ over $|\sigma'\rangle$ with $\big|\epsilon(\sigma') - \epsilon(\sigma)\big| \lesssim (Nt)^{-1}$. To exponential order,

$$P_{\text{tun}}(x,t) \sim \left(e^{-2N\gamma(x,\epsilon)}t^2\right)\left(e^{Ng(x,\epsilon)}t^{-1}\right) = e^{-N\left(2\gamma(x,\epsilon)-g(x,\epsilon)\right)}t, \tag{2.70}$$

from which the tunneling rate is apparent. The rate τ_{q}^{-1} at which the system exits its initial state is given by integrating over x, which since $P_{\text{tun}}(x,t)$ scales exponentially gives the result stated above:

$$\frac{1}{N}\ln\tau_{\text{q}} = \min_{x\in[x^{**}(\epsilon),1-x^{**}(\epsilon)]} \big[2\gamma(x,\epsilon) - g(x,\epsilon)\big]. \tag{2.44}$$

(Tunneling timescale)

Note that the tunneling rate is equal to the weight of the transformed state $\cos(S)\,|\sigma\rangle$ on other $|\sigma'\rangle$ (Eq. (2.63)). The field strength at which the transformed

state no longer resembles $|\sigma\rangle$ is exactly the strength at which the tunneling rate is $O(1)$ regardless. If the tunneling rate is $O(1)$, our use of perturbation theory is questionable. Furthermore, we shall show momentarily that the system enters its excited phase before this occurs. Thus it is justified to take $\cos(S)|\sigma\rangle \sim |\sigma\rangle$ throughout the entire tunneling phase, as claimed.

Perturbation theory breaks down if the transverse field is too large, which we see through the weight of $e^{iS}|\sigma\rangle$ in the $\mathcal{Q}_0$ subspace. This weight corresponds to probability that the system will be observed to have a different classical energy density ϵ'. From Eq. (2.64), the weight of $e^{iS}|\sigma\rangle$ on a single $|\sigma'\rangle$ is of order $e^{-N\gamma(x,\epsilon'|\epsilon)}$ (the energy denominator is by definition not small and does not affect the exponential scaling). Thus the total weight in the $\mathcal{Q}_0$ subspace is

$$\int_0^1 \mathrm{d}x \int \mathrm{d}\epsilon' \left| \langle\sigma'|e^{iS}|\sigma\rangle \right|^2 e^{Ng(x,\epsilon'|\epsilon)} \sim \int_0^1 \mathrm{d}x \int \mathrm{d}\epsilon' \, e^{N\left(g(x,\epsilon'|\epsilon)-2\gamma(x,\epsilon'|\epsilon)\right)}. \tag{2.71}$$

The result must be exponentially small if perturbation theory is to be valid. This is the non-excitation condition given above:

$$\max_{x\in[0,1]} \left[\max_{\epsilon'} \left[g(x,\epsilon'|\epsilon) - 2\gamma(x,\epsilon'|\epsilon) \right] \right] < 0. \tag{2.43}$$

(Non-excitation condition)

For the REM, the maximization over ϵ' is trivial and we have the requirement

$$\max_{x\in[0,1]} \left[2x \ln \frac{\Gamma}{e|\epsilon|} + x\ln x - (1-x)\ln(1-x) \right] < 0. \tag{2.72}$$

Strictly speaking, violation of Eq. (2.43) only means that the perturbation theory is inconsistent. However, it has an immediate physical interpretation: the system excites out of its initial state and into higher classical energy densities. This corresponds to another failure mechanism for the matching problem, as a measurement of the system will not yield the desired energy density.

Finally, we present clear numerical evidence in Sec. 2.4.1 that the first-order thermodynamic transition into a quantum paramagnetic phase is relevant for the Hamiltonian dynamics. It is itself an excitation transition in which the system excites to classical energy density 0, and is another breakdown of matching.

We have obtained two necessary conditions for quantum dynamics to succeed in the matching problem. If Eq. (2.42) is violated, the system never escapes its initial states. If Eq. (2.43) is violated (or the first-order line is crossed), the system excites to higher energies and does not return. Generically, satisfying both conditions requires that the transverse field be neither too strong nor too weak, and this regime may be narrow or non-existent depending on ϵ and the model in question. Indeed, Fig. 2.6 shows that one cannot satisfy both conditions at low ϵ in the QREM.

2.3.3 Comparison to classical algorithms

The rate of tunneling between states, when it occurs at all, is always exponentially slow in system size. This is clear from the expressions for the rate

(Eq. (2.44)) and the non-excitation condition (Eq. (2.43)): if Eq. (2.43) is satisfied, then $N^{-1} \ln \tau_{\mathrm{q}}$ in Eq. (2.44) is necessarily positive since it optimizes over fewer variables. Thus quantum dynamics cannot succeed at matching in polynomial time. However, it may be exponentially *faster* than simple classical algorithms. We now show this for the QREM, by comparing the tunneling rate found above to the equilibration timescale for stochastic (e.g., Monte Carlo) dynamics. We then additionally compare to an unstructured search algorithm in which new configurations are chosen randomly.

Stochastic dynamics can be used for matching problems as follows: from a starting configuration $|\sigma\rangle$, run a Monte Carlo simulation at the temperature T corresponding to $\epsilon(\sigma)$ by Legendre transform. Since the temperature is properly chosen, one will observe a configuration having the same energy density at later times with high probability. However, the later configuration will in fact be the initial one unless one waits long enough for the system to be thermally activated over the energy barriers that separate states. This activation timescale is the time required for Monte Carlo dynamics to succeed in energy matching.

It is straightforward to calculate the activation timescale in the REM. The N neighboring configurations to a given $|\sigma\rangle$ all have energy density 0 with high probability, as follows from Eq. (2.1). Thus in a Monte Carlo simulation with single-spin update rules (e.g., Metropolis), the simulation time required to leave state $|\sigma\rangle$ is $e^{N\beta|\epsilon(\sigma)|}$. Recall that the thermodynamic entropy density of the REM is

$$s(\epsilon) = \ln 2 - \epsilon^2, \tag{1.34}$$

from which it follows that $\beta(\epsilon) = -2\epsilon$. The activation timescale in the REM starting from energy density ϵ is therefore

$$\tau_{\mathrm{th}} \sim e^{2N\epsilon^2}. \tag{2.73}$$

Note that there is another method of matching which is particularly trivial: ignore the given $|\sigma\rangle$ and pick a new configuration $|\sigma'\rangle$ uniformly out of all possible 2^N, check if $\epsilon(\sigma') = \epsilon$, and repeat until true. The probability of selecting a $|\sigma'\rangle$ with the correct energy density is $e^{Ns(\epsilon)}/2^N$ (and the event that $|\sigma'\rangle = |\sigma\rangle$ is unlikely), thus the timescale τ_{unstr} for this unstructured search is

$$\tau_{\mathrm{unstr}} \sim e^{N\epsilon^2}. \tag{2.74}$$

Clearly $\tau_{\mathrm{unstr}} \ll \tau_{\mathrm{th}}$, and indeed, the unstructured search is the most efficient *classical* algorithm for the QREM since the energy levels are completely independent.

The tunneling timescale τ_{q} from Sec. 2.3.2 also scales exponentially with N and is given by Eq. (2.44). Using the explicit expressions for $\gamma(x, \epsilon)$ and $g(x, \epsilon)$,

$$\frac{1}{N} \ln \tau_{\mathrm{q}} = \min_{x \in [x^{**}(\epsilon), 1 - x^{**}(\epsilon)]} \left[-2x \ln \frac{\Gamma}{e|\epsilon|} - x \ln x + (1-x) \ln (1-x) + \epsilon^2 \right]. \tag{2.75}$$

It is straightforward to evaluate Eq. (2.75) numerically.

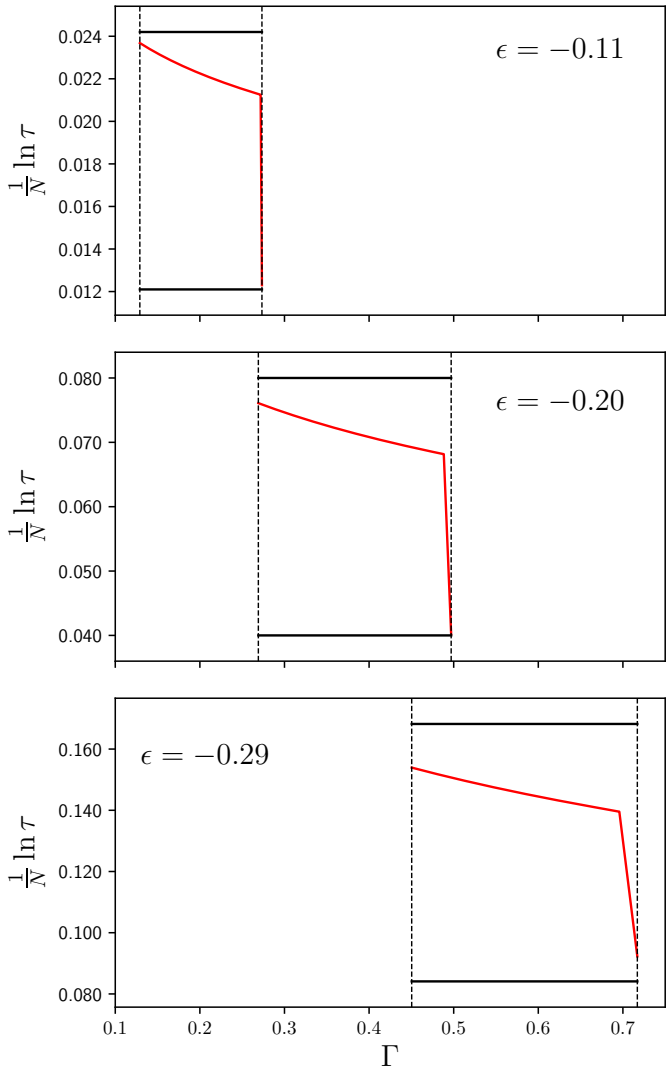

Figure 2.7: Timescales for matching in the QREM, as a function of Γ at the indicated ϵ. In each panel, the red curve is τ_{q}, the upper black curve is τ_{th}, and the lower black curve is τ_{unstr}. The left dashed line is the location of the tunneling transition and the right dashed line is the location of the excitation transition. τ_{q} is meaningful only in between the two. The non-analyticity in τ_{q} comes from a change in the argmin of Eq. (2.75).

Fig. 2.7 shows the tunneling timescale as a function of Γ at representative values of ϵ, alongside the activation and unstructured timescales. Tunneling is exponentially faster than thermal activation at matching problems. One can check that this is true for all ϵ and Γ in the tunneling phase of the QREM. Tunneling can even match the unstructured search precisely on the excitation boundary $\Gamma_{\text{exc}}(\epsilon)$: since the classical energies are independent and $\gamma(x, \epsilon'|\epsilon)$ does not depend on ϵ' in the QREM,

$$\begin{aligned} \frac{1}{N} \ln \tau_{\text{q}} &= \min_{x \in [x^{**}(\epsilon), 1-x^{**}(\epsilon)]} \left[2\gamma(x, \epsilon) - g(x, \epsilon) \right] \\ &= \min_{x \in [x^{**}(\epsilon), 1-x^{**}(\epsilon)]} \left[\min_{\epsilon'} \left[2\gamma(x, \epsilon'|\epsilon) - g(x, \epsilon'|\epsilon) \right] \right] + \epsilon^2, \end{aligned} \tag{2.76}$$

and the first term on the right-hand side is 0 by definition on $\Gamma_{\text{exc}}(\epsilon)$[5].

Unfortunately, this derivation also shows that tunneling never performs *better* than the unstructured search. However, we make another comparison when considering the p-spin model in Chap. 4. In that model, even at large p, we find that tunneling is faster than the unstructured search in a sliver of the tunneling phase. The p-spin model is more realistic than the REM because there are correlations between the energy levels. Those correlations enhance the tunneling amplitude to states at energy density ϵ relative to those at $\epsilon' > \epsilon$, giving quantum dynamics an edge over the unstructured search. We are not aware of any classical algorithm which has a similar advantage, at least for large p where the correlations are minimal.

The lesson is that quantitative comparisons of different algorithms do depend on the specific model in question. This does somewhat limit the utility of studying toy models like the REM and the p-spin model, but on the other hand, our results make clear that quantum dynamics can be competitive at matching problems in non-trivial case studies.

2.4 Numerical validation of results

The purpose of this section is to present numerical evidence supporting the picture developed above. Our primary technique is exact diagonalization, in which we generate realizations of the QREM Hamiltonian in Eq. (1.39) for finite N and compute the eigenvectors numerically. The procedure is computationally intensive, and we are limited to very small system sizes ($N \leq 14$). We also perform numerical calculations within the FSA, by generating realizations of H_{REM} and evaluating Eq. (2.8) for $\langle \sigma' | \Psi_\sigma \rangle$ numerically. We are able to access larger but still limited sizes in this way ($N \leq 20$). Regardless of the finite-N limitations, we unambiguously confirm the phase diagrams in Figs. 2.2 and 2.6.

There is one subtle point which has been glossed over thus far. According to all the diagnostics which we shall present, the trapped phase of the QREM

[5]Strictly speaking, on the excitation boundary the maximum over all $x \in [0, 1]$ is 0. However, one can check that the maximum in fact lies within $[x^{**}(\epsilon), 1 - x^{**}(\epsilon)]$.

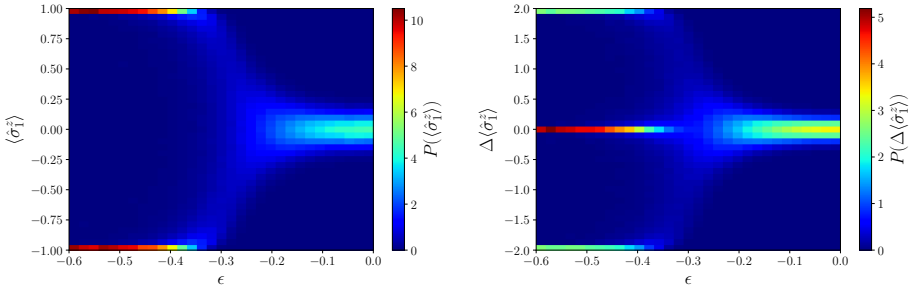

Figure 2.8: (Left) Probability density function for the eigenstate magnetization of spin 1, as a function of energy density. (Right) Probability density function for the difference in magnetization between adjacent eigenstates in the spectrum, as a function of energy density. In both panels, each vertical slice is a separate probability distribution, obtained by generating a histogram over eigenstates within an energy window centered on the indicated ϵ. These distributions are at $\Gamma = 0.20$ and $N = 14$, with energy density windows $\delta\epsilon = 0.02$.

constitutes many-body localization. Indeed, the QREM was initially considered to be a mean-field model for MBL [90, 92]. However, we shall make clear in Chap. 4 that the trapped phase of the p-spin model, for which the QREM is the $p \to \infty$ limit, is decidedly not many-body localized. It is thus better to think of the trapped phase in the QREM as a particularly frozen limit of the p-spin model.

2.4.1 Exact diagonalization

The exact diagonalization results serve two purposes. First, they confirm that the eigenstates of the QREM are trapped at small fields and (by standard diagnostics) thermal at large fields. Second, they illustrate the three distinct dynamical phases: trapped, tunneling, and excited.

A particularly transparent method for studying eigenstate thermalization or the lack thereof is to examine the single-spin magnetization of individual eigenstates, i.e., $\langle\hat{\sigma}_i^z\rangle$ with the expectation value taken in an eigenstate. In an ETH phase, the magnetization is 0 for every eigenstate and every spin i. In the trapped phase, the magnetization is either 1 or -1 depending on the specific eigenstate and spin in question. One cannot simply average $\langle\hat{\sigma}_i^z\rangle$ over realizations because the random sign in the trapped phase would average to 0. Yet there are two straightforward fixes. First, one can study the histogram of $\langle\hat{\sigma}_i^z\rangle$ obtained by looking at all eigenstates in a small energy window. The histogram of magnetization *differences* between eigenstates and their neighbors in the spectrum gives further confirmation as to whether $\langle\hat{\sigma}_i^z\rangle$ varies erratically between states. Fig. 2.8 presents examples of these distributions. Second, one can instead average $|\langle\hat{\sigma}_i^z\rangle|$ over realizations. Fig. 2.9 shows the result for a represen-

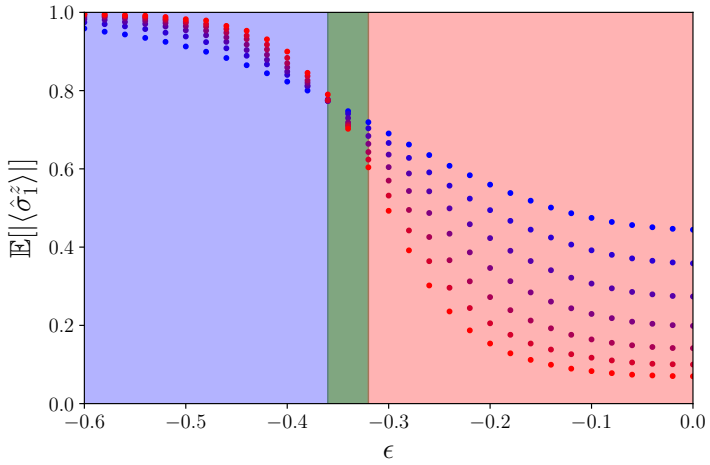

Figure 2.9: The disorder-averaged magnitude of the eigenstate single-spin magnetization, as determined via exact diagonalization, as a function of the eigenstate energy density. These results are taken at $\Gamma = 0.20$, from $N = 8$ (blue) to $N = 14$ (red). The average is also over all eigenstates within an energy density window of size 0.02. Statistical errorbars are smaller than the marker widths. The background shading corresponds to the predicted phase at that energy density: red is ETH, blue is trapped, and green is the transition region as determined by spectral statistics.

tative value of Γ. Both approaches support the same conclusion: the eigenstates of the QREM are trapped at low energies and thermal at high energies.

Note that in Fig. 2.9, the most important feature is not the numerical values of $|\langle\hat{\sigma}_i^z\rangle|$ but where they tend to as the system size increases. At low ϵ, $|\langle\hat{\sigma}_i^z\rangle|$ increases towards 1 as N increases. At high ϵ, $|\langle\hat{\sigma}_i^z\rangle|$ decreases towards 0. This strongly suggests that a transition between two phases is occuring at a critical energy density. We will be looking primarily for the same feature in most of the diagnostics presented below.

Spectral statistics provide another standard tool for distinguishing eigenstate phases. As discussed in the Introduction, the level spacing distribution in an ETH phase is that of the GOE. Non-thermal phases, in contrast, typically show Poisson-distributed level spacings. We use three quantities to characterize the distribution. The ratio of adjacent gaps is denoted r:

$$r_n \equiv \min\left[\frac{E_{n+1}-E_n}{E_n-E_{n-1}}, \frac{E_n-E_{n-1}}{E_{n+1}-E_n}\right], \tag{2.77}$$

where E_n is the n^{th} energy level of the Hamiltonian, and we compute the average of r_n over realizations and states within an energy window. $\mathbb{E}[r] \approx 0.53$ in the GOE and $\mathbb{E}[r] \approx 0.39$ for the Poisson distribution [31]. The fraction of level

spacings which are smaller than half the mean is denoted I_1, and the fraction which are greater than twice the mean is denoted I_2 [99]. Since anomalously small and large spacings are both suppressed in the GOE, I_1 and I_2 are both smaller in the GOE than in the Poisson distribution. We normalize them by the difference:

$$J_1 \equiv \frac{I_1 - I_1^{(\mathrm{GOE})}}{I_1^{(\mathrm{Pois})} - I_1^{(\mathrm{GOE})}}, \quad J_2 \equiv \frac{I_2 - I_2^{(\mathrm{GOE})}}{I_2^{(\mathrm{Pois})} - I_2^{(\mathrm{GOE})}}. \tag{2.78}$$

Thus J_1 and J_2 change from 0 to 1 as one passes from a thermal to a non-thermal phase.

Fig. 2.10 shows numerical results on the three quantities for the QREM. They all tend to the Poisson value at low ϵ and the GOE value at high ϵ as N increases. Furthermore, the transition region is consistent with that seen in the magnetization curves.

We also consider the eigenstate structure in the configuration space, namely the number of $\hat{\sigma}^z$ states on which a given eigenstate has significant amplitude. In the trapped phase, given the analysis in Sec. 2.2.2, we expect this number to be close to 1. In the ETH phase, it should be exponentially large. A natural quantity to compute is the inverse participation ratio (IPR) [55]. Given an eigenstate $|\Psi\rangle$ in the $\hat{\sigma}^z$ basis, the IPR Y_2 is defined as

$$Y_2 \equiv \sum_{\sigma} \big|\, \langle \sigma | \Psi \rangle \,\big|^4. \tag{2.79}$$

Note that if $|\Psi\rangle$ is itself a basis state $|\sigma'\rangle$, then $Y_2 = 1$, whereas if $|\Psi\rangle$ is uniformly distributed over all states (i.e., $|\Psi\rangle = 2^{-N/2} \sum_\sigma |\sigma\rangle$), then $Y_2 = 2^{-N}$. Thus the IPR is roughly one over the number of basis states on which $|\Psi\rangle$ is distributed (the inverse of the participation number, hence the name).

Fig. 2.11 gives an example of the IPR as a function of ϵ, at the same value of Γ used for Figs. 2.9 and 2.10. We again see the expected behavior: the log-IPR divided by N tends to 0 at low ϵ (Y_2 is sub-exponential), and tends away from 0 at high ϵ (Y_2 is exponentially small). The location of the transition region agrees reasonably well with the other diagnostics (given the small system sizes, we are not concerned with small discrepancies).

Taken together, these exact diagonalization results paint a clear picture of the eigenstate phases in the QREM, one which agrees with the understanding developed in Sec. 2.2. The numerics give us separate finite-size estimates of the phase boundary. We plot them alongside the theoretical curve in Fig. 2.2. While the agreement is not perfect, we do expect significant finite-size effects: the theoretical analysis relies on taking $N \to \infty$ to control rare fluctuations and the competition between exponentials, whereas the numerical results are restricted to $N \leq 14$, hardly the thermodynamic limit. Thus we view the comparison in Fig. 2.2 as quite satisfactory.

Finally, we study the tunneling dynamics of the QREM explicitly through exact diagonalization, so as to confirm the dynamical phases discussed in Sec. 2.3.

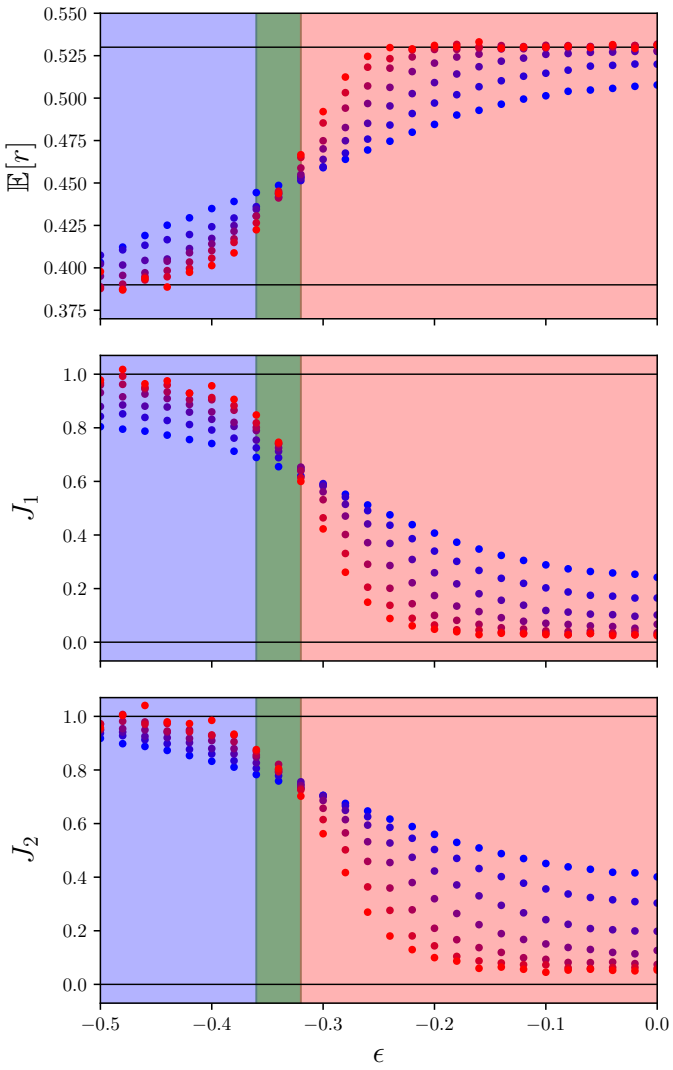

Figure 2.10: Spectral statistics in the QREM as a function of energy density. All data is at $\Gamma = 0.20$, and N ranges from 8 (blue) to 14 (red). The bin size for energy densities is 0.02. Statistical errorbars are comparable to the marker widths. The horizontal black lines show the GOE and Poisson values for each quantity. The background shading corresponds to the predicted phase at that energy density: red is ETH, blue is trapped, and green is the transition region.

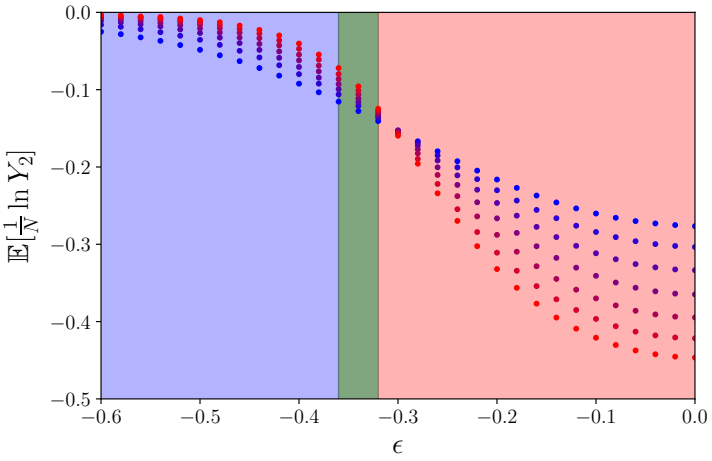

Figure 2.11: The disorder-averaged logarithm of the IPR, normalized by system size, as a function of the eigenstate energy density. These results are taken at $\Gamma = 0.20$, and N ranges from 8 (blue) to 14 (red). The average is also over all eigenstates within an energy density window of size 0.02. Statistical errorbars are smaller than the marker widths. The background shading corresponds to the predicted phase at that energy density: red is ETH, blue is trapped, and green is the transition region as determined by spectral statistics.

For each realization of the QREM Hamiltonian, we perform a "quench" simulation: find the $\hat{\sigma}^z$ eigenstate $|\sigma\rangle$ with classical energy density closest to a specified ϵ, then compute $|\Psi(t)\rangle \equiv e^{-iHt}|\sigma\rangle$. We evaluate two observables at time t, denoted $\hat{x}$ and $\hat{\epsilon}$, which are the operators corresponding respectively to the distance from $|\sigma\rangle$ and the classical energy density (both are diagonal in the $\hat{\sigma}^z$ basis).

Results for $\langle\Psi(t)|\hat{x}|\Psi(t)\rangle$ and $\langle\Psi(t)|\hat{\epsilon}|\Psi(t)\rangle$ are shown in Fig. 2.12. Both quantities reach saturated values, denoted x_∞ and ϵ_∞. For all Γ and ϵ, x_∞ lies between 0 and 1/2 and ϵ_∞ lies between ϵ and 0. Since we study finite-size systems, the dependence on the parameters is smooth. The difference between the three dynamical phases is in the flow of x_∞ and ϵ_∞ as N increases.

- Trapped phase: $x_\infty \to 0$ and $\epsilon_\infty \to \epsilon$.
- Tunneling phase: $x_\infty \to 1/2$ and $\epsilon_\infty \to \epsilon$.
- Excited phase: $x_\infty \to 1/2$ and $\epsilon_\infty \not\to \epsilon$.

In Fig. 2.12, the behavior of the system is consistent with the trapped phase at small Γ (top panels), the tunneling phase at intermediate Γ (middle panels), and the excited phase at large Γ (bottom panels). Furthermore, it appears that the timescale on which the system approaches x_∞ is indeed exponential with N in the tunneling phase.

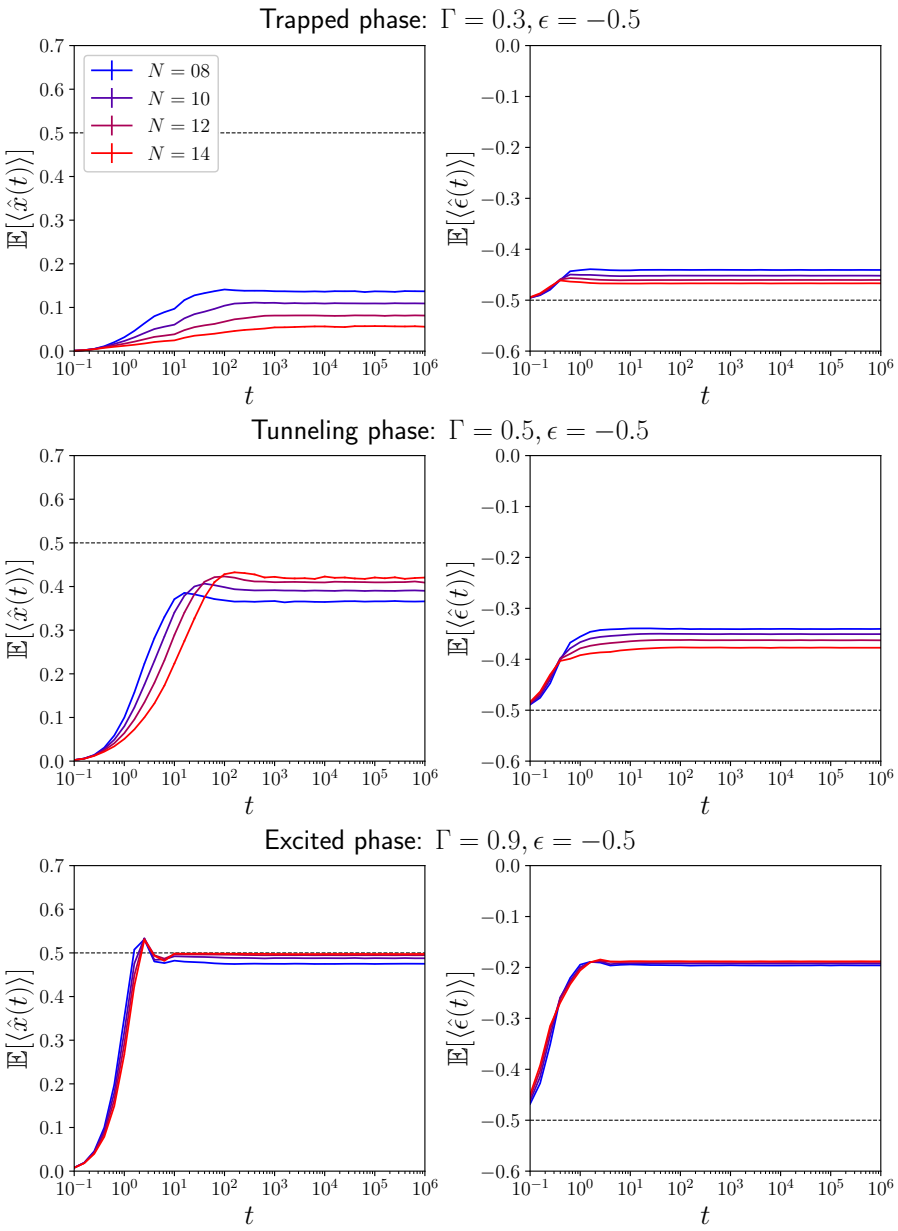

Figure 2.12: Quench dynamics in the QREM, at the indicated Γ and ϵ. (Left) Average distance relative to the initial configuration, $\mathbb{E}\big[\langle \hat{x}(t) \rangle\big] \equiv \mathbb{E}\big[\, \langle \Psi(t)|\hat{x}|\Psi(t)\rangle \,\big]$. The dashed line is $x = 1/2$. (Right) Average classical energy density, $\mathbb{E}\big[\langle \hat{\epsilon}(t) \rangle\big] \equiv \mathbb{E}\big[\, \langle \Psi(t)|\hat{\epsilon}|\Psi(t)\rangle \,\big]$. The dashed line is the initial energy density ϵ. Statistical errorbars are smaller than the linewidths.

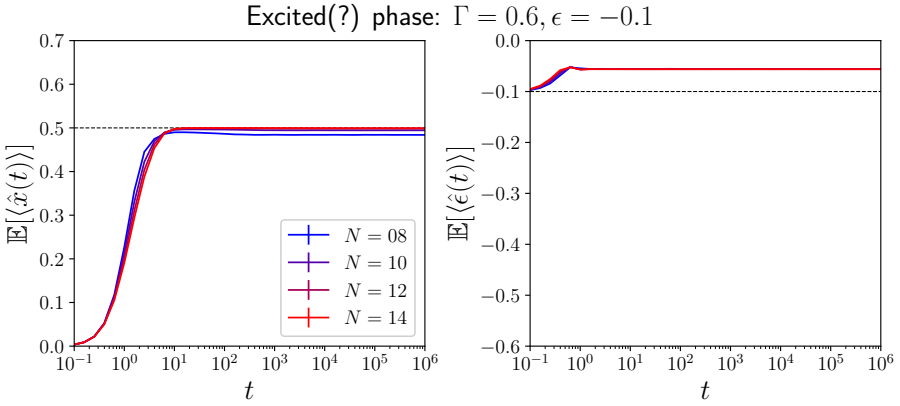

Figure 2.13: Quench dynamics in the QREM, at the indicated Γ and ϵ. The dynamical behavior is ambiguously in between that of the tunneling and excited phases. It is uncertain which it will tend to as N increases. (Left) Average distance relative to the initial configuration, $\mathbb{E}\big[\langle \hat{x}(t) \rangle\big] \equiv \mathbb{E}\big[\, \langle \Psi(t)|\hat{x}|\Psi(t)\rangle \,\big]$. The dashed line is $x = 1/2$. (Right) Average classical energy density, $\mathbb{E}\big[\langle \hat{\epsilon}(t) \rangle\big] \equiv \mathbb{E}\big[\, \langle \Psi(t)|\hat{\epsilon}|\Psi(t)\rangle \,\big]$. The dashed line is the initial energy density ϵ. Statistical errorbars are smaller than the linewidths.

The middle panels, which show behavior consistent with the tunneling phase, are at a (Γ, ϵ) point which Fig. 2.6 predicts is in the trapped phase. There are two possible explanations for the discrepancy. First, we cannot rule out that the system becomes trapped at larger system sizes. Our analytical arguments focus only on the leading exponential order of the quantities relevant for computing the phase boundaries, and polynomial prefactors may lead to significant finite-size effects for $N \leq 14$. Second, since the analysis of Sec. 2.3 is based on perturbation theory in Γ, it may only be quantitatively correct at small Γ. Regardless, the observed behavior is consistent with the other numerical results on the eigenstate properties.

We are unable to conclusively identify the small-Γ portion of the excited phase shown in Fig. 2.6. Fig. 2.13 plots $\langle \Psi(t)|\hat{x}|\Psi(t)\rangle$ and $\langle \Psi(t)|\hat{\epsilon}|\Psi(t)\rangle$ for a (Γ, ϵ) point well within that region of the phase diagram. $x_\infty = 1/2$ as expected, signifying that the system is not trapped within a cluster. However, ϵ_∞ shows a slight downward flow as N increases, and it is not clear whether the timescale on which the system approaches x_∞ is scaling exponentially or sub-exponentially. It is possible that the system is excited out of clusters, but it may instead be in the tunneling phase with very strong finite-size effects.

Regardless, we do find strong signatures of all three dynamical phases at lower ϵ, as shown in Fig. 2.12.

2.4.2 Numerical forward-scattering

Given a realization of H_{REM}, we can calculate many of the same diagnostics as above using the forward-scattering expression in Eq. (2.8) for the eigenstates. In particular, we have computed the single-spin magnetization and the IPR, averaged over many realizations. We have also measured the probability that a given realization yields resonances in the forward-scattering expansion. Note that the energy density ϵ is a tunable parameter within this framework, and we can study the dependence of quantities on ϵ without needing to bin and average over eigenstates.

By construction, the FSA is unable to describe the ETH phase. Our goals for the numerical forward-scattering calculations are focused on the trapped eigenstate phase. We aim to confirm that the perturbation theory becomes more valid at sufficiently low energies as N increases (e.g., the probability of resonances decreases, the IPR approaches 1, etc.). We also hope to detect the energy at which the perturbation theory breaks down and compare this estimate for the phase transition to the estimate from exact diagonalization.

Fig. 2.14 gives representative results from the forward-scattering calculations. The picture is largely the same as that from exact diagonalization. All diagnostics are consistent with trapped eigenstates at low energies and show a clear transition as ϵ increases. There are a couple of minor points to note. First, keep in mind that the results are meaningless in the ETH phase. They indicate only that the perturbation theory has become invalid. Second, for these calculations we take the unperturbed state $|\sigma\rangle$ to have all spins pointing down (without loss of generality), and thus can average the magnetization directly without taking a modulus.

The forward-scattering estimate for the phase transition is plotted in Fig. 2.2 alongside the exact diagonalization estimate and the analytic curve. We see that forward-scattering and exact diagonalization are in very good agreement at small Γ, and start to deviate at larger Γ. This is expected, given that the FSA is based on perturbation theory in Γ. Furthermore, the same caveat about finite-size effects applies here: even within the FSA, our numerics are limited to $N \leq 20$. We also compare the IPR computed within the FSA to exact diagonalization in the bottom panel of Fig. 2.14. The two agree quite well inside the trapped phase. These results provide strong evidence that perturbation theory and even the FSA give a suitable description of trapped eigenstates.

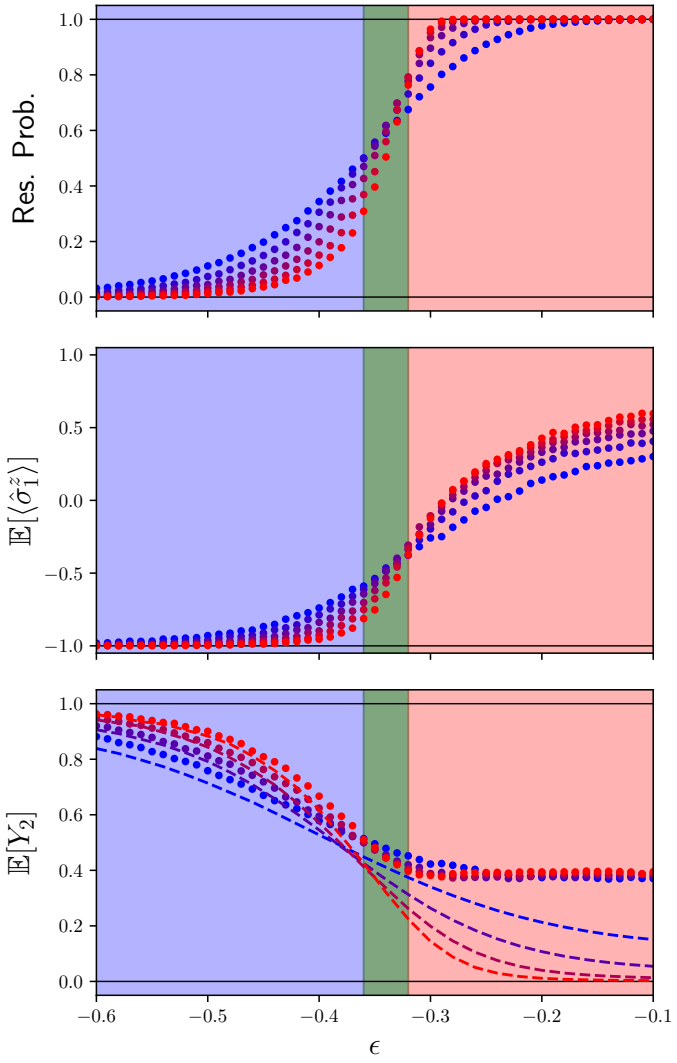

Figure 2.14: Diagnostics for trapped eigenstates in the QREM, computed within the FSA, as a function of energy density and system size. All data is at $\Gamma = 0.20$. (Top) Probability of resonances. N ranges from 10 (blue) to 20 (red). (Middle) Single-spin magnetization. N ranges from 10 (blue) to 20 (red). (Bottom) IPR. N ranges from 8 (blue) to 14 (red). The markers are forward-scattering data, and the dashed lines are exact diagonalization data for comparison. In all panels, statistical errorbars are smaller than the marker size. The shading indicates the phase as predicted by exact diagonalization: red is ETH, blue is trapped, and green is the transition region.

Chapter 3

Rugged energy landscapes and the clustering phenomenon

The main drawback to the random energy model is that the energy levels are independent. Any model that is expressed in terms of interactions among degrees of freedom, as all physical models and optimization problems are, has correlations between levels. In this sense, the p-spin model discussed in the Introduction is a more realistic toy model that remains semi-tractable. Recall that the p-spin model has Hamiltonian

$$H_p = \sum_{(i_1 \cdots i_p)} J_{i_1 \cdots i_p} \sigma^z_{i_1} \cdots \sigma^z_{i_p}, \tag{1.27}$$

where each coupling $J_{i_1 \cdots i_p}$ is Gaussian-distributed with mean 0 and variance $\frac{p!}{2N^{p-1}}$. The energy levels are then Gaussian-distributed themselves with moments

$$\mathbb{E}\big[H_p(\sigma)\big] = 0, \quad \mathbb{E}\big[H_p(\sigma) H_p(\sigma')\big] = \frac{N}{2}\Big(1 - 2x(\sigma, \sigma')\Big)^p. \tag{3.1}$$

We consider the quantum model obtained by including a transverse field in Chap. 4. This chapter focuses entirely on the classical model and develops a detailed understanding of the energy landscape. Many of the dynamical properties will then follow rather quickly.

3.1 Clustering in the p-spin model

The p-spin model is a prototypical model for rugged energy landscapes. Fig. 3.1 shows the simplest yet most ubiquitous cartoon of such a landscape. The potential energy has many local minima with large energy barriers in between. Note that if one specifies a sufficiently low energy ϵ, those positions at or below ϵ form

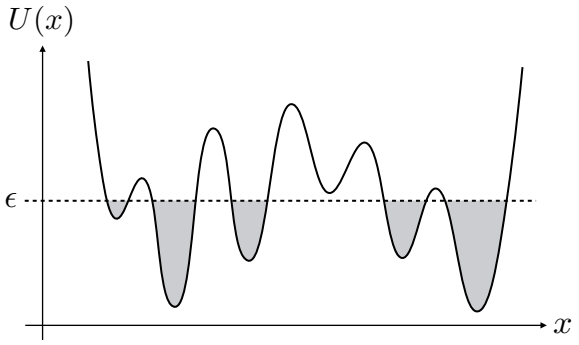

Figure 3.1: A one-dimensional example of a rugged energy landscape $U(x)$. States with energy below the dashed line form disconnected clusters (shaded).

disconnected regions referred to as "clusters". $H_p(\sigma)$ plays a role analogous to the potential energy $U(x)$. Although the geometry of configuration space is much more complicated than that of a line, much of the physics which we shall discuss can be understood with Fig. 3.1 in mind.

In the $\hat{\sigma}^z$ configuration space, we say that two configurations σ and σ' are connected if there is a sequence of spin flips transforming one into the other (analogous to moving along x in Fig. 3.1) which incurs only $O(1)$ changes in energy throughout the process. For a given σ, the set of σ' to which it is connected defines a cluster. The motivation for these definitions is that, heuristically, stochastic dynamics such as Glauber or Metropolis Monte Carlo quickly explores within a cluster but requires much longer times to transition between them. In many physical and computational problems, including the p-spin model, the number and geometry of clusters transitions sharply at certain energy densities.

The relevant transitions for this thesis are sketched in Fig. 3.2. The center of the spectrum, corresponding to infinite temperature, is at energy density $\epsilon = 0$, and the bottom is at a finite negative energy density ϵ_{GS}. In between, transitions occur at ϵ_d and ϵ_s. They are best understood in terms of two order parameters. The Edwards-Anderson order parameter quantifies *dynamical* ergodicity-breaking, e.g., in a Monte Carlo simulation run for time t:

$$q_{\text{EA}} \equiv \lim_{t\to\infty} \lim_{N\to\infty} \mathbb{E}\Big[\Big\langle N^{-1} \sum_i \sigma_i(t)\sigma_i(0)\Big\rangle\Big]. \tag{3.2}$$

The angular brackets denote a thermal average over $\sigma(0)$ and an average over the randomness of the dynamics. The order parameter that quantifies *equilibrium* ergodicity-breaking is in terms of "replicas", i.e., copies of the system that are

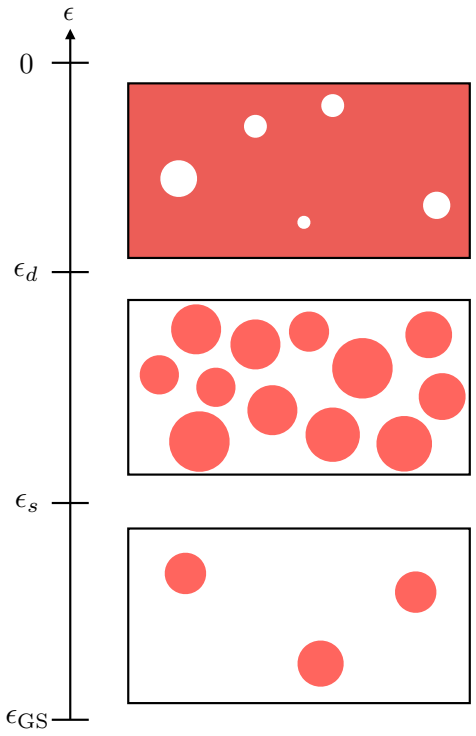

Figure 3.2: Important transitions in the classical p-spin model. Each box represents the configuration space of N spin-1/2s, and the red areas represent the regions of configuration space that contain states of energy density ϵ. Top: $\epsilon_d < \epsilon < 0$, middle: $\epsilon_s < \epsilon < \epsilon_d$, bottom: $\epsilon_{\mathrm{GS}} < \epsilon < \epsilon_s$.

uncoupled from each other but have the same disorder realization:

$$q \equiv \lim_{N\to\infty} \mathbb{E}\Big[\Big\langle \big|N^{-1}\sum_i \sigma_i^\alpha \sigma_i^\beta\big| \Big\rangle\Big]. \tag{3.3}$$

The superscripts α and β denote different replicas and the angular brackets denote independent thermal averages over σ^α and σ^β. Note that $N^{-1}\sum_i \sigma_i^\alpha \sigma_i^\beta$, the "overlap" between α and β, is simply $1 - 2x(\sigma^\alpha, \sigma^\beta)$. Two configurations chosen uniformly out of all possible 2^N will have $q = 0$ ($x = 1/2$) with probability 1. In a finite-temperature paramagnetic phase, q remains at 0. In any ordered phase, whether ferromagnetic or spin-glass, $q \neq 0$.

Now we turn to the relevant phases of the p-spin model.

- $\epsilon_d < \epsilon < 0$: $q_{\mathrm{EA}} = 0$, $q = 0$. A randomly selected pair of states at such ϵ is connected with probability 1 (in the thermodynamic limit). The corre-

sponding cluster spans the configuration space, in the sense that the overlap between a randomly selected pair is 0 with probability 1 and stochastic dynamics equilibrates throughout the space.

- $\epsilon_s < \epsilon < \epsilon_d$: $q_{\mathrm{EA}} \neq 0$, $q = 0$. Typical states are no longer connected, and instead the number of clusters scales exponentially with N. The timescale for transitioning between clusters is exponential in N. In particular, it diverges in the thermodynamic limit, hence q_{EA} is non-zero. Nonetheless, the clusters are distributed throughout the configuration space. A randomly selected pair of states belong to different clusters and the overlap is still 0.

- $\epsilon_{\mathrm{GS}} < \epsilon < \epsilon_s$: $q_{\mathrm{EA}} \neq 0$, $q \neq 0$. The number of clusters is $O(1)$ with respect to N. A randomly selected pair of states has finite probability of belonging to the same cluster, which occupies only a small region of the configuration space. This finite-probability event produces a non-zero average overlap, i.e., $q \neq 0$.

The transition at ϵ_d is called the "dynamical" or "clustering" transition, as it marks the energy density (or corresponding temperature) below which stochastic dynamics fails to equilibrate the system. The transition at ϵ_s is called the "static" transition, as it is where the equilibrium order parameter becomes non-trivial.

The REM exhibits all these features itself, although it usually is not discussed in such terms. One connects between the REM and the p-spin model by using the intuition that individual configurations in the REM correspond to clusters in the p-spin model (we show this explicitly in Sec. 3.3). Thus the static transition ϵ_s, in which the system freezes onto $O(1)$-many clusters, is exactly the glass transition discussed in the Introduction for the REM, in which the system freezes onto $O(1)$-many configurations. Although we will not do so here, one can calculate q for the REM and show that it becomes non-zero at the glass transition temperature.

One might think that the REM has no analogue to ϵ_d, but in fact, *all* finite-temperature configurations lie below the dynamical transition. In other words, $\epsilon_d = 0$ for the REM. As we noted in the Introduction, every state σ with $\epsilon < 0$ has neighbors which are at energy density 0 (i.e., infinite temperature). Thus σ is disconnected from all others having the same energy density, and q_{EA} is trivially 1 at any finite temperature.

The interval (ϵ_s, ϵ_d) is many ways the most interesting, despite (or rather because of) being thermodynamically paramagnetic. There are exponentially many clusters scattered throughout the configuration space, but it is a highly non-trivial problem to find them. Much of Chap. 4 will be devoted to studying the tunneling amplitudes between clusters when a transverse field is applied. We will use the results to draw conclusions about the ability of quantum dynamics to locate clusters faster than classical algorithms, exactly as we did for the REM in Chap. 2.

3.2 Two inequalities

Before studying the geometry of clusters quantitatively, it will be useful to have two basic inequalities with which to bound the probabilities of rare fluctuations.

The first inequality is Markov's: given a *non-negative* random variable $\mathcal{N}$,

$$\Pr\big[\mathcal{N} \geq A\big] \leq \frac{\mathbb{E}\big[\mathcal{N}\big]}{A}. \tag{3.4}$$

It is straightforward to prove Eq. (3.4). Define $\mathcal{M}(\mathcal{N})$ to be A if $\mathcal{N} \geq A$ and 0 if $0 \leq \mathcal{N} < A$ (we assumed that $\mathcal{N} < 0$ never occurs). Note that $\mathcal{M}(\mathcal{N}) \leq \mathcal{N}$ regardless of the value of $\mathcal{N}$, and thus $\mathbb{E}[\mathcal{M}] \leq \mathbb{E}[\mathcal{N}]$. Since $\mathbb{E}[\mathcal{M}] = A\Pr[\mathcal{N} \geq A]$, we have Eq. (3.4).

The utility of Eq. (3.4) is its generality: it applies to any non-negative random variable, regardless of the distribution or how the variable is defined.

The second inequality is Chebyshev's: given *any* random variable $\mathcal{N}$,

$$\Pr\Big[\big|\mathcal{N} - \mathbb{E}[\mathcal{N}]\big| \geq k\mathbb{E}[\mathcal{N}]\Big] \leq \frac{\mathrm{Var}\big[\mathcal{N}\big]}{k^2\mathbb{E}[\mathcal{N}]^2}. \tag{3.5}$$

To prove Eq. (3.5), note that $(\mathcal{N} - \mathbb{E}[\mathcal{N}])^2$ is non-negative and thus Markov's inequality applies to it. The average is $\mathrm{Var}[\mathcal{N}]$ by definition, and the statement that $|\mathcal{N} - \mathbb{E}[\mathcal{N}]| \geq k\mathbb{E}[\mathcal{N}]$ is equivalent to $(\mathcal{N} - \mathbb{E}[\mathcal{N}])^2 \geq k^2\mathbb{E}[\mathcal{N}]^2$.

As a first use of these inequalities, we can make the analysis of the REM in the Introduction completely rigorous. Let $\mathcal{N}(\epsilon)$ be the number of configurations having an energy density within $\mathrm{d}\epsilon$ of ϵ for a single realization of the REM. We can write

$$\mathcal{N}(\epsilon) = \sum_{\sigma} \Theta\big(|\epsilon(\sigma) - \epsilon| < \mathrm{d}\epsilon\big), \tag{3.6}$$

where $\Theta(\,\cdot\,)$ is 1 if the argument is true and 0 if false. Then

$$\mathbb{E}\big[\mathcal{N}(\epsilon)\big] = 2^N P_1(\epsilon)\, 2\mathrm{d}\epsilon = 2\sqrt{\frac{N}{\pi}} e^{Ns(\epsilon)}\mathrm{d}\epsilon, \tag{3.7}$$

where $P_1(\epsilon)$ is the probability distribution of ϵ (Eq. (1.32)) and

$$s(\epsilon) = \ln 2 - \epsilon^2. \tag{3.8}$$

Since $\mathcal{N}(\epsilon)$ is by definition non-negative, Markov's inequality applies, in particular that

$$\Pr\big[\mathcal{N}(\epsilon) \geq 1\big] \leq \mathbb{E}\big[\mathcal{N}(\epsilon)\big] = 2\sqrt{\frac{N}{\pi}} e^{Ns(\epsilon)}\mathrm{d}\epsilon. \tag{3.9}$$

If $|\epsilon| > \sqrt{\ln 2}$, $s(\epsilon) < 0$ and the right-hand side is exponentially small. Thus the probability of any configuration having energy density ϵ must be exponentially small (or smaller), and it vanishes in the thermodynamic limit. We have shown that the spectrum of the REM lies within $[-N\sqrt{\ln 2}, N\sqrt{\ln 2}]$ with certainty as $N \to \infty$.

Now suppose that $|\epsilon| < \sqrt{\ln 2}$, so that $\mathbb{E}[\mathcal{N}(\epsilon)]$ is exponentially large. Since the different terms in Eq. (3.6) are independent for the REM,

$$\mathrm{Var}\big[\mathcal{N}(\epsilon)\big] = 2^N P_1(\epsilon)\, 2\mathrm{d}\epsilon \left(1 - P_1(\epsilon)\, 2\mathrm{d}\epsilon\right) \sim 2^N P_1(\epsilon)\, 2\mathrm{d}\epsilon = \mathbb{E}\big[\mathcal{N}(\epsilon)\big]. \quad (3.10)$$

Chebyshev's inequality then gives

$$\Pr\Big[\big|\mathcal{N}(\epsilon) - \mathbb{E}[\mathcal{N}(\epsilon)]\big| \geq k\mathbb{E}[\mathcal{N}(\epsilon)]\Big] \leq \frac{1}{k^2 \mathbb{E}[\mathcal{N}(\epsilon)]}. \quad (3.11)$$

The right-hand side is exponentially small, regardless of k. Thus the probability of $\mathcal{N}(\epsilon)$ deviating from the mean value by any finite fraction vanishes in the thermodynamic limit. We have shown that $\mathcal{N}(\epsilon)$ equals $\mathbb{E}[\mathcal{N}(\epsilon)]$ up to subleading corrections. In particular, the entropy density equals $s(\epsilon)$ with certainty as $N \to \infty$.

A *single* realization of the REM has all configurations lying within the interval of energy densities $[-\sqrt{\ln 2}, \sqrt{\ln 2}]$, and has entropy density $\ln 2 - \epsilon^2$ within that interval. At this point, we can proceed to study the thermodynamics exactly as in the Introduction, now with the assurance that we are indeed studying the properties of individual realizations.

3.3 The Franz-Parisi potential

3.3.1 Definition

We need a tool with which to *quantitatively* study the energy landscape of the p-spin model. The distance-resolved density of states from Chap. 2 serves this purpose well. We shall retain the notation from before, and denote the density of states by $\mathcal{N}(x, \epsilon'|\epsilon) \equiv e^{N g(x,\epsilon'|\epsilon)}$. Written out,

$$\mathcal{N}(x, \epsilon'|\epsilon) = \sum_{\sigma'} \delta_{x,x(\sigma,\sigma')} \delta\big(\epsilon' - \epsilon(\sigma')\big)_{\epsilon(\sigma)=\epsilon}, \quad (3.12)$$

where the subscript indicates that we must condition on σ having energy density ϵ. This conditioning did not enter into the analysis of the REM because the energy levels were independent. Furthermore, proofs analogous to that in Sec. 3.2 meant that we could use the average value of $\mathcal{N}(x, \epsilon'|\epsilon)$ in place of typical values. Neither simplification holds in the p-spin model. It is standard to disorder-average $g(x, \epsilon'|\epsilon)$ as opposed to $\mathcal{N}(x, \epsilon'|\epsilon)$:

$$\mathbb{E}\big[g(x, \epsilon'|\sigma, \epsilon)\big] = \frac{1}{N}\mathbb{E}\Big[\ln \mathrm{Tr}_{\sigma'}\big[\delta_{x,x(\sigma,\sigma')}\, \delta\big(\epsilon' - \epsilon(\sigma')\big)\big]\Big]_{\epsilon(\sigma)=\epsilon}. \quad (3.13)$$

The subscript again indicates conditioning. Generically, the fluctuations in $g(x, \epsilon'|\epsilon)$ between realizations are small even when those in $\mathcal{N}(x, \epsilon'|\epsilon)$ are not. Thus we will often write g in place of $\mathbb{E}[g]$ and leave the disorder-averaging implied.

$g(x, \epsilon'|\epsilon)$ is closely related to the Franz-Parisi potential (FPP), which is an important tool in the analysis of mean-field disordered systems [100–102]. In fact, Eq. (3.13) is essentially the FPP written in the microcanonical ensemble. The FPP as defined in the literature is

$$v(x, \beta'|\beta) = \mathbb{E}\left[\mathrm{Tr}_\sigma\left[\frac{e^{-N\beta\epsilon(\sigma)}}{Z(\beta)} \ln \mathrm{Tr}_{\sigma'}\left[\delta_{x,x(\sigma,\sigma')} e^{-N\beta'\epsilon(\sigma')}\right]\right]\right], \tag{3.14}$$

where $Z(\beta)$ is the partition function. $v(x, \beta'|\beta)$ represents the free energy of a system at inverse temperature β' which is constrained to be at distance x from a system in equilibrium at inverse temperature β.

Before moving on, let us briefly establish the relationship between $v(x, \beta'|\beta)$ and $g(x, \epsilon'|\epsilon)$. First consider

$$\mathbb{E}\left[\mathrm{Tr}_\sigma\left[\frac{e^{-N\beta\epsilon(\sigma)}}{Z(\beta)} f(\sigma)\right]\right], \tag{3.15}$$

for a function $f(\sigma)$ growing slower than exponential with N but otherwise arbitrary. The trace is dominated by those σ at the energy density ϵ which maximizes $s(\epsilon) - \beta\epsilon$, where $s(\epsilon)$ is the disorder-averaged entropy density (the sample-to-sample fluctuations about $s(\epsilon)$ are expected to vanish as $N \to \infty$). The configurations at other energy densities collectively give an exponentially small contribution. Thus as $N \to \infty$,

$$\mathbb{E}\left[\mathrm{Tr}_\sigma\left[\frac{e^{-N\beta\epsilon(\sigma)}}{Z(\beta)} f(\sigma)\right]\right] \sim \mathbb{E}\left[\mathrm{Tr}_\sigma\left[\frac{\delta\big(\epsilon - \epsilon(\sigma)\big)}{\mathcal{N}(\epsilon)} f(\sigma)\right]\right], \tag{3.16}$$

where $\epsilon = \mathrm{argmax}_z\big[s(z) - \beta z\big]$ and $\mathcal{N}(\epsilon) = e^{Ns(\epsilon)}$.

Eq. (3.16) applies to $v(x, \beta'|\beta)$ with

$$f(\sigma) = \ln \mathrm{Tr}_{\sigma'}\big[\delta_{x,x(\sigma,\sigma')} e^{-N\beta'\epsilon(\sigma')}\big]. \tag{3.17}$$

In fact, since all configurations are statistically equivalent, the argument of the trace over σ in Eq. (3.14) is independent of σ and we have that

$$v(x, \beta'|\beta) = \mathbb{E}\Big[\ln \mathrm{Tr}_{\sigma'}\big[\delta_{x,x(\sigma,\sigma')} e^{-N\beta'\epsilon(\sigma')}\big]\Big]\Big|_{\epsilon(\sigma)=\epsilon}, \tag{3.18}$$

for an arbitrary reference configuration σ.

Next write

$$\mathrm{Tr}_{\sigma'}\big[\delta_{x,x(\sigma,\sigma')} e^{-N\beta'\epsilon(\sigma')}\big] = \int \mathrm{d}\epsilon' e^{-N\beta'\epsilon'} \mathrm{Tr}_{\sigma'}\big[\delta_{x,x(\sigma,\sigma')} \delta\big(\epsilon' - \epsilon(\sigma')\big)\big]. \tag{3.19}$$

The trace on the right-hand side is precisely $e^{Ng(x,\epsilon'|\epsilon)}$. The integral is then dominated by $\epsilon' = \mathrm{argmax}_{z'}\big[g(x, z'|\epsilon) - \beta' z'\big]$. We thus have the desired relationship between the FPP $v(x, \beta'|\beta)$ and the distance-resolved entropy $g(x, \epsilon'|\epsilon)$:

$$v(x, \beta'|\beta) = g(x, \epsilon'|\epsilon) - \beta'\epsilon', \tag{3.20}$$

$$\epsilon = \text{argmax}_z \big[s(z) - \beta z \big], \tag{3.21}$$

$$\epsilon' = \text{argmax}_{z'} \big[g(x, z'|\epsilon) - \beta' z' \big]. \tag{3.22}$$

Note that the relationship between ϵ' and β' is not set by the full entropy $s(\epsilon)$ but rather by the distance-resolved entropy $g(x, \epsilon'|\epsilon)$.

Eqs. (3.20), (3.21), and (3.22) express $v(x, \beta'|\beta)$ in terms of $g(x, \epsilon'|\epsilon)$ through a Legendre transform. By inverting the transform, one obtains $g(x, \epsilon'|\epsilon)$ in terms of $v(x, \beta'|\beta)$.

For our purposes, $g(x, \epsilon'|\epsilon)$ is a much more natural object to use than $v(x, \beta'|\beta)$. Nevertheless, this analysis establishes that our results will have close connections to the existing spin glass literature. Given the relationship, we will often refer to $g(x, \epsilon'|\epsilon)$ as the microcanonical FPP or simply the FPP.

3.3.2 Annealed averaging

Strictly speaking, one would need to use the replica trick to evaluate the FPP, as done in [101]. However, the essential physics remains intact if we instead take an "annealed" average by switching the order of the logarithm and disorder average:

$$g(x, \epsilon'|\epsilon) \approx \frac{1}{N} \ln \mathbb{E}\Big[\text{Tr}_{\sigma'} \big[\delta_{x, x(\sigma,\sigma')} \, \delta\big(\epsilon' - \epsilon(\sigma')\big) \big] \Big]_{\epsilon(\sigma)=\epsilon} = \frac{1}{N} \ln \mathbb{E}\big[\mathcal{N}(x, \epsilon'|\epsilon) \big]. \tag{3.23}$$

Thus despite the points made above, we disorder-average $\mathcal{N}(x, \epsilon'|\epsilon)$ in the end. Markov's inequality from Sec. 3.2 provides the justification. The most important feature of our analysis shall be identifying intermediate distances x at which there are no low-energy configurations. Thus we can map out the shapes of the energy barriers that separate clusters. We shall find that the annealed $g(x, \epsilon'|\epsilon)$ in Eq. (3.23) can become negative for intermediate x and low ϵ', meaning that $\mathbb{E}[\mathcal{N}(x, \epsilon'|\epsilon)]$ is exponentially small, from which Markov's inequality gives that there are no states at such x having ϵ' with high probability. This is the conclusion which we were aiming for.

Furthermore, the inequality $\mathbb{E}[\ln \cdot\,] \leq \ln \mathbb{E}[\,\cdot\,]$ shows that the annealed estimate for the FPP is a rigorous upper bound to the true value.

Evaluating $\mathbb{E}[\mathcal{N}(x, \epsilon'|\epsilon)]$ is reasonably straightforward. We first need the joint distribution for configurations σ and σ', separated by distance x, to have energy densities ϵ and ϵ'. We know that ϵ and ϵ' are Gaussian-distributed, and Eq. (3.1) gives the covariance matrix, thus up to normalization,

$$P_2(\epsilon, \epsilon') \propto e^{-N \boldsymbol{\epsilon}^T Q^{-1} \boldsymbol{\epsilon}}, \tag{3.24}$$

where $\boldsymbol{\epsilon}^T \equiv \begin{pmatrix} \epsilon & \epsilon' \end{pmatrix}$ and

$$Q \equiv \begin{pmatrix} 1 & (1-2x)^p \\ (1-2x)^p & 1 \end{pmatrix}. \tag{3.25}$$

Evaluating the inverse,

$$P_2(\epsilon,\epsilon') \propto \exp\left(-N\frac{\epsilon^2 - 2(1-2x)^p\epsilon\epsilon' + \epsilon'^2}{1-(1-2x)^{2p}}\right). \tag{3.26}$$

In particular, the conditional distribution of ϵ' given ϵ is

$$P_{1|2}(\epsilon'|\epsilon) \propto \exp\left(-N\frac{(\epsilon' - (1-2x)^p\epsilon)^2}{1-(1-2x)^{2p}}\right), \tag{3.27}$$

again up to normalization. $\mathbb{E}[\mathcal{N}(x,\epsilon'|\epsilon)]$ is then simply

$$\mathbb{E}[\mathcal{N}(x,\epsilon'|\epsilon)] = \binom{N}{Nx} P_{1|2}(\epsilon'|\epsilon), \tag{3.28}$$

and the annealed estimate for the FPP is

$$g(x,\epsilon'|\epsilon) = -x\ln x - (1-x)\ln(1-x) - \frac{\left(\epsilon' - (1-2x)^p\epsilon\right)^2}{1-(1-2x)^{2p}}. \tag{3.29}$$

Note that if we take $p \to \infty$, $(1-2x)^p \to 0$ and we recover Eq. (2.65), the REM expression for $g(x,\epsilon'|\epsilon)$. The finite-p expression for the FPP is more complicated, and in particular now depends on ϵ, because of the correlations in the p-spin model.

One might hope that the variance in $\mathcal{N}(x,\epsilon'|\epsilon)$ is small compared to the mean, analogous to the situation in the REM, for then Eq. (3.29) would be exact rather than approximate. Unfortunately, this is not the case. Using Eq. (3.12),

$$\mathbb{E}\big[\mathcal{N}(x,\epsilon'|\epsilon)^2\big] = \sum_{\sigma'\sigma''} \delta_{x,x(\sigma,\sigma')}\delta_{x,x(\sigma,\sigma'')}P_{2|3}(\epsilon',\epsilon'|\epsilon), \tag{3.30}$$

where $P_{2|3}(\epsilon',\epsilon'|\epsilon)$ is the conditional distribution for $\epsilon(\sigma') = \epsilon'$ and $\epsilon(\sigma'') = \epsilon'$ given $\epsilon(\sigma) = \epsilon$. The distribution depends on σ' and σ'' only through x and y, the distance between them. Thus

$$\mathbb{E}\big[\mathcal{N}(x,\epsilon'|\epsilon)^2\big] \sim \binom{N}{Nx}\int \mathrm{d}y \binom{Nx}{N\frac{y}{2}}\binom{N(1-x)}{N\frac{y}{2}} P_{2|3}(\epsilon',\epsilon'|\epsilon). \tag{3.31}$$

Dividing by the square of the mean, we have

$$\frac{\mathbb{E}\big[\mathcal{N}(x,\epsilon'|\epsilon)^2\big]}{\mathbb{E}\big[\mathcal{N}(x,\epsilon'|\epsilon)\big]^2} = \int \mathrm{d}y\, \frac{\binom{Nx}{N\frac{y}{2}}\binom{N(1-x)}{N\frac{y}{2}}}{\binom{N}{Nx}}\, \frac{P_{2|3}(\epsilon',\epsilon'|\epsilon)}{P_{1|2}(\epsilon'|\epsilon)^2}. \tag{3.32}$$

The joint distribution for three energy levels is given by an expression analogous to Eqs. (3.24) and (3.25):

$$P_3(\epsilon,\epsilon',\epsilon') \propto e^{-N\boldsymbol{\epsilon}^T Q^{-1}\boldsymbol{\epsilon}}, \tag{3.33}$$

where $\boldsymbol{\epsilon}^T \equiv \begin{pmatrix}\epsilon & \epsilon' & \epsilon'\end{pmatrix}$ and

$$Q \equiv \begin{pmatrix} 1 & (1-2x)^p & (1-2x)^p \\ (1-2x)^p & 1 & (1-2y)^p \\ (1-2x)^p & (1-2y)^p & 1 \end{pmatrix}. \tag{3.34}$$

A straightforward but tedious calculation of the inverse gives

$$\boldsymbol{\epsilon}^T Q^{-1} \boldsymbol{\epsilon} = \frac{2}{1-2\mu(x)^2+\mu(y)} \left(\epsilon'^2 - 2\mu(x)\epsilon\epsilon' + \frac{1+\mu(y)}{2}\epsilon^2 \right), \tag{3.35}$$

where $\mu(z) \equiv (1-2z)^p$. Then the conditional distribution is

$$P_{2|3}(\epsilon', \epsilon'|\epsilon) \propto \exp\left(-N \frac{2\big(\epsilon' - \mu(x)\epsilon\big)^2}{1-2\mu(x)^2+\mu(y)} \right). \tag{3.36}$$

Dividing by $P_{1|2}(\epsilon'|\epsilon)^2$ gives

$$\frac{P_{2|3}(\epsilon', \epsilon'|\epsilon)}{P_{1|2}(\epsilon'|\epsilon)^2} \sim \exp\left(-N \frac{2\big(\mu(x)^2 - \mu(y)\big)}{\big(1-\mu(x)^2\big)\big(1-2\mu(x)^2+\mu(y)\big)} \big(\epsilon' - \mu(x)\epsilon\big)^2 \right). \tag{3.37}$$

As for the binomial coefficients,

$$\begin{aligned} &\frac{1}{N} \ln \binom{Nx}{N\frac{y}{2}} \binom{N(1-x)}{N\frac{y}{2}} \\ &\quad \sim \frac{y}{2} \ln \frac{4x(1-x)}{y^2} + \left(x - \frac{y}{2}\right) \ln \frac{2x}{2x-y} + \left(1 - x - \frac{y}{2}\right) \ln \frac{2(1-x)}{2(1-x)-y}. \end{aligned} \tag{3.38}$$

The maximum is at

$$\frac{(2x-y^*)(2-2x-y^*)}{y^{*2}} = 1, \tag{3.39}$$

i.e. $y^* = 2x(1-x)$. Then Eq. (3.38) gives

$$\binom{Nx}{N\frac{y^*}{2}} \binom{N(1-x)}{N\frac{y^*}{2}} \sim \binom{N}{Nx}, \tag{3.40}$$

and the binomial coefficients in Eq. (3.32) together give 1 at y^*.

Note that $\mu(y^*) = \mu(x)^2$, and thus that the exponent of Eq. (3.37) vanishes there. Thus the integral in Eq. (3.32) has a contribution scaling as $O(1)$ from y^*. This makes sense: we know automatically that $\mathbb{E}\big[\mathcal{N}(x, \epsilon'|\epsilon)^2\big] / \mathbb{E}\big[\mathcal{N}(x, \epsilon'|\epsilon)\big]^2$ must be at least 1. The question now is whether y^* is the saddle-point of Eq. (3.32). If so, we would have that $\mathbb{E}\big[\mathcal{N}(x, \epsilon'|\epsilon)^2\big] / \mathbb{E}\big[\mathcal{N}(x, \epsilon'|\epsilon)\big]^2 \sim 1$ and thus $\mathrm{Var}\big[\mathcal{N}(x, \epsilon'|\epsilon)\big] / \mathbb{E}\big[\mathcal{N}(x, \epsilon'|\epsilon)\big]^2 \to 0$ as $N \to \infty$. Unfortunately, y^* is not the saddle-point. One can check that the exponent of Eq. (3.37) has a negative first derivative at y^*, meaning that the saddle-point must be at $y < y^*$ and that the value at the saddle-point is greater than at y^*, i.e., positive. We have shown

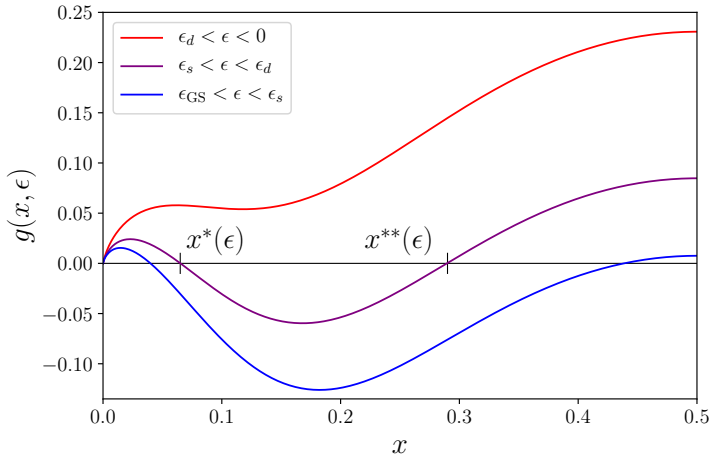

Figure 3.3: Transitions in the p-spin model exhibited through the FPP, $g(x, \epsilon|\epsilon)$. Only $x < 1/2$ is shown, since (for even p) $g(x, \epsilon|\epsilon)$ is symmetric between $x \leftrightarrow 1 - x$. For the curves shown, we made the annealed approximation using $p = 6$ and $\epsilon = -0.68$ (red), -0.78 (purple), -0.828 (blue).

that $\mathbb{E}\big[\mathcal{N}(x, \epsilon'|\epsilon)^2\big]$ is exponentially larger than $\mathbb{E}\big[\mathcal{N}(x, \epsilon'|\epsilon)\big]^2$, and we cannot use Chebyshev's inequality to show that the fluctuations in $\mathcal{N}(x, \epsilon'|\epsilon)$ are small.

Thus as far as we know, $g(x, \epsilon'|\epsilon)$ in Eq. (3.29) is only approximate. We shall continue to use it in our calculations for concreteness, but it is important to keep this fact in mind.

3.3.3 Geometry of the energy landscape

Fig. 3.3 plots $g(x, \epsilon|\epsilon) \equiv g(x, \epsilon)$ as a function x. For reference,

$$g(x, \epsilon) = -x \ln x - (1 - x) \ln (1 - x) - \frac{1 - (1 - 2x)^p}{1 + (1 - 2x)^p} \epsilon^2. \tag{3.41}$$

The curves demonstrate that low-lying energy levels are organized into clusters, and give a quantitative picture of the transitions sketched in Fig. 3.2.

- $\epsilon_d < \epsilon < 0$: $g(x, \epsilon) > 0$ for all x. There are configurations that have the same energy density at all distances from the reference state σ. This suggests that each configuration is connected to all others, forming a single cluster that spans the configuration space. While it is not a proof, as the FPP distinguishes only the radial coordinate x of configurations and not angular coordinates, dynamical calculations of the classical stochastic dynamics confirm that $q_{\rm EA} = 0$ above ϵ_d [79, 103].

- $\epsilon_s < \epsilon < \epsilon_d$: $g(x, \epsilon)$ is positive for x less than a certain $x^*(\epsilon)$ or greater than a certain $x^{**}(\epsilon)$ (see Fig. 3.3), but is negative in between. This

shows that configurations below ϵ_d are organized into disjoint clusters. No configurations at distances $x \in \big(x^*(\epsilon), x^{**}(\epsilon)\big)$ have energy density ϵ, thus those at $x > x^{**}(\epsilon)$ cannot be connected to σ. Furthermore, the maximum of $g(x,\epsilon)$ over $x > x^{**}(\epsilon)$ is greater than that over $x < x^*(\epsilon)$. In other words, although the number of configurations within a cluster is still exponential, there are exponentially more configurations disconnected to σ than connected, i.e., exponentially many clusters. A randomly selected σ' lies at distance $1/2$ from σ.

- $\epsilon_{\rm GS} < \epsilon < \epsilon_s$: The maximum of $g(x,\epsilon)$ over $x > x^{**}(\epsilon)$ is now *less* than that over $x < x^*(\epsilon)$. Interpreting this result literally, one would say that most configurations belong to a single cluster of linear size $x^*(\epsilon)$. A randomly selected σ' lies within that distance.

We are specifically interested in large but finite p, where all the relevant quantities can be computed analytically to leading order in $1/p$. First consider the linear cluster size $x^*(\epsilon)$ at $\epsilon \sim O(1)$ (with respect to p). For $x \ll \frac{1}{p}$,

$$\begin{aligned} g(x,\epsilon) &\sim -x\ln x + x - xp\epsilon^2 + O(p^2x^2) \\ &\sim x\left(\ln\frac{e}{x} - p\epsilon^2\right). \end{aligned} \tag{3.42}$$

The right-hand side starts at 0 for $x = 0$, is positive for sufficiently small x, and then becomes negative. Thus

$$x^*(\epsilon) \sim e^{1-p\epsilon^2}. \tag{3.43}$$

As for the separation between clusters $x^{**}(\epsilon)$, it occurs at $x \sim O(1)$, for which

$$g(x,\epsilon) \sim -x\ln x - (1-x)\ln(1-x) - \epsilon^2 + e^{-O(p)}. \tag{3.44}$$

Thus

$$x^{**}(\epsilon) = x^{**}(\epsilon)_{p\to\infty} - e^{-O(p)}, \tag{3.45}$$

where $x^{**}(\epsilon)_{p\to\infty}$ is the REM value of $x^{**}(\epsilon)$. We have shown that the clusters have a linear size exponentially small in p and are separated by $O(1)$ fractional Hamming distances.

We next use the FPP to characterize the energy barriers between clusters. Setting $g(x,\epsilon'|\epsilon) = 0$ at *fixed* x gives us a bound $\epsilon'_-(x)$: all configurations at distance x have energy densities greater than $\epsilon'_-(x)$. For x between $x^*(\epsilon)$ and $x^{**}(\epsilon)$,

$$\epsilon'_-(x) = (1-2x)^p\epsilon - \sqrt{\big(1-(1-2x)^{2p}\big)\big(-x\ln x - (1-x)\ln(1-x)\big)}, \tag{3.46}$$

which is strictly greater than ϵ. The shape of $\epsilon'_-(x)$ is plotted in Fig. 3.4. At large p, the peak of the barrier is at

$$x_{\rm peak} \sim \frac{\ln p}{4p}, \tag{3.47}$$

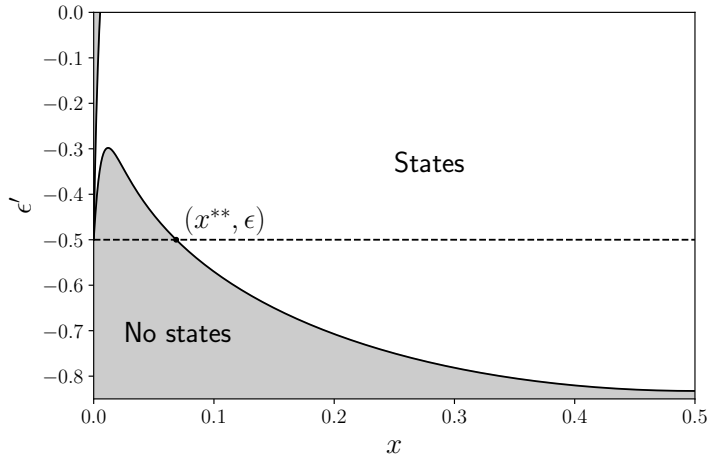

Figure 3.4: Regions of the (x, ϵ') plane in which the FPP is positive (white) and negative (grey), for $p = 100$ and $\epsilon = -0.5$ (dashed line). Configurations at distance x have energy densities exclusively in the white region. $x^{**}(\epsilon)$ is marked, and $x^{*}(\epsilon)$ is too close to 0 to be visible on this scale. The curve separating white and grey is $\epsilon'_{-}(x)$, Eq. (3.46) (the corresponding upper root $\epsilon'_{+}(x)$ is barely visible in the top-left corner).

with a height of

$$\epsilon'_{-}(x_{\text{peak}}) - \epsilon \sim |\epsilon| - \frac{\ln p}{2\sqrt{p}}. \tag{3.48}$$

Now consider the dynamical transition at ϵ_d. We can show that it occurs on a scale $\sqrt{\frac{\ln p}{p}}$, i.e., $\epsilon_d = \epsilon_r \sqrt{\frac{\ln p}{p}}$. The FPP on this scale is

$$g(x, \epsilon) = -x \ln x - (1-x) \ln (1-x) - \frac{1-(1-2x)^p}{1+(1-2x)^p} \frac{\ln p}{p} \epsilon_r^2. \tag{3.49}$$

Define $x \equiv \frac{x_r}{p}$ with $x_r \lesssim O(\ln^n p)$, then

$$g(x, \epsilon) \sim \frac{\ln p}{p} \left(x_r - \epsilon_r^2 \frac{1-e^{-2x_r}}{1+e^{-2x_r}} \right) + \frac{1}{p} x_r \ln \frac{e}{x_r} + O\left(\frac{\ln^n p}{p^2} \right). \tag{3.50}$$

If $\epsilon_r > 1$, then $g(x, \epsilon) < 0$ for an interval of $x_r \sim O(1)$. On the other hand, if $\epsilon_r < 1$, then $g(x, \epsilon) > 0$ for all x_r: the first term is always positive, while the second term is positive for $x_r \ll 1$ and subleading for $x_r \sim O(1)$. Finally, if $x \gg \frac{\ln^n p}{p}$, the last term in Eq. (3.49) is subleading compared to the first two and $g(x, \epsilon)$ is manifestly positive. Together, this identifies $\epsilon_r = 1$ as the location of the dynamical transition, i.e.,

$$\epsilon_d \sim \sqrt{\frac{\ln p}{p}}. \tag{3.51}$$

As for the static transition at ϵ_s, from Eq. (3.42) we see that

$$\max_{x<x^*(\epsilon)} g(x,\epsilon) = e^{-p\epsilon^2}, \tag{3.52}$$

whereas

$$\max_{x>x^{**}(\epsilon)} g(x,\epsilon) = \ln 2 - \epsilon^2. \tag{3.53}$$

Thus we have that

$$\epsilon_s \sim -\sqrt{\ln 2} + \frac{1}{2\sqrt{\ln 2}}\, 2^{-p}. \tag{3.54}$$

Note that Eq. (3.52) is the entropy density of configurations within an individual cluster (this follows from integrating $e^{Ng(x,\epsilon)}$ over $x < x^*(\epsilon)$, which to exponential order simply gives the maximum value). Although it may appear to be small, keep in mind that it is the entropy per spin. The *number* of configurations within the cluster is exponentially large, e^{Ng}, regardless of whether g is exponentially small in p. Since the internal entropy of each cluster is strictly less than the thermodynamic entropy $s(\epsilon) = \ln 2 - \epsilon^2$, the number of clusters is itself exponential. The entropy density of clusters, often called the "complexity", makes up the difference between the internal and thermodynamic entropies. At the risk of belaboring the point, this is the most important feature of the clustered phase at $\epsilon \in (\epsilon_s, \epsilon_d)$. The energy landscape is disconnected into exponentially many clusters, each with exponentially many configurations inside.

It is worth noting again that since we estimated $g(x,\epsilon)$ through an annealed average, the quantities calculated here are only approximate. In particular, the interpretation that below ϵ_s most states belong to a single cluster is too naive: the number of clusters is $O(1)$ but larger than 1, and it depends on ϵ [63]. However, the fact that the annealed $g(x,\epsilon)$ is an upper bound to the typical value tells us the direction in which our results are approximate. Eq. (3.43) is an upper bound on $x^*(\epsilon)$ and Eq. (3.45) is a lower bound on $x^{**}(\epsilon)$, while Eqs. (3.46) and (3.51) for the energy barrier and value of ϵ_d are both lower bounds.

3.4 A proof of clustering

Even though the annealed FPP is only approximate, we can nonetheless *prove* that the low-energy states in the p-spin model are organized into clusters by using a different approach, analogous to what was done in Ref. [72] for satisfiability problems. Rather than fixing a configuration σ and counting states at distance x around it, we count the total number of pairs σ & σ' which are separated by distance x. For simplicity, we take both states to have energy density ϵ. Denote the number by $\mathcal{N}_{\rm pair}(x,\epsilon)$, then formally,

$$\mathcal{N}_{\rm pair}(x,\epsilon) = \sum_{\sigma\sigma'} \delta_{x,x(\sigma,\sigma')} \delta\big(\epsilon - \epsilon(\sigma)\big)\delta\big(\epsilon - \epsilon(\sigma')\big). \tag{3.55}$$

The first moment is easy to compute:

$$\begin{aligned}\mathbb{E}\big[\mathcal{N}_{\text{pair}}(x,\epsilon)\big] &= 2^N \binom{N}{Nx} P_2(\epsilon,\epsilon) \\ &= e^{N\left(\ln 2 - \epsilon^2 + g(x,\epsilon)\right)}.\end{aligned} \tag{3.56}$$

Note that

$$\mathbb{E}\big[\mathcal{N}_{\text{pair}}(x,\epsilon)\big] = \begin{cases} e^{N(\ln 2 - \epsilon^2)} & , \quad x = 0 \\ e^{2N(\ln 2 - \epsilon^2)} & , \quad x = \frac{1}{2} \end{cases}. \tag{3.57}$$

We are only interested in $|\epsilon| < \sqrt{\ln 2}$ since we know that the spectrum is contained in this interval. Thus $\mathbb{E}\big[\mathcal{N}_{\text{pair}}(x,\epsilon)\big] \gg 1$ for x close to 0 and x close to $1/2$. Intermediate x are more interesting. For sufficiently low ϵ (e.g., $\epsilon < -\sqrt{\frac{\ln 2}{2}}$ at large p), one can show that there is a range of distances in which $\mathbb{E}\big[\mathcal{N}_{\text{pair}}(x,\epsilon)\big]$ is exponentially small. Thus there are no pairs separated by intermediate distances, with certainty in the thermodynamic limit. If we can show that $\mathcal{N}_{\text{pair}}(x,\epsilon)$ concentrates around its mean at smaller and larger distances, then we will have proved that the states at low ϵ form disjoint clusters.

From Eq. (3.55), we see that $\mathcal{N}_{\text{pair}}(x,\epsilon)^2$ involves a sum over sets of four configurations. The orientation between any four is specified by the distances x_{mn}, $1 \le m < n \le 4$, with x_{12} and x_{34} fixed at x. We can write

$$\mathbb{E}\big[\mathcal{N}_{\text{pair}}(x,\epsilon)^2\big] = \sum_{x_{mn}} \mathcal{N}_4\big(\{x_{mn}\}\big) P_4(\epsilon,\epsilon,\epsilon,\epsilon), \tag{3.58}$$

with P_4 the joint distribution of energies and $\mathcal{N}_4$ the number of sets of configurations consistent with the given distances. Our strategy is to show that $\mathcal{N}_4 P_4$ has a saddle-point at $x^*_{13} = x^*_{14} = x^*_{23} = x^*_{24} = 1/2$, that at this saddle-point $\mathcal{N}_4 P_4 \sim \mathbb{E}\big[\mathcal{N}_{\text{pair}}(x,\epsilon)\big]^2 \equiv (\mathcal{N}_2 P_2)^2$, and that any other saddle-points give exponentially smaller contributions. It follows that $\mathbb{E}\big[\mathcal{N}_{\text{pair}}(x,\epsilon)^2\big] \sim \mathbb{E}\big[\mathcal{N}_{\text{pair}}(x,\epsilon)\big]^2$ and then, by Chebyshev's inequality, that $\mathcal{N}_{\text{pair}}(x,\epsilon)$ concentrates around its mean.

We first focus on $\mathcal{N}_4$. Note that

$$\mathcal{N}_4\big(\{x_{mn}\}\big) = \text{Tr}\left[\prod_{m<n} \delta\left(\frac{1}{N}\sum_i \frac{1+\sigma_i^{(m)}\sigma_i^{(n)}}{2} - x_{mn}\right)\right], \tag{3.59}$$

where the trace is over four systems of N Ising spins each. Certainly $\mathcal{N}_4$ scales exponentially with N, and thus we have that

$$\max_{x_{mn}} \big[\mathcal{N}_4\big(\{x_{mn}\}\big)\big] \sim \int \mathcal{D}x\, \mathcal{N}_4\big(\{x_{mn}\}\big). \tag{3.60}$$

Intuitively, one expects the maximum to be at $x^*_{13} = x^*_{14} = x^*_{23} = x^*_{24} = 1/2$, and we can show this formally. Using the identity

$$\delta\big(f(\sigma) - x_{mn}\big) = \int_{-i\infty}^{i\infty} \mathrm{d}\lambda_{mn}\, e^{N\lambda_{mn}\left(f(\sigma) - x_{mn}\right)}, \tag{3.61}$$

we have

$$\begin{aligned}\mathcal{N}_4\big(\{x_{mn}\}\big) &= \int \mathcal{D}\lambda\, e^{-N\sum_{m<n}\lambda_{mn}x_{mn}}\mathrm{Tr}\left[e^{\sum_{m<n}\lambda_{mn}\sum_i \frac{1+\sigma_i^{(m)}\sigma_i^{(n)}}{2}}\right] \\ &= \int \mathcal{D}\lambda\, e^{N\left(-\sum_{m<n}\lambda_{mn}x_{mn}+\ln Z_{\text{eff}}\right)},\end{aligned} \tag{3.62}$$

where

$$Z_{\text{eff}} = \sum_{\sigma^{(m)}} e^{\sum_{m<n}\lambda_{mn}\frac{1+\sigma^{(m)}\sigma^{(n)}}{2}}. \tag{3.63}$$

Given Eq. (3.60), we can compute the maximum value of $\mathcal{N}_4$ by integrating over x_{mn} (but not x_{12} or x_{34}, which are fixed at x). Yet from Eq. (3.62), integration over x_{mn} simply fixes $\lambda_{mn} = 0$. Then

$$\begin{aligned}Z_{\text{eff}} &= \left(\sum_{\sigma^{(1)}\sigma^{(2)}} e^{\lambda_{12}\frac{1+\sigma^{(1)}\sigma^{(2)}}{2}}\right)\left(\sum_{\sigma^{(3)}\sigma^{(4)}} e^{\lambda_{34}\frac{1+\sigma^{(3)}\sigma^{(4)}}{2}}\right) \\ &= 4\left(1+e^{\lambda_{12}}\right)\left(1+e^{\lambda_{34}}\right).\end{aligned} \tag{3.64}$$

We integrate over λ_{12} and λ_{34} by saddle-point, which sets $\lambda_{12} = \lambda_{34} = \ln\frac{x}{1-x}$, giving us

$$\begin{aligned}\max_{x_{mn}}\left[\mathcal{N}_4\big(\{x_{mn}\}\big)\right] &\sim e^{2N\left(\ln 2 - x\ln x - (1-x)\ln(1-x)\right)} \\ &\sim \left(2^N\binom{N}{Nx}\right)^2.\end{aligned} \tag{3.65}$$

For the location of the maximum, note that if we had not integrated over x_{mn}, the saddle-point equation for λ_{mn} would be

$$x_{mn} = \frac{1}{2} + \frac{1}{Z_{\text{eff}}}\sum_{\sigma^{(m)}} \frac{\sigma^{(m)}\sigma^{(n)}}{2} e^{\sum_{m<n}\lambda_{mn}\frac{1+\sigma^{(m)}\sigma^{(n)}}{2}}, \tag{3.66}$$

which defines $\lambda^*_{mn}(x_{mn})$ implicitly. Since integrating over x_{mn} is equivalent to evaluating the integrand at the saddle-point x^*_{mn}, and integrating over x_{mn} fixes λ_{mn} to be 0, we have that $\lambda^*_{mn}(x^*_{mn}) = 0$. Plugging into Eq. (3.66), we get that $x^*_{mn} = 1/2$.

We now turn to P_4. The joint distribution is

$$P_4(\epsilon,\epsilon,\epsilon,\epsilon) = e^{-N\boldsymbol{\epsilon}^T Q^{-1}\boldsymbol{\epsilon}}, \tag{3.67}$$

where $\boldsymbol{\epsilon}^T \equiv \begin{pmatrix}\epsilon & \epsilon & \epsilon & \epsilon\end{pmatrix}$ and

$$Q \equiv \begin{pmatrix} 1 & (1-2x)^p & (1-2x_{13})^p & (1-2x_{14})^p \\ (1-2x)^p & 1 & (1-2x_{23})^p & (1-2x_{24})^p \\ (1-2x_{13})^p & (1-2x_{23})^p & 1 & (1-2x)^p \\ (1-2x_{14})^p & (1-2x_{24})^p & (1-2x)^p & 1 \end{pmatrix}. \tag{3.68}$$

It would be too tedious to evaluate Q^{-1} directly. However, note that Q becomes block-diagonal when we set x_{mn} to $x^*_{mn} = 1/2$. Then

$$\boldsymbol{\epsilon}^T Q^{-1} \boldsymbol{\epsilon} = 2 \begin{pmatrix} \epsilon & \epsilon \end{pmatrix} \begin{pmatrix} 1 & (1-2x)^p \\ (1-2x)^p & 1 \end{pmatrix} \begin{pmatrix} \epsilon \\ \epsilon \end{pmatrix}, \tag{3.69}$$

and $P_4(\epsilon, \epsilon, \epsilon, \epsilon) \sim P_2(\epsilon, \epsilon)^2$. As for the correction when we shift x_{mn} slightly away from $1/2$, write $x_{mn} = \frac{1+\Delta_{mn}}{2}$. Then Q depends on Δ^p_{mn}, and since Q^{-1} is an analytic function of Δ_{mn}, we see that the correction to Q^{-1} is $O(\Delta^p_{mn})$.

It follows that $x^*_{mn} = 1/2$ is a maximum of $\mathcal{N}_4 P_4$: it is a maximum of $\mathcal{N}_4$, and the exponent of P_4 has vanishing first *and second* derivatives at that location (for $p > 2$). We have also shown that

$$\mathcal{N}_4\big(\{x^*_{mn}\}\big) P_4(\epsilon, \epsilon, \epsilon, \epsilon) \sim \Big(\mathcal{N}_2\big(x\big) P_2(\epsilon, \epsilon)\Big)^2. \tag{3.70}$$

Thus x^*_{mn} is the saddle-point which we hoped to find.

Assuming p is large, similar analysis shows that any other saddle-points must be sub-leading. Since the correction to Q^{-1} for x_{mn} around $1/2$ scales as $O(\Delta^p_{mn})$, in the large-p limit the only cases to consider are those in which some or all $x_{mn} \lesssim O(1/p)$. If $x_{13} \to 0$ and $x_{24} \not\to 0$, one finds that $\mathcal{N}_4 P_4 \to e^{-N(\ln 2 - \epsilon^2)} (\mathcal{N}_2 P_2)^2 \ll (\mathcal{N}_2 P_2)^2$. If $x_{13} \to 0$ and $x_{24} \to 0$, one finds that $\mathcal{N}_4 P_4 \to \mathcal{N}_2 P_2 \ll (\mathcal{N}_2 P_2)^2$.

We have shown that $\mathbb{E}\big[\mathcal{N}_{\text{pair}}(x, \epsilon)^2\big] \sim \mathbb{E}\big[\mathcal{N}_{\text{pair}}(x, \epsilon)\big]^2$ in the event that $\mathbb{E}\big[\mathcal{N}_{\text{pair}}(x, \epsilon)\big]$ is large. Chebyshev's inequality then proves that fluctuations in $\mathcal{N}_{\text{pair}}(x, \epsilon)$ around the mean are unlikely. Since $\mathcal{N}_{\text{pair}}(x, \epsilon)$ is exponentially large for both small x and large x, but is 0 in between when ϵ is sufficiently small, this proves that the low-energy states in the p-spin model are organized into disjoint clusters.

Chapter 4

Quantum dynamics in the p-spin model

Here we study the dynamical behavior of the quantum p-spin model:

$$H = H_p - \Gamma \sum_i \hat{\sigma}_i^x, \tag{1.38}$$

with H_p as described in detail in Chap. 3. Our goal is the same as in Chap. 2 for the REM: to elucidate the eigenstate and dynamical phases, now in a more realistic energy landscape. Many of the conclusions drawn there apply here as well, merely by replacing the individual configurations in the REM with clusters in the p-spin model. Although each cluster now contains exponentially many configurations, there are many such clusters scattered throughout the configuration space. The exponentially small tunneling amplitudes between them compete non-trivially with the exponentially large number of them.

Now that there are multiple configurations inside each cluster, we must tweak our definition of matching problems. Given a state $|\sigma\rangle$ in a cluster of the p-spin model, if the goal were to find any other $|\sigma'\rangle$ having the same energy, the problem would be trivial: simply find another state in the same cluster, where there are no energy barriers to impede progress. Thus we additionally require that $|\sigma'\rangle$ lie in a different cluster from $|\sigma\rangle$. This was always the implicit aim in matching. The utility of having multiple solutions to an optimization problem comes from those solutions being sufficiently distinct, rather than superficial modifications of the same structure.

The presence of exponentially many configurations per cluster also makes clear the distinction between the trapped eigenstates in the p-spin model and many-body localization. We argue in Sec. 4.3 that the trapped eigenstates are nonetheless "thermal" within their respective clusters, in a sense which we make precise. This has no analogue in MBL, and makes the trapped phase a genuinely novel class of eigenstates.

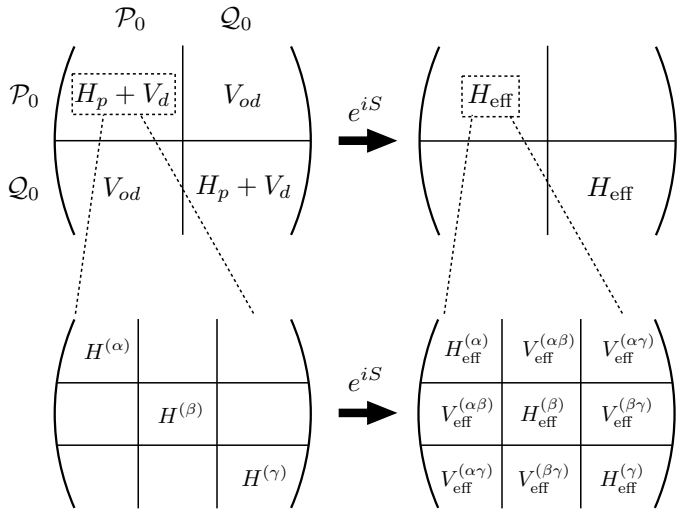

Figure 4.1: The Schrieffer-Wolff transformation. The left side is H, the right side H_{eff}. On top is the full Hamiltonian, broken into $\mathcal{P}_0$ and $\mathcal{Q}_0$ subspaces. V has a block-diagonal part V_d and an off-block-diagonal part V_{od}. Below is a schematic of the structure within $\mathcal{P}_0$. Superscripts refer to different clusters.

4.1 Finite-p corrections

As we did for the REM, we study the quantum p-spin model using the distance-resolved density of states $\mathcal{N}(x, \epsilon'|\epsilon) \sim e^{Ng(x,\epsilon'|\epsilon)}$ and the effective coupling $V_{\text{eff}}(x, \epsilon'|\epsilon) \sim e^{-N\gamma(x,\epsilon'|\epsilon)}$. The density of states was discussed in Sec. 3.3. We take the effective coupling to again be the matrix element between $|\sigma\rangle$ and $|\sigma'\rangle$ in the Schrieffer-Wolff-transformed Hamiltonian, computed within the FSA.

The Schrieffer-Wolff transformation itself comes with some subtleties in the p-spin model. As before, we define it so as to decouple the $\hat{\sigma}^z$ states having classical energy density ϵ (the $\mathcal{P}_0$ subspace) from those having a different classical energy density (the $\mathcal{Q}_0$ subspace). Yet now the effective Hamiltonian contains an intra-cluster part as well as the inter-cluster terms. The situation is illustrated in Fig. 4.1. We will neglect the energy shifts that arise from the intra-cluster effective Hamiltonian ($H_{\text{eff}}^{(\alpha)}$ in Fig. 4.1). Our justification relies on the fact that the entropy of states within each cluster is exponentially small in p. Assuming that the corrections which come from diagonalizing $H_{\text{eff}}^{(\alpha)}$ scale as that entropy[1], they will be sub-leading compared to the polynomial-in-$1/p$

[1]For example, a very crude model for a cluster with e^{Ng} states would be that $Ng/\ln 2$ spins are free to flip while the remaining $N - Ng/\ln 2$ spins are frozen in specific orientations. Upon applying the transverse field, the eigenstates have the free spins pointing along $\hat{\mathbf{x}}$. The spread in energies is $2\Gamma Ng/\ln 2$, i.e., the shifts in energy density are proportional to g.

terms which we calculate below.

In addition, while the different terms in the expansion of $V_{\rm eff}(x,\epsilon'|\epsilon)$ can still be thought of as paths in configuration space, they acquire different weights depending on how they pass through clusters (see Eq. (2.52) and the coefficients associated with extra factors of V_{od}). We are unable to quantitatively account for these intra-cluster contributions to $V_{\rm eff}(x,\epsilon'|\epsilon)$. However, we expect them to be negligible at large p, since the cluster size is much smaller than the separation between clusters. The majority of each tunneling path lies outside of the clusters and contributes factors of $\Gamma/N\big(\epsilon-\epsilon(\sigma'')\big)$ exactly as in Eq. (2.59). The intra-cluster portions should give additive contributions to $\gamma(x,\epsilon'|\epsilon)$ which scale as $O\big(x^*(\epsilon)\big)$. Since $x^*(\epsilon)$ is exponentially small in p, these effects will be sub-leading and can be ignored. We shall thus continue to take

$$V_{\rm eff}(x,\epsilon'|\epsilon) = \Gamma \sum_P \prod_{\sigma''\in P} \frac{\Gamma}{N\big(\epsilon-\epsilon(\sigma'')\big)}. \tag{4.1}$$

Eq. (4.1) is nonetheless more difficult to evalute in the p-spin model than in the REM because the $\epsilon(\sigma'')$ are correlated[2]. We account for these correlations by using a path integral representation of $V_{\rm eff}(x,\epsilon'|\epsilon)$, from which we learn that the corrections relative to the REM value are no larger than $O(1/p)$ at large p.

Consider those tunneling paths along which the energy densities are a given function $\epsilon(y)$ $(0<y<x)$. Let the number of such paths be denoted $\mathcal{N}[\epsilon(y)]$. We can then write Eq. (4.1) as

$$\big|V_{\rm eff}(x,\epsilon'|\epsilon)\big| \sim \int \mathcal{D}\epsilon(y)\,\mathcal{N}[\epsilon(y)]\,e^{N\int_0^x {\rm d}y\,\ln\frac{\Gamma}{N|\epsilon-\epsilon(y)|}}. \tag{4.2}$$

We enforce the conditioning on $\epsilon(\sigma)$ and $\epsilon(\sigma')$ through boundary conditions: $\epsilon(y=0)=\epsilon$ and $\epsilon(y=x)=\epsilon'$. Eq. (4.2) is formally exact, since now $\mathcal{N}[\epsilon(y)]$ is the random variable which depends on the disorder realization. Importantly, we integrate only over $\epsilon(y)$ that are nowhere equal to ϵ, since the tunneling paths lie outside of the clusters.

We next make another "annealed" approximation:

$$\mathcal{N}[\epsilon(y)] \to \mathbb{E}\big[\mathcal{N}[\epsilon(y)]\big] = \big(Nx\big)!\,P[\epsilon(y)], \tag{4.3}$$

where $P[\epsilon(y)]$ is the *probability* of a given path having energy densities $\epsilon(y)$. Calculating $P[\epsilon(y)]$ exactly is intractable, yet we can infer the scaling with both N and p from the covariance matrix of the classical energies (Eq. (3.1)):

$$\mathbb{E}\big[\epsilon(\sigma_1)\epsilon(\sigma_2)\big] = \frac{1}{2N}\left(1-2x(\sigma_1,\sigma_2)\right)^p. \tag{4.4}$$

At large p, the right-hand side is independent of p on a length scale $x(\sigma_1,\sigma_2)\sim O\big(1/p\big)$. Thus $1/p$ can be identified as the "correlation length" for the classical energies. If $\epsilon(y)$ deviates from its mean throughout a distance x, then since

[2]Now the ϵ' variable is no longer superfluous.

the number of correlation lengths involved is px, this roughly corresponds to a number px of independent fluctuations, each of which is exponentially rare in N. Thus

$$P[\epsilon(y)] \sim e^{-Np\,c[\epsilon(y)]}, \tag{4.5}$$

where $c[\epsilon(y)]$ is independent of both N and p, with a unique minimum value of 0 at $\mathbb{E}\big[\epsilon(y)\big]$. Thus Eq. (4.2) becomes

$$\big|\,\langle\sigma'|V_{\text{eff}}|\sigma\rangle\,\big| \sim \int \mathcal{D}\epsilon(y)\, e^{N\left(x\ln\frac{x\Gamma}{e} - \int_0^x \mathrm{d}y\ \ln|\epsilon-\epsilon(y)| - p\,c[\epsilon(y)]\right)}. \tag{4.6}$$

At $p\to\infty$, the saddle point of the path integral is at $\epsilon^0(y) \equiv \mathbb{E}\big[\epsilon(y)\big]$ (see Sec. 2.2.2). To compute the correction from large but finite p, write $\epsilon(y) = \epsilon^0(y) + \delta\epsilon(y)$ and expand the exponent:

$$\begin{aligned} -\int_0^x \mathrm{d}y\ \ln|\epsilon-\epsilon(y)| - p\,c[\epsilon(y)] \sim -\int_0^x \mathrm{d}y\ \ln|\epsilon-\epsilon^0(y)| \,+\, \int_0^x \mathrm{d}y\,\frac{\delta\epsilon(y)}{\epsilon-\epsilon(y)} \\ -\,p\,\frac{\partial^2 c[\epsilon^0(y)]}{\partial\epsilon(y)\partial\epsilon(z)}\delta\epsilon(y)\delta\epsilon(z). \end{aligned} \tag{4.7}$$

There are no first derivatives of $c[\epsilon(y)]$ because $\epsilon^0(y)$ is the location of its minimum. Competition between the second and third terms in Eq. (4.7) determines the location of the saddle point. They are comparable for $\delta\epsilon(y) \sim O\big(1/p\big)$, which changes the value of the exponent at the saddle point by $O\big(1/p\big)$. This is the error made to $\langle\sigma'|V_{\text{eff}}|\sigma\rangle$, or rather $\gamma(x,\epsilon'|\epsilon)$, by approximating $\epsilon(y) \approx \mathbb{E}\big[\epsilon(y)\big]$, i.e., $\delta\epsilon(y) \approx 0$. It is indeed small at large p.

However, since the paths in Eq. (4.2) must obey the boundary conditions, $\mathbb{E}\big[\epsilon(y)\big]$ still includes correlations with ϵ and ϵ', the energy densities of $|\sigma\rangle$ and $|\sigma'\rangle$. Thus we need to average over ϵ'' in the joint distribution $P_3(\epsilon,\epsilon',\epsilon'')$, where the distance between $|\sigma\rangle$ and $|\sigma''\rangle$ is y and the distance between $|\sigma''\rangle$ and $|\sigma'\rangle$ is $x-y$. We discussed how to compute this distribution in Sec. 3.3.2. In the present case, the correlation matrix is

$$Q = \begin{pmatrix} 1 & (1-2x)^p & (1-2y)^p \\ (1-2x)^p & 1 & (1-2x+2y)^p \\ (1-2y)^p & (1-2x+2y)^p & 1 \end{pmatrix}. \tag{4.8}$$

Before computing Q^{-1}, let us write it in block-diagonal form as

$$Q^{-1} = \begin{pmatrix} A & \boldsymbol{b} \\ \boldsymbol{b}^T & c \end{pmatrix}, \tag{4.9}$$

where A is 2×2 and acts in the (ϵ,ϵ') subspace, $\boldsymbol{b}$ is 2×1, and c is 1×1. Then

$$\begin{aligned} P_3(\epsilon,\epsilon',\epsilon'') &= \exp\Big(-N\big(c\epsilon''^2 + 2\boldsymbol{b}^T\boldsymbol{\epsilon}\epsilon'' + \boldsymbol{\epsilon}^T A\boldsymbol{\epsilon}\big)\Big) \\ &= \exp\Big(-Nc\Big(\epsilon'' + \frac{\boldsymbol{b}^T\boldsymbol{\epsilon}}{c}\Big)^2 - N\boldsymbol{\epsilon}^T\Big(A - \frac{\boldsymbol{b}\boldsymbol{b}^T}{c}\Big)\boldsymbol{\epsilon}\Big), \end{aligned} \tag{4.10}$$

where $\boldsymbol{\epsilon} \equiv \begin{pmatrix} \epsilon & \epsilon' \end{pmatrix}^T$. We see that

$$\mathbb{E}\big[\epsilon''\big]\Big|_{\epsilon,\epsilon'} = -\frac{\boldsymbol{b}^T\boldsymbol{\epsilon}}{c}. \tag{4.11}$$

A direct calculation of the inverse gives

$$\mathbb{E}\big[\epsilon''\big]\Big|_{\epsilon,\epsilon'} = \frac{\mu(y)-\mu(x)\mu(x-y)}{1-\mu(x)^2}\,\epsilon \,+\, \frac{\mu(x-y)-\mu(x)\mu(y)}{1-\mu(x)^2}\,\epsilon', \tag{4.12}$$

where $\mu(z) \equiv (1-2z)^p$.

We thus have that

$$V_{\text{eff}}(x,\epsilon'|\epsilon) = \Gamma \sum_P \prod_{\sigma''\in P} \frac{\Gamma}{N\big(\epsilon - \mathbb{E}[\epsilon(\sigma'')]\big|_{\epsilon,\epsilon'}\big)} \sim e^{-N\gamma(x,\epsilon'|\epsilon)}, \tag{4.13}$$

where

$$\begin{aligned}\gamma(x,\epsilon'|\epsilon) = &-x\ln\frac{x\Gamma}{e|\epsilon|} \\ &+ \int_0^x \mathrm{d}y\,\ln\left|1 - \frac{\mu(y)-\mu(x)\mu(x-y)}{1-\mu(x)^2} - \frac{\mu(x-y)-\mu(x)\mu(y)}{1-\mu(x)^2}\frac{\epsilon'}{\epsilon}\right|.\end{aligned} \tag{4.14}$$

In particular, we will need $\gamma(x,\epsilon'|\epsilon)$ in two regimes: $x \sim O(1)$ and $x \ll 1/p$.

Let us first evaluate the integral assuming $x \sim O(1)$. Since $\mu(x)$ is exponentially small in p, the integral simplifies to

$$\int_0^x \mathrm{d}y\,\ln\left|1-\mu(y)-\mu(x-y)\frac{\epsilon'}{\epsilon}\right|. \tag{4.15}$$

Since $\mu(y)$ is exponentially small when $y \sim O(1)$ and $\mu(x-y)$ is exponentially small when $x-y \sim O(1)$, we can approximate the integral as

$$\int_0^x \mathrm{d}y\,\ln\Big|1-\mu(y)\Big| \,+\, \int_0^x \mathrm{d}y\,\ln\left|1-\mu(y)\frac{\epsilon'}{\epsilon}\right|. \tag{4.16}$$

Setting $y = z/p$, using that $\mu(y) \to e^{-2z}$ as $p\to\infty$, and taking the upper limit of integration to infinity, we are left with

$$\begin{aligned}\frac{1}{p}\int_0^\infty \mathrm{d}z\,\ln\left|1-e^{-2z}\right| \,+\, \frac{1}{p}\int_0^\infty \mathrm{d}z\,\ln\left|1-\frac{\epsilon'}{\epsilon}e^{-2z}\right| \\ = -\frac{\pi^2}{12p} \,+\, \frac{1}{p}\int_0^\infty \mathrm{d}z\,\ln\left|1-\frac{\epsilon'}{\epsilon}e^{-2z}\right|.\end{aligned} \tag{4.17}$$

Thus for $x \sim O(1)$,

$$\gamma(x,\epsilon'|\epsilon) \sim -x\ln\frac{x\Gamma}{e|\epsilon|} - \frac{K}{p}, \tag{4.18}$$

where

$$K \equiv \frac{\pi^2}{12} - \int_0^\infty \mathrm{d}z\,\ln\left|1-\frac{\epsilon'}{\epsilon}e^{-2z}\right|. \tag{4.19}$$

Let us next evaluate the integral assuming $x \ll 1/p$. Write

$$1 - \frac{\mu(y) - \mu(x)\mu(x-y)}{1-\mu(x)^2} - \frac{\mu(x-y) - \mu(x)\mu(y)}{1-\mu(x)^2}\frac{\epsilon'}{\epsilon} = 1 - \frac{\mu(y)+\mu(x-y)}{1+\mu(x)} - \frac{\mu(x-y)-\mu(x)\mu(y)}{1-\mu(x)^2}\frac{\delta\epsilon}{\epsilon}, \tag{4.20}$$

where $\delta\epsilon \equiv \epsilon' - \epsilon$. Since $x \ll 1/p$ and $0 < y < x$, we can expand all quantities:

$$1 - \frac{\mu(y)+\mu(x-y)}{1+\mu(x)} - \frac{\mu(x-y)-\mu(x)\mu(y)}{1-\mu(x)^2}\frac{\delta\epsilon}{\epsilon} \sim 2p^2 y(x-y) - \frac{y}{x}\frac{\delta\epsilon}{\epsilon}. \tag{4.21}$$

Then we have

$$\begin{aligned}
&\int_0^x \mathrm{d}y\, \ln\left(2p^2 y(x-y) + \frac{y}{x}\frac{\delta\epsilon}{|\epsilon|}\right) \\
&\quad = x\ln(2p^2x) - x + \int_0^x \mathrm{d}y\, \ln\left(x - y + \frac{1}{2p^2x}\frac{\delta\epsilon}{|\epsilon|}\right) \\
&\quad = x\ln(2p^2x) - 2x - \frac{1}{2p^2x}\frac{\delta\epsilon}{|\epsilon|}\ln\left(\frac{1}{2p^2x}\frac{\delta\epsilon}{|\epsilon|}\right) \\
&\qquad + \left(x + \frac{1}{2p^2x}\frac{\delta\epsilon}{|\epsilon|}\right)\ln\left(x + \frac{1}{2p^2x}\frac{\delta\epsilon}{|\epsilon|}\right).
\end{aligned} \tag{4.22}$$

Thus for $x \ll 1/p$,

$$\begin{aligned}
\gamma(x, \epsilon'|\epsilon) &= -x\ln\frac{e\Gamma}{2p^2|\epsilon|} - \frac{1}{2p^2x}\frac{\delta\epsilon}{|\epsilon|}\ln\left(\frac{1}{2p^2x}\frac{\delta\epsilon}{|\epsilon|}\right) \\
&\quad + \left(x + \frac{1}{2p^2x}\frac{\delta\epsilon}{|\epsilon|}\right)\ln\left(x + \frac{1}{2p^2x}\frac{\delta\epsilon}{|\epsilon|}\right).
\end{aligned} \tag{4.23}$$

One might have noticed that the correction to $\gamma(x, \epsilon'|\epsilon)$ from correlations with the initial and final states is of the same scale as the correction due to fluctuations about $\mathbb{E}\big[\epsilon(\sigma'')\big]$: $O(1/p)$. Thus we do not know whether the subleading terms in Eqs. (4.18) and (4.23) have the correct coefficients. We cannot be any more precise about the effect of fluctuations because we do not know the form of the functional $c[\epsilon(y)]$ in Eq. (4.5). However, this issue is somewhat beside the point. The most important features of the effective coupling are that: 1) the finite-p corrections are small at large p, and 2) the coupling is larger to states having $\epsilon' = \epsilon$ than states having $\epsilon' > \epsilon$. These features have been demonstrated carefully. Our use of Eqs. (4.18) and (4.23) is largely for concreteness, and we will explicitly note how our conclusions do not depend on the precise form of $\gamma(x, \epsilon'|\epsilon)$ at the appropriate moments.

4.2 The phase diagram

The eigenstate and dynamical phases of the p-spin model are defined by the same conditions as for the REM. Given an initial $\hat{\sigma}^z$ state $|\sigma\rangle$ with energy density ϵ,

the expected number of resonant states at distance x is $e^{Ng(x,\epsilon)-N\gamma(x,\epsilon)}$ and the total weight on states having ϵ' is $e^{Ng(x,\epsilon'|\epsilon)-2N\gamma(x,\epsilon'|\epsilon)}$. The trapped phase is defined by

$$\max_{x\in[x^{**}(\epsilon),1-x^{**}(\epsilon)]}\left[g(x,\epsilon)-\gamma(x,\epsilon)\right]<0, \tag{4.24}$$

the tunneling phase by

$$\begin{aligned}\max_{x\in[x^{**}(\epsilon),1-x^{**}(\epsilon)]}\left[g(x,\epsilon)-\gamma(x,\epsilon)\right]&>0,\\ \max_{x\in[0,1]}\left[\max_{\epsilon'}\left[g(x,\epsilon'|\epsilon)-2\gamma(x,\epsilon'|\epsilon)\right]\right]&<0,\end{aligned} \tag{4.25}$$

and the excited phase by

$$\max_{x\in[0,1]}\left[\max_{\epsilon'}\left[g(x,\epsilon'|\epsilon)-2\gamma(x,\epsilon'|\epsilon)\right]\right]>0. \tag{4.26}$$

Note that now, the limits on which x to optimize over are important. We only consider tunneling to states at $x > x^{**}(\epsilon)$, since these are the distances at which different clusters lie, but consider the non-resonant weight on states at all distances.

One important new feature is the existence of ϵ_d. The trapped and tunneling phases are not even defined for $\epsilon > \epsilon_d$ because disjoint clusters do not exist. We expect the eigenstates to obey the ETH and the dynamics to rapidly thermalize for any non-zero Γ at such high energies. The situation is sketched in Fig. 4.2.

4.2.1 Phase boundaries

The phase boundaries are shifted only slightly relative to the REM. For the tunneling transition, we have

$$g(x,\epsilon)-\gamma(x,\epsilon)\sim x\ln\frac{\Gamma}{e|\epsilon|}-(1-x)\ln(1-x)-\epsilon^2+\frac{\pi^2}{6p}. \tag{4.27}$$

The maximum over $x\in\left[x^{**}(\epsilon),1-x^{**}(\epsilon)\right]$ is

$$\ln\frac{\Gamma}{|\epsilon|}-1+\frac{|\epsilon|}{\Gamma}-\epsilon^2+\frac{\pi^2}{6p}, \tag{4.28}$$

which is 0 at the trapped-tunneling phase boundary. Denoting the REM solution at $p\to\infty$ by $\Gamma^{\infty}_{\text{tun}}(\epsilon)$, we have that

$$\Gamma_{\text{tun}}(\epsilon)=\Gamma^{\infty}_{\text{tun}}(\epsilon)\left(1-\frac{\pi^2}{6p}\frac{\Gamma^{\infty}_{\text{tun}}(\epsilon)}{\Gamma^{\infty}_{\text{tun}}(\epsilon)-\epsilon}\right). \tag{4.29}$$

The excitation transition is more subtle. First consider $x\sim O(1)$ with respect to p:

$$\begin{aligned}&g(x,\epsilon'|\epsilon)-2\gamma(x,\epsilon'|\epsilon)\\ &\qquad\sim 2x\ln\frac{\Gamma}{e|\epsilon|}+x\ln x-(1-x)\ln(1-x)-\epsilon'^2+\frac{\pi^2}{6p}+\frac{\epsilon'}{p\epsilon},\end{aligned} \tag{4.30}$$

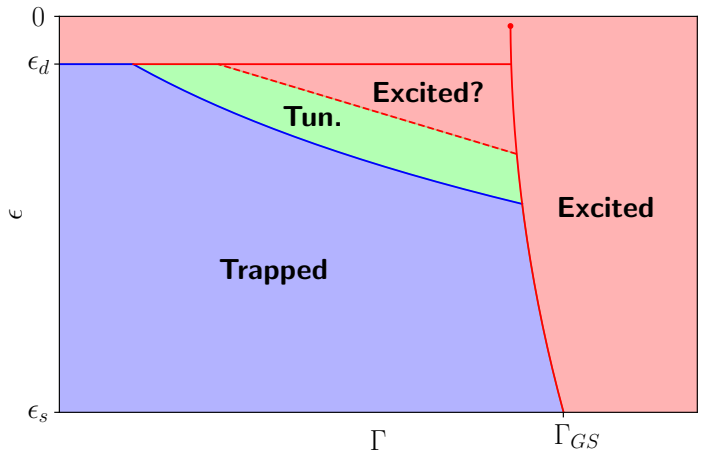

Figure 4.2: A sketch of the dynamical phase diagram of the p-spin model. The system tunnels between clusters in the "tunneling" phase (green), remains trapped in a cluster in the "trapped" phase, and is excited out of clusters in the "excited" phase. See Fig. 2.6 and Sec. 2.4.1 for comments on the "excited?" phase. Compared to the REM, note that the trapped and tunneling phases are cut off at ϵ_d, and that the first-order line terminates at high energy [104].

where we have anticipated that $\epsilon' \ll \epsilon$. The maximization over ϵ', which occurs at $\epsilon' = 1/2p\epsilon$, gives

$$2x \ln \frac{\Gamma}{e|\epsilon|} + x \ln x - (1-x) \ln (1-x) + \frac{\pi^2}{6p} + O\left(\frac{1}{p^2}\right), \tag{4.31}$$

and the maximization over x then gives

$$\frac{1+D}{2} \ln \frac{1+D}{2} - \frac{1-D}{2} \ln \frac{1-D}{2} + (1+D)\left(\ln \frac{\Gamma}{|\epsilon|} - 1\right) + \frac{\pi^2}{6p}, \tag{4.32}$$

where $D \equiv \sqrt{1 - 4\epsilon^2/\Gamma^2}$. We set this expression to 0 and obtain

$$\Gamma_{\text{exc}}(\epsilon) \sim \left(2.485 - \frac{2.565}{p}\right) |\epsilon|. \tag{4.33}$$

The coefficients are approximate, but the proportionality to $|\epsilon|$ is exact.

As mentioned above, the most important feature of Eqs. (4.29) and (4.33) is simply that the finite-p corrections are small. This is due to the corrections in $g(x, \epsilon'|\epsilon)$ and $\gamma(x, \epsilon'|\epsilon)$ being small, regardless of the specific functional form.

Now let us turn to $x \ll 1/p$:

$$g(x,\epsilon'|\epsilon) - 2\gamma(x,\epsilon'|\epsilon) \sim x \ln \frac{e^3\Gamma^2}{4p^4\epsilon^2 x} - \frac{(\delta\epsilon - 2p|\epsilon|x)^2}{4px} + \frac{1}{p^2 x}\frac{\delta\epsilon}{|\epsilon|}\ln\left(\frac{1}{2p^2x}\frac{\delta\epsilon}{|\epsilon|}\right) - 2\left(x + \frac{1}{2p^2x}\frac{\delta\epsilon}{|\epsilon|}\right)\ln\left(x + \frac{1}{2p^2x}\frac{\delta\epsilon}{|\epsilon|}\right). \tag{4.34}$$

The maximization over ϵ' is at $\delta\epsilon \sim 2p|\epsilon|x$ and gives

$$x \ln \frac{e\Gamma^2}{4p^2\epsilon^2 x} + O\left(\frac{1}{p^3}\right). \tag{4.35}$$

This expression is maximized at

$$x_m = \frac{\Gamma^2}{4p^2\epsilon^2}, \tag{4.36}$$

and importantly, the value of the maximum is positive. Thus strictly speaking, one can never satisfy the non-excitation condition in Eq. (4.25). However, this does not imply that the system escapes from its initial cluster: Eq. (4.36) indicates that the system moves through a distance $O(1/p^2)$ and the energy changes by $O(1/p)$, yet we found in Sec. 3.3.3 that the energy barriers between clusters are much larger, at a distance $O(1/p)$ and height $O(1)$. To check if the system is excited out of clusters, one should modify the non-excitation condition to maximize over $x \gtrsim O(1/p)$. Then the finite-p corrections to $\gamma(x,\epsilon'|\epsilon)$ are sub-leading and we are back to Eq. (4.33).

Similarly, suppose that we had not restricted ourselves to $x > x^{**}(\epsilon)$ in Eq. (4.24), and in particular had allowed $x < x^*(\epsilon)$, i.e., distances lying within the same cluster. We would have

$$g(x,\epsilon) - \gamma(x,\epsilon) \sim x \ln \frac{e^2\Gamma}{2p^2|\epsilon|x^2} - p\epsilon^2 x. \tag{4.37}$$

Eq. (4.37) is positive throughout $x < x^*(\epsilon)$, meaning that there are resonant configurations throughout the initial cluster, even for arbitrarily small Γ. One can understand this on conceptual grounds, without relying on a specific form for $\gamma(x,\epsilon)$. Starting from a configuration $|\sigma\rangle$, the correlations in the p-spin model are such that the energy (*not* per spin) changes by $O(p)$ when one flips a single spin. Yet the energy costs are random, and since there are N possibilities for which spin to flip, a non-zero fraction of the spins will have arbitrarily small energy costs to flipping. The eigenstate $|\Psi_\sigma\rangle$ hybridizes among these free spins, and the perturbation theory breaks down, for any non-zero Γ.

Our interpretation of this result is that the eigenstates automatically thermalize within individual clusters, and the trapped states are those which do not thermalize *between* clusters. We give a precise statement of this phenomenon in Sec. 4.3. It is consistent with our broader understanding of the quantum p-spin model. Macroscopic energy barriers are responsible for completely suppressing

tunneling in the trapped phase and restricting it to exponential timescales in the tunneling phase, yet these barriers by definition do not exist within a single cluster. There is nothing to prevent the system from moving throughout a cluster, regardless of what happens in the configuration space as a whole.

4.2.2 Tunneling rates

Let us now return to the matching problem and the question of timescales in the tunneling phase. Recall that we compare quantum dynamics to thermal activation and the unstructured search, with runtimes τ_{q}, τ_{th}, and τ_{unstr}, respectively.

Tunneling continues to be exponentially faster than activation for large but finite p. This follows from the fact that for $x \sim O(1)$, the density of states has exponent

$$g(x,\epsilon) = \max_{\epsilon'} \left[g(x,\epsilon'|\epsilon) \right] - \epsilon^2 + e^{-O(p)}, \tag{4.38}$$

and the effective coupling has exponent

$$\gamma(x,\epsilon) = \gamma(x,\epsilon' \neq \epsilon|\epsilon) - O\left(\frac{1}{p}\right). \tag{4.39}$$

See Secs. 3.3 and 4.1, respectively. Thus $N^{-1}\ln\tau_{\mathrm{q}}$ is corrected only by $O(1/p)$ relative to the REM value. Similarly, given that the height of the energy barriers is close to the REM value and the distance from the cluster centers is close to 0 (Sec. 3.3.3), $N^{-1}\ln\tau_{\mathrm{th}}$ also has corrections small in $1/p$. These corrections cannot compensate for the leading-order result that $N^{-1}\ln\tau_{\mathrm{q}} < N^{-1}\ln\tau_{\mathrm{th}}$ by $O(1)$.

The comparison between tunneling and unstructured search is more interesting at finite p, and indeed, tunneling is now *faster* in a portion of the tunneling phase. It is known that the entropy density of the p-spin model is exactly equal to the REM expression for all $\epsilon > \epsilon_s$ [77], thus the runtime for unstructured search is again given by Eq. (2.74), written here as

$$\frac{1}{N}\ln\tau_{\mathrm{unstr}} = \epsilon^2. \tag{4.40}$$

From Eqs. (4.38) and (4.39),

$$\begin{aligned} \frac{1}{N}\ln\tau_{\mathrm{q}} &= -\max_{x\in[x^{**}(\epsilon),1-x^{**}(\epsilon)]} \left[g(x,\epsilon) - 2\gamma(x,\epsilon) \right] \\ &= -\max_{x\in[x^{**}(\epsilon),1-x^{**}(\epsilon)]} \left[\max_{\epsilon'} \left[g(x,\epsilon'|\epsilon) - 2\gamma(x,\epsilon'|\epsilon) \right] \right] + \epsilon^2 - O\left(\frac{1}{p}\right). \end{aligned} \tag{4.41}$$

Precisely on the excitation boundary, the first term on the right-hand side is zero by definition[3]. Thus $N^{-1}\ln\tau_{\mathrm{q}}$ is smaller than $\epsilon^2 = N^{-1}\ln\tau_{\mathrm{unstr}}$ by $O(1/p)$

[3] As noted in Sec. 2.3.2, one can check in the REM that the maximum over all $x \in [0,1]$ indeed lies within $[x^{**}(\epsilon), 1-x^{**}(\epsilon)]$. By continuity, this is true for large but finite p as well.

on the boundary. By continuity, tunneling is faster than unstructured search for an entire range of $\Gamma < \Gamma_{\text{exc}}(\epsilon)$ in the tunneling phase.

As trivial as the unstructured search is, we are not aware of any classical search algorithm that can perform better at large p, where the energy landscape is similar to the uncorrelated landscape of the REM (for which unstructured search must be optimal, since the energy levels are independent). Thus to the best of our knowledge, the quantum energy matching algorithm presented here is more efficient than any classical method for solving matching problems in this regime. The algorithm does not require exponential precision or knowledge of the level structure. While one must be able to identify the tunneling phase and tune the transverse field close to the excitation boundary, these requirements do not scale with the *size* of the problem. This approach thus has a fundamental advantage over other quantum algorithms, which require unreasonable amounts of control [105].

4.3 Eigenstate structure in the trapped phase

We are finally in a position to sharply distinguish the trapped phase of eigenstates from the existing categories, namely ETH and MBL. We shall do so in terms of the matrix elements of local operators between eigenstates. Recall from the Introduction that the ETH asserts

$$\langle \Phi | \hat{A} | \Psi \rangle \sim e^{-Ns(\epsilon)/2} f(\epsilon, \omega), \tag{4.42}$$

for two eigenstates $|\Phi\rangle$ and $|\Psi\rangle$ with energies $E_\Phi \equiv N\epsilon + \omega/2$ and $E_\Psi \equiv N\epsilon - \omega/2$. The essence of the statement is that all eigenstates at energy density ϵ are coupled with comparable magnitude by local operators. See the Introduction for a more thorough description.

Using the l-bit description (also in the Introduction), we can make a contrasting statement about MBL:

$$\langle \Phi | \hat{A} | \Psi \rangle \sim \begin{cases} O(1) & , \quad \text{supp}\big[|\tau_\Phi - \tau_\Psi|\big] \subset \text{supp}\big[\hat{A}\big] \\ 0 & , \quad \text{otherwise} \end{cases}, \tag{4.43}$$

where the (admittedly schematic) notation in the upper line indicates that those sites on which the l-bits of $|\Phi\rangle$ and $|\Psi\rangle$ differ are contained in the support of $\hat{A}$. Given that the l-bits are quasi-local, there are only $O(1)$-many $|\Phi\rangle$ for which this is true per $|\Psi\rangle$. For example, if $\hat{A} = \hat{\sigma}_i^z$, then since $\hat{\sigma}_i^z$ has an expansion in l-bits with an exponentially decaying envelope, $\hat{A}$ couples $|\Psi\rangle$ only to those $|\Phi\rangle$ which are identical outside of a localization length around site i. The number of such $|\Phi\rangle$ is $2^{O(\xi)}$, i.e., $O(1)$. To summarize, in an MBL phase, local operators couple an eigenstate to only $O(1)$-many others.

The trapped phase is intermediate between these two extremes. Each trapped eigenstate is associated with one of the exponentially many clusters, and local operators do not couple between clusters. Yet there are exponentially many

states per cluster, and local operators do couple all those within a cluster. We have

$$\langle\Phi|\hat{A}|\Psi\rangle \sim \begin{cases} e^{-Ns_c(\epsilon)/2} f_c(\epsilon,\omega) & , \quad c_\Phi = c_\Psi \\ 0 & , \quad \text{otherwise} \end{cases}, \tag{4.44}$$

where c_Φ and c_Ψ denote the clusters to which $|\Phi\rangle$ and $|\Psi\rangle$ belong. $s_c(\epsilon)$ is the entropy density of a single cluster, and $f_c(\epsilon,\omega)$ is a smooth cluster-dependent function.

In terms of the standard diagnostics, the trapped phase has much in common with MBL. To be more precise, we need a concrete model for the trapped wavefunctions. We shall take each state to have $O(1)$ amplitude on configurations within the cluster and have the typical amplitude $e^{-N\gamma(x,\epsilon'|\epsilon)}$ on configurations outside the cluster (in the "tail" of the wavefunction). Note that most of the weight is in fact in the tail. The total weight at distance x is (see Eqs. (4.34) and (4.35))

$$\begin{aligned} W(x) \equiv \int \mathrm{d}\epsilon'\, e^{N\left(g(x,\epsilon'|\epsilon)-2\gamma(x,\epsilon'|\epsilon)\right)} &\sim \exp\left(N \max_{\epsilon'}\left(g(x,\epsilon'|\epsilon)-2\gamma(x,\epsilon'|\epsilon)\right)\right) \\ &\sim \exp\left(Nx\ln\frac{e\Gamma^2}{4p^2\epsilon^2 x}\right), \end{aligned} \tag{4.45}$$

which is maximized at x_m:

$$x_m = \frac{\Gamma^2}{4p^2\epsilon^2}, \quad W(x_m) = \exp\left(N\frac{\Gamma^2}{4p^2\epsilon^2}\right). \tag{4.46}$$

Compare to the total weight within the cluster, which is only $\exp\left(Ne^{-O(p)}\right)$ (see Sec. 3.3.3).

Let us first compute the IPR:

$$Y_2 \equiv \sum_\sigma \frac{\left|\langle\sigma|\Psi\rangle\right|^4}{\left(\sum_{\sigma'}|\langle\sigma'|\Psi\rangle|^2\right)^2}. \tag{4.47}$$

Using our ansatz for $|\Psi\rangle$,

$$\sum_\sigma \left|\langle\sigma|\Psi\rangle\right|^4 \sim \int \mathrm{d}x \int \mathrm{d}\epsilon'\, e^{N\left(g(x,\epsilon'|\epsilon)-4\gamma(x,\epsilon'|\epsilon)\right)} \sim \exp\left(N\frac{\Gamma^4}{16p^4\epsilon^4}\right). \tag{4.48}$$

Thus

$$Y_2 \sim \exp\left(-N\frac{\Gamma^2}{2p^2\epsilon^2}\left(1-\frac{\Gamma^2}{8p^2\epsilon^2}\right)\right). \tag{4.49}$$

Although the IPR is exponentially small, it is exponentially larger than in a thermal state, for which one would expect $Y_2 \sim e^{-Ns(\epsilon)}$.

Our next quantity is

$$q_{\mathrm{ES}} \equiv \frac{1}{N}\sum_i \left(\frac{\langle\Psi|\hat{\sigma}_i^z|\Psi\rangle}{\langle\Psi|\Psi\rangle}\right)^2, \tag{4.50}$$

which is the eigenstate analogue to a common order parameter in spin glass theory: $q \equiv N^{-1}\sum_i \langle\sigma_i^z\rangle^2$ [63, 106]. One would have $q_{\rm ES} = 0$ in an ETH phase and $q_{\rm ES} \neq 0$ in an MBL phase. To evaluate Eq. (4.50), write

$$\begin{aligned} q_{\rm ES} &= \frac{1}{N\langle\Psi|\Psi\rangle^2}\sum_i\left(\sum_\sigma \big|\langle\sigma|\Psi\rangle\big|^2\sigma_i\right)^2 \\ &= \frac{1}{\langle\Psi|\Psi\rangle^2}\sum_{\sigma\sigma'}\big|\langle\sigma|\Psi\rangle\big|^2\big|\langle\sigma'|\Psi\rangle\big|^2\left(\frac{1}{N}\sum_i\sigma_i\sigma_i'\right). \end{aligned} \tag{4.51}$$

Recall that $N^{-1}\sum_i \sigma_i\sigma_i' = 1 - 2x(\sigma,\sigma')$. We thus have

$$\begin{aligned} q_{\rm ES} = e^{-N\frac{\Gamma^2}{2p^2\epsilon^2}}\int {\rm d}x\int {\rm d}y\int {\rm d}z\binom{N}{Nx}\binom{Nx}{N\frac{x-y+z}{2}}\binom{N(1-x)}{N\frac{y-x+z}{2}} \\ \cdot\left(\frac{e\Gamma}{2p^2|\epsilon|}\right)^{2Nx}\left(\frac{e\Gamma}{2p^2|\epsilon|}\right)^{2Ny}(1-2z), \end{aligned} \tag{4.52}$$

where x and y are the distances of σ and σ' from the origin, z is the distance from each other, the binomial coefficients together give the number of configurations with such a geometry, and we have already performed the integrals over the energies at x and y (ignoring the correlations between them for simplicity). The saddle-point in z is at $z^* = x + y - 2xy$, and

$$\binom{Nx}{N\frac{x-y+z^*}{2}}\binom{N(1-x)}{N\frac{y-x+z^*}{2}} \sim \binom{N}{Ny}. \tag{4.53}$$

We are left with separate integrals over x and y, each of which has a saddle-point at $\Gamma^2/4p^2\epsilon^2$, thus

$$q_{\rm ES} \sim 1 - \frac{\Gamma^2}{p^2\epsilon^2}. \tag{4.54}$$

Trapped eigenstates have $q_{\rm ES} \neq 0$, similar to many-body localized states, and in fact $q_{\rm ES} \to 1$ as $p \to \infty$.

The level spacing statistics in the trapped phase will follow the Poisson distribution. If one could isolate the levels within a single cluster, they would exhibit GOE statistics. However, the spectra of different clusters interpenetrate, and as the clusters are essentially uncoupled, their spectra are independent. Thus the level spacing statistics as a whole obey Poisson.

The final quantity which we shall discuss highlights the distinction between ETH, MBL, and trapped phases quite well. It is the $\hat\sigma_i^z$-$\hat\sigma_i^z$ autocorrelation function, evaluated in an eigenstate for simplicity:

$$C(t) \equiv \langle\Psi|\hat\sigma_i^z(t)\hat\sigma_i^z(0)|\Psi\rangle\,. \tag{4.55}$$

Inserting a set of energy eigenstates, we have

$$C(t) = \sum_\Phi e^{i(E_\Psi - E_\Phi)t}\big|\langle\Phi|\hat\sigma_i^z|\Psi\rangle\big|^2. \tag{4.56}$$

First consider the situation in which the eigenstates obey the ETH. Denote the equilibrium value of $\hat{\sigma}_i^z$ by σ_{eq}. We have

$$C(t) = \sigma_{\text{eq}}^2 + \sum_{\Phi \neq \Psi} e^{i(E_\Psi - E_\Phi)t} \frac{R_{\Phi\Psi}^2}{e^{N s(\epsilon)}} \big| f(\epsilon, \omega) \big|^2. \tag{4.57}$$

The function $f(\epsilon, \omega)$ decays to 0 for $\omega \sim O(1)$, so we can consider the sum as only over $|\Phi\rangle$ with the same energy density ϵ as $|\Psi\rangle$. Given the exponentially large density of states, the sum over Φ should average out any fluctuations in $R_{\Phi\Psi}^2$, so that we can replace $R_{\Phi\Psi}^2$ by 1. Thus

$$C(t) \sim \sigma_{\text{eq}}^2 + \int \mathrm{d}\omega \, e^{i\omega t} \big| f(\epsilon, \omega) \big|^2. \tag{4.58}$$

Since $|f(\epsilon, \omega)|^2$ is a smooth function, we know that the Fourier transform decays to 0 as $t \to \infty$ faster than a power law. We have thus established that in an ETH phase, the autocorrelation function decays to the equilibrium value in a reasonably short amount of time.

Next consider the MBL case. The matrix elements $\langle \Phi | \hat{\sigma}_i^z | \Psi \rangle$ are significant only for $O(1)$-many $|\Phi\rangle$, namely those whose flipped l-bits relative to $|\Psi\rangle$ lie within a localization length of site i. Number the significant states as $\{|\Phi_1\rangle, |\Phi_2\rangle, \cdots, |\Phi_M\rangle\}$, where $M \sim 2^{O(\xi)}$. We have that

$$C(t) = \sum_{m=1}^{M} \big| \langle \Phi_m | \hat{\sigma}_i^z | \Psi \rangle \big|^2 e^{i(E_\Psi - E_{\Phi_m})t}. \tag{4.59}$$

The important feature here is that, as a sum over a finite number of oscillating terms, $C(t)$ never decays. It may fluctuate erratically, especially if $\xi \gg 1$, but it never settles into a steady-state value.

Finally, consider the trapped phase. Here the matrix elements are significant only for those $|\Phi\rangle$ in the same cluster c as $|\Psi\rangle$. Furthermore, the expectation value $\langle \Psi | \hat{\sigma}_i^z | \Psi \rangle$ does not equal the equilibrium average σ_{eq} but rather an average restricted to the cluster c, i.e., σ_c. We thus have

$$C(t) = \sigma_c^2 + \sum_{\Phi \neq \Psi,\, \Phi \in c} e^{i(E_\Psi - E_\Phi)t} \frac{R_{\Phi\Psi}^2}{e^{N s_c(\epsilon)}} \big| f_c(\epsilon, \omega) \big|^2. \tag{4.60}$$

Even though the internal entropy of the cluster, $s_c(\epsilon)$, is less than the full thermodynamic entropy, it is still non-zero. Thus exponentially many states are included in the sum. The arguments from the ETH case apply here as well, and

$$C(t) \sim \sigma_c^2 + \int \mathrm{d}\omega \, e^{i\omega t} \big| f_c(\epsilon, \omega) \big|^2. \tag{4.61}$$

The autocorrelation function does approach a steady-state value as $t \to \infty$, but one that is not the equilibrium value.

This summarizes the difference between the three eigenstate phases discussed in this thesis. In an ETH phase, observables decay to their equilibrium values

over time. In a trapped phase, observables decay to non-equilibrium values over time. In an MBL phase, observables do not decay over time. We have shown that the previously undiscovered trapped phase manifests in the quantum p-spin model of spin glass theory. Furthermore, keep in mind the generality of what we have discussed. The specific functional forms of the two ingredients in our theoretical analysis, the distance-resolved density of states $e^{Ng(x,\epsilon'|\epsilon)}$ and the effective coupling $e^{-N\gamma(x,\epsilon'|\epsilon)}$, were not particularly important. All that mattered was that both scale exponentially with N, which in turn relied only on having clusters of states separated by macroscopic energy barriers. Many interesting models, especially those relevant in the quantum computing field, exhibit the same features. The physics of the trapped phase is important for these models and has significant implications for the performance of quantum algorithms.

Part II

Additional topics in disordered systems

Chapter 5

Sign phase transition in the problem of interfering directed paths

In this chapter, we investigate the statistical properties of interfering directed paths in disordered media. The work is published in Ref. [107]. On a technical level, this chapter shares with the previous ones the feature of studying sums over directed paths. However, that is where the similarities end. Here we are concerned with paths on finite-dimensional lattices and focus on characterizing the role that interference between paths plays. Two possibilities are that the average sign of the path sum tends to zero at long distance (sign-disordered) or that the average sign remains finite (sign-ordered). We discuss the physical implications and show that dimensionality plays a very important role.

5.1 Background

An example of directed paths in a random medium is shown schematically in Fig. 5.1, where solid lines correspond to directed "tunneling" paths and blue dots represent scattering sites. Important physical settings for interfering directed paths include hopping conduction in doped semiconductors [37,108], spin glasses at high temperature [109], and granular D-wave superconductors [110,111]. We describe these applications in more detail below. First, let us introduce the common mathematical structure among them and motivate the question which we shall address.

In each of these settings, the physics is determined by the statistics of a sum over paths:

$$A = \sum_{\Gamma} A_{\Gamma}, \quad A_{\Gamma} = \prod_{j \in \Gamma} \alpha_j, \tag{5.1}$$

where A_Γ is the tunneling amplitude of path Γ, given as a product of scattering

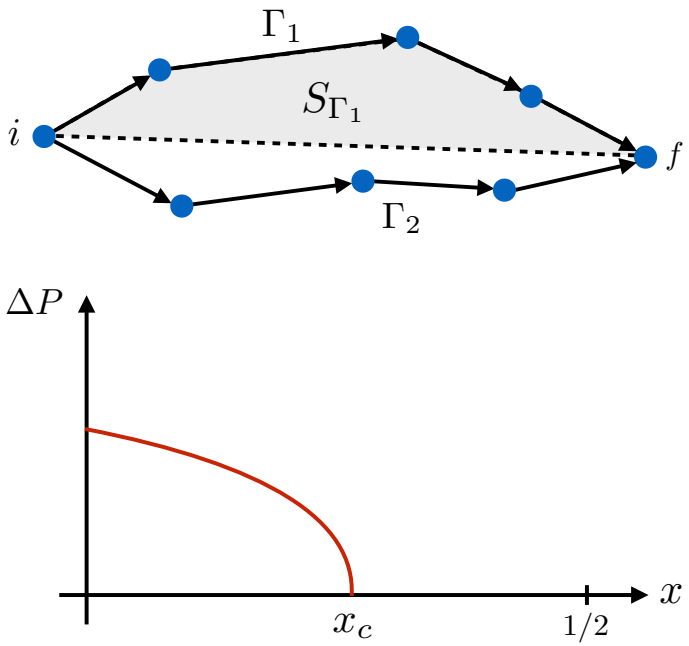

Figure 5.1: (top) Schematic of interfering directed paths in a random medium. Γ_1 and Γ_2 are two different paths from site i to f. S_{Γ_1} is the area enclosed by Γ_1 relative to the line joining i and f. (bottom) Sketch of the order parameter for the sign phase transition.

amplitudes α_j along the path (see Fig. 5.1). If the amplitudes α_j have random signs, so too does the sum A. The destructive interference at large distances $r \equiv |\mathbf{r}_f - \mathbf{r}_i|$ is characterized by whether the sum A is more likely to be positive than negative:

$$\Delta P_{r\to\infty} \equiv \Delta P \equiv \Pr[A > 0] - \Pr[A < 0]. \tag{5.2}$$

It was suggested in [108,112] that the path sum exhibits a "sign phase transition" at a critical concentration of negative scattering sites x_c. For example, if

$$\alpha_j = \begin{cases} 1 & \text{with probability } 1-x \\ -M & \text{with probability } x \end{cases} \tag{5.3}$$

then

$$\begin{array}{ll} \Delta P > 0 & \text{for } x < x_c, \\ \Delta P = 0 & \text{for } x > x_c. \end{array} \tag{5.4}$$

The quantity $\Delta P(x)$ serves as an order parameter for the sign phase transition. Such a transition is shown qualitatively in the bottom of Fig. 5.1.

It was argued in [108] that the upper critical dimension for the sign phase transition is four. The lower critical dimension has been debated, and in particular, whether the sign-ordered phase exists in 2D has remained unresolved for a long time [108, 113–121].

We show conclusively that the sign-ordered phase does not exist in 2D ($\Delta P = 0$ for any $x > 0$), and present strong numerical evidence that it does exist in 3D. The former result is consistent with some of the previous studies (see in particular [120]). We explain the instability of the sign-ordered phase at small values of x by identifying the rare fluctuations which destabilize the sign order. These lead to an anomalously large correlation length which scales stretched-exponentially with x and explains the apparent sign order observed in previous numerical studies [112, 115, 118, 121].

The (non-)existence of the sign-ordered phase and associated transition has immediate consequences for the following physical systems:

1. The quantity A in Eq. (5.1) can play the role of the electron tunneling amplitude in a disordered medium, where it arises as a sum of partial amplitudes corresponding to different tunneling paths [108, 112, 122–128]. It was argued in Refs. [108,112,127] that the sign of the magnetoresistance in the hopping conductivity regime depends on whether the system is in the sign-ordered or -disordered phase.

2. In the Edwards-Anderson spin glass, the spin correlation function at high temperature is governed by a sum analogous to A, where the α_j correspond to bond disorder. Thus, the presence of a sign-ordered phase in 3D implies that a transition takes place in the sign of the correlation functions at high temperature.

3. At high temperature, the correlation function $\chi = \langle \exp(i(\theta_i - \theta_j)) \rangle$ in a system of randomly oriented and randomly shaped grains of D-wave superconductor embedded into a metallic matrix can be reduced to Eq. (5.1). Here, θ_i is the phase of the order parameter on grain i. In analogy with the magnetoresistance in the hopping conductivity regime, the magnetic field suppresses superconductivity in the sign-ordered phase and enhances it in the sign-disordered phase.

We will return to these applications in more detail in Sec. 5.3, after presenting the technical results in Sec. 5.2.

5.2 The sign phase transition

5.2.1 Mean-field description and generalities

The essential picture of the sign-ordered phase is illustrated in the "space-time" diagram of Fig. 5.2. Here, the "time" coordinate t corresponds to the direction of propagation of the directed paths and the "spatial" coordinates s to the

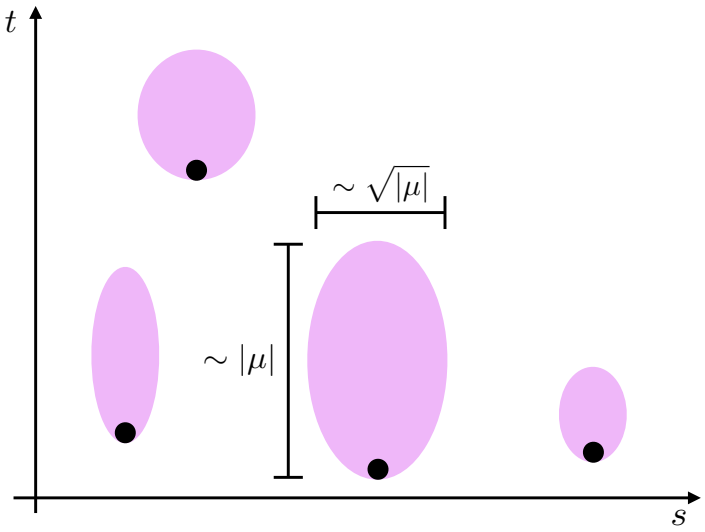

Figure 5.2: Regions in which the path sum is negative (purple), created by isolated negative scatterers (black dots). Although each region has a random size, the typical scales are as shown. The paths are directed along t. The scattering length μ characterizes the strength of the scatterer, see [121] for details.

$d-1$ transverse directions. Negative-amplitude scatterers produce cigar-shaped negative domains in the sign

$$\sigma(s,t) \equiv \mathrm{sgn}[A(s,t)] \tag{5.5}$$

of the amplitude field.

For an isolated negative scatterer in an otherwise uniform lattice of positive scatterers, the sign at (s,t) is determined by the interference between those paths which go through the negative scatterer and those which miss it. If the scattering amplitude is sufficiently large, the path sum may be estimated in the diffusive limit [121],

$$A(s,t) \propto 1 - \left(\frac{|\mu|}{t}\right)^{\frac{d-1}{2}} e^{-\frac{s^2}{4Dt}} \tag{5.6}$$

where the scattering length μ characterizes the strength of the negative scatterer, D is a microscopic length, and we have suppressed an $O(1)$ constant. We find that the negative domain $A < 0$ has extent $\tau \sim |\mu|$, width $w \sim \sqrt{|\mu|}$, and volume $\mathfrak{v} \sim |\mu|^{\frac{d+1}{2}}$. At sufficiently small concentration of scatterers x, the negative domains remain far apart and do not interfere. The sign field $\sigma(s,t)$ only disorders if the domains percolate, i.e., when

$$x\mathfrak{v} = x|\mu|^{\frac{d+1}{2}} \gtrsim 1. \tag{5.7}$$

Thus this picture predicts a finite x_c for sign order in any dimension $d > 1$[1].

This argument neglects fluctuations in the size of the isolated negative domains. Should the distribution of domains have a sufficiently long tail, then sign order becomes unstable even at very small x, as argued by [120]. Suppose that the distribution of domain lengths τ has a power-law tail, $p_s(\tau) \sim \tau^{-\eta}$, and that the typical transverse width of such domains is $w(\tau) \sim \tau^{\gamma}$. We refer to η as the "survival" exponent and γ as the "growth" exponent. The fraction of the transverse volume occupied by negative domains at time t is

$$x \int^t dt' p_s(t-t') w(t-t')^{d-1}. \tag{5.8}$$

This fraction converges as $t \to \infty$ provided

$$1 - \eta + (d-1)\gamma < 0. \tag{5.9}$$

Inequality (5.9) is a necessary condition for the stability of the sign-ordered phase with respect to these fluctuations.

Since the sign $\sigma(s,t)$ takes values in $\{+,-\}$, it is instructive to interpret it as an Ising field in $d-1$ spatial dimensions s and temporal dimension t which evolves in the presence of "noise" given by the scattering disorder. In this language, the sign order parameter is simply the magnetization as $t \to \infty$,

$$\begin{aligned} \mathbb{E}[\sigma(s,t)] &= \Pr[A(s,t) > 0] - \Pr[A(s,t) < 0] \\ &= \Delta P(s,t). \end{aligned} \tag{5.10}$$

Here $\mathbb{E}[\cdot]$ denotes averaging with respect to the random distribution of scatterers (i.e., the noise). The steady state resulting from the noise need not correspond to equilibrium with respect to any Ising model. Nevertheless, one might suspect that the sign-ordered phase is unstable to fluctuations for $d = 2$ (i.e., 1 spatial dimension) and stable for $d \geq 3$. We will argue below that this is indeed the case.

5.2.2 Absence of the sign-ordered phase in 2D

As a warm-up, consider the 1D equilibrium Ising model with Glauber dynamics at low temperature. Domain walls undergo random walks and annihilate when they meet. When a single spin is flipped in a uniform background, the resulting domain has probability $p_s(\tau) \sim \tau^{-1/2}$ of surviving until time τ. Over that time, the walls typically walk $w \sim \tau^{1/2}$. Thus, $\eta = \gamma = \frac{1}{2}$ and inequality (5.9) with $d - 1 = 1$ is violated. The magnetization is unstable, as expected for a finite-temperature 1D model.

In the directed path problem, there is no Hamiltonian with respect to which the sign field σ comes into equilibrium. The stochastic "dynamics" nevertheless induce survival and growth exponents. We follow [120] and consider an

[1] In $d = 1$, randomly placed single scatterers clearly disorder the sign field.

isolated negative scatterer embedded in a dense background of *disordered* positive scatterers. The path sum in the positive-scattering background reduces to the well-known directed polymer problem [129, 130]. In the extreme disordered limit, the polymer "pins" so that one path Γ_0 dominates the sum:

$$A = A_{\Gamma_0} + \cdots . \tag{5.11}$$

Accordingly, the sign $\sigma(s,t)$ is only negative if Γ_0 happens to go through the lone negative scatterer. It is known that the directed polymer wanders over a distance $w(\tau) \sim \tau^{\xi}$ with wandering exponent $\xi = \frac{2}{3}$. Thus, we identify $\eta = (d-1)\xi$ and $\gamma = \xi$. Inequality (5.9) is violated, which again implies the instability of the sign-ordered phase even at arbitrarily small x.

Since the fraction of space occupied by negative domains at time t is xt (see Eq. (5.8)), we also obtain a simple estimate for the disordering time:

$$t^*(x) \sim x^{-1}. \tag{5.12}$$

This argument clearly applies to the large-disorder limit where the path sum is dominated by a single path Γ_0. At weaker disorder in the "pinned" phase, the wandering exponent ξ governing the directed polymer is unchanged, yet subdominant paths now contribute to the path sum and interference effects may become nontrivial. Numerical investigations in Ref. [120] confirmed that the survival and growth exponents for the domains produced by isolated negative scatterers are nevertheless unchanged when the background disorder is of intermediate strength in 2D.

However, the above analysis relies on positive background disorder to produce the destabilizing fluctuations. It leaves open the possibility of 2D sign order when the disorder arises only from negative scatterers. Here we close the door by considering this regime in the limit where the typical negative domain is microscopic ($\mu \lesssim D$) and the concentration of negative scatterers $x \to 0$. We find that sign order is nonetheless destroyed by rare events.

First consider no disorder ($x = 0$). The sum Eq. (5.1) describes diffusion of paths, so that in the continuum limit,

$$\partial_t A = D\nabla_s^2 A \tag{5.13}$$

where we have rescaled A exponentially with t in order to remove an overall s-independent factor. Suppose the amplitude at $t = 0$ is roughly uniform over a region of width l. If a negative scatterer flips the sign of A in a subregion of width $w \ll l$, the negative domain becomes positive after a time $\tau \sim w^2/D$. Thus, isolated negative scatterers do not produce asymptotically long-lived negative domains.

For small but finite concentration x, a large length scale $l(x)$ emerges. Fig. 5.3 shows a typical realization of the amplitude $A(s,t)$ at late time t (we will discuss the numerical details momentarily). The log-amplitude field forms smooth "hills" separated by sharp minima. The length scale $l(x)$ is the typical distance between minima, i.e., the typical width of a hill. As in the isolated

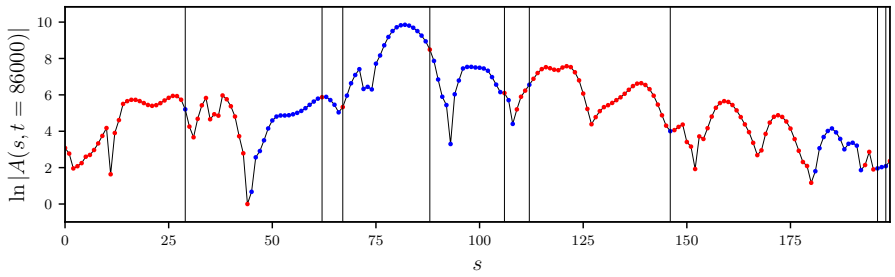

Figure 5.3: A typical snapshot of the (log-)amplitude field $\ln|A(s,t)|$, as a function of s for fixed t ($L = 200$, $x = 0.04$). The y-axis values are shifted so that the minimum is at 0. The time $t = 86000$ is close to the disordering timescale t^* for this x. Red (blue) points correspond to positive (negative) $\sigma(s,t) \equiv \mathrm{sgn}[A(s,t)]$. The vertical black lines indicate the negative scatterers at the current t, i.e., where $\alpha_{(s,t)} = -1$. All other sites have $\alpha_{(s,t)} = 1$.

case, scattering events which produce negative domains of width $w \ll l(x)$ remain short-lived ($\tau \sim w^2$). However, if a negative scattering event produces a domain covering more than half of the weight in the hill ($w \sim l(x)/2$), then it cannot disappear due to diffusion of amplitude within the hill. Such domains are locally stable and their lifetimes are governed by competition with neighboring hills over much longer timescales. Thus, $l(x)$ separates short-lived and long-lived domains.

A self-consistent argument gives the scaling of $l(x)$ as $x \to 0$. A single negative scatterer at time t_0, although it does not produce a lasting negative domain, creates a local minimum in $|A(s,t)|$. The minimum becomes wider and shallower as $\Delta t \equiv t - t_0$ increases, with the width scaling as $\Delta t^{1/2}$. After a time $\Delta t \sim l(x)^2$, the minimum merges into its neighbors and can no longer be resolved. Thus $l(x)^2$ is the "lifetime" of a local minimum. New minima are created at a rate x per unit length and time. Thus, the typical density of minima present at any given time is $\sim x l(x)^2$, but by definition, this must equal $\frac{1}{l(x)}$. We have that

$$l(x) \sim x^{-\frac{1}{3}} \tag{5.14}$$

which holds for $x \ll 1$.

Coarse-grained on the scale $l(x)$, isolated negative scatterers become effective positive-weight disorder, while the rare events which produce domains of width $l(x)$ become negative scatterers whose concentration is $x^{\alpha l(x)}$ for some $O(1)$ constant α. On this scale, the effective positive scatterers are disordered, so the analysis of Ref. [120] again applies. We recover that the sign order is unstable but with a parametrically longer timescale (cf. Eq. (5.12)),

$$t^*(x) \sim \; x^{-\alpha l(x)} \sim x^{-\alpha x^{-1/3}}, \tag{5.15}$$

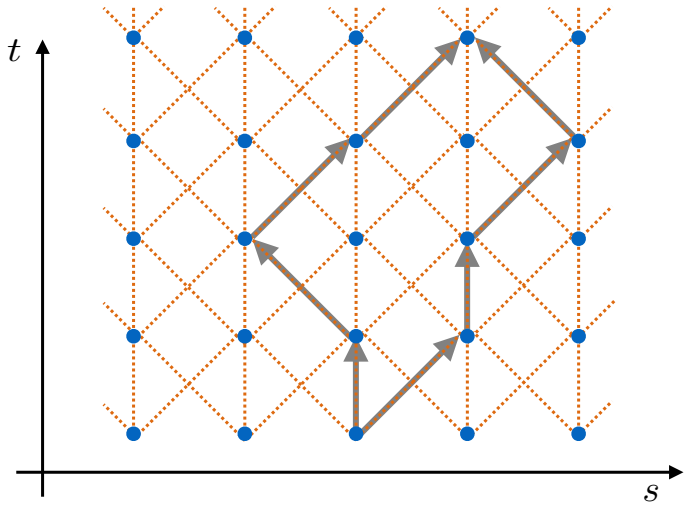

Figure 5.4: The lattice (blue dots) used in the 2D simulations. All 2D simulations begin with uniform initial conditions $A(s,0) = 1$ and propagate forward in t using Eq. (5.16). The arrows show two examples of directed paths on this lattice.

for $x \to 0$.

We now present numerical validation of these arguments. For concreteness, we use the lattice shown in Fig. 5.4. Each site (s,t) contains a scatterer with random amplitude $\alpha_{(s,t)}$, for which we take the binary distribution given by Eq. 5.3 with $M = 1$. Instead of evaluating each path amplitude A_Γ, we organize the sum over paths iteratively:

$$A(s,t+1) = \alpha_{(s,t+1)} \left(A(s-1,t) + A(s,t) + A(s+1,t) \right). \tag{5.16}$$

In all simulations in this section, we consider "quenches" from uniform initial conditions $A(s,0) = 1$ in systems with transverse width L and periodic boundary conditions.

We first determine $l(x)$ numerically by defining, at fixed time t, $l_t(x)$ to be the disorder- and spatial-averaged distance between local minima of $\ln|A(s,t)|$. Fig. 5.5 shows $l_t(x)$ as a function of t for a system of size $L = 1600$ (the curves are independent of L). Since the curves saturate at t well within the simulation time, we determine $l(x) \equiv \lim_{t\to\infty} l_t(x)$ by averaging the $l_t(x)$ over their plateaux. The scaling behavior of the resulting $l(x)$ with x, shown in Fig. 5.5b, confirms Eq. 5.14.

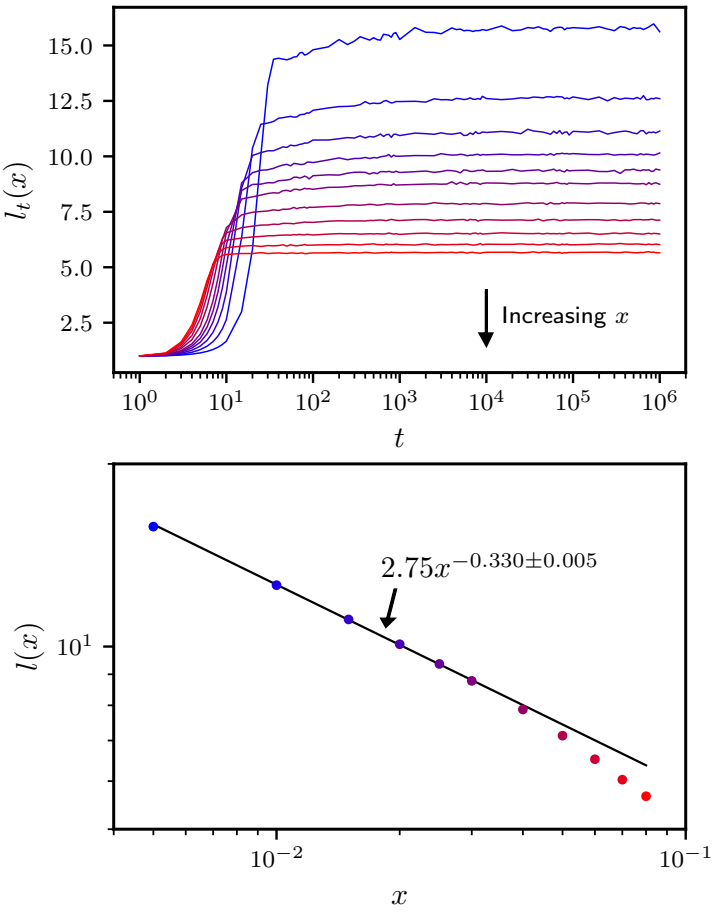

Figure 5.5: (Top) Mean distance between local minima of the height field at time t, averaged over disorder ($L = 1600$). Each line (color) corresponds to a different density of scatterers x. Errorbars (not shown for clarity) are of the same magnitude as the fluctuations within each curve. (Bottom) Asymptotic distance $l(x)$ between minima, taken from the average of the late-time plateaux of $l_t(x)$. The color of each point indicates which curve in the top panel it corresponds to. Errorbars are smaller than the marker size. The solid line is a power-law fit of the points with $x \in [0.01, 0.03]$.

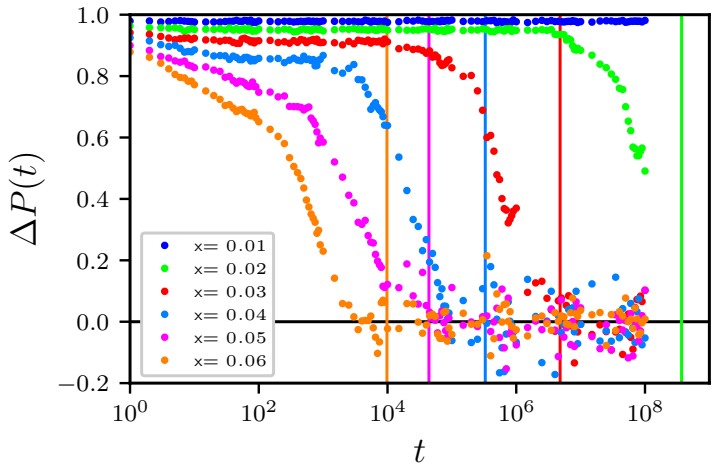

Figure 5.6: Decay of the sign order parameter $\Delta P(t) \equiv \mathbb{E}\left[\frac{1}{L}\sum_s \sigma(s,t)\right]$ in 2D from uniform initial conditions (transverse size $L = 100$). Errorbars (not shown) are of the same magnitude as the fluctuations within a curve. The vertical lines correspond to the independently determined disordering timescales $t^*(x)$ for each density of negative scatterers x, see Eq. (5.15). The predicted $t^*(x = 0.01) \approx 10^{12}$ is not accessible with current computing resources.

We have also verified Eq. (5.15) for the disordering time. Fig. 5.6 shows

$$\Delta P(t) \equiv \mathbb{E}\left[\frac{1}{L}\sum_s \sigma(s,t)\right] \tag{5.17}$$

as a function of t, for various small x. For all $x \geq 0.02$, the sign field clearly disorders at large t. The vertical lines are the independent estimates $t^*(x) = x^{-\alpha l(x)}$, with $\alpha = \frac{1}{2}$ and $l(x)$ determined numerically as described above. The agreement with the observed disordering times is excellent considering that $t^*(x)$ ranges over ~ 5 orders of magnitude as x varies. This also explains why past numerical work on the 2D sign phase transition was inconclusive: the simulation must run for very long times to see disordering. Indeed, we estimate that the disordering time for $x = 0.01$ is $\sim 10^{12}$, which is longer than we can study numerically.

We note that within our analysis, α is the only free fitting parameter. $\alpha = \frac{1}{2}$ gives an excellent fit and has a simple physical rationale: only half of a hill must change sign simultaneously, for then the new domain occupies the majority of the hill and annihilates the remainder.

5.2.3 The sign phase transition in 3D

There are several suggestive but contradictory arguments regarding the sign-ordered phase in 3D. The analogy with the $(d-1)$-dimensional stochastic Ising model (see Sec. 5.2.1) suggests that the sign-ordered phase can exist, since Ising order is stable in two spatial dimensions. On the other hand, disorder always drives the (positive-weight) directed polymer into its "pinned" phase in 3D [130], just as in 2D. In the strongly pinned limit where A is dominated by a single path, this would lead to sign disorder by the arguments of Sec. 5.2.2 and Ref. [120]. However, this does not rule out the possibility of a stable sign-ordered phase at weaker disorder. Here, we present a numerical study in the weak disorder regime analogous to that studied in 2D above. By several complimentary numerical simulations and finite-size scaling analyses, we conclude that 3D sign order exists.

We calculate path sums on the cubic lattice defined by the recursion relation

$$\begin{aligned} A(s_1, s_2, t+1) = \alpha_{(s_1,s_2,t+1)} \Big(& A(s_1, s_2, t) \\ & + A(s_1 - 1, s_2, t) + A(s_1 + 1, s_2, t) \\ & + A(s_1, s_2 - 1, t) + A(s_1, s_2 + 1, t) \Big), \end{aligned} \tag{5.18}$$

with periodic boundary conditions for systems of transverse size L x L.

Fig. 5.7 shows the decay of $\Delta P(t)$ starting from uniform initial conditions. It suggests that the sign field becomes disordered when $x \gtrsim 0.16$ but remains ordered when $x \lesssim 0.16$. However, we face the same difficulty as in 2D (cf. Fig. 5.6): $\Delta P(t)$ may remain non-zero throughout the accessible simulation but disorder on longer timescales. The values of ΔP as a function of x plotted in the bottom panel of Fig. 5.7 are only upper bounds to the true $t \to \infty$ values.

To confirm that the sign-ordered phase is in fact stable at small x, we consider "quench" experiments from *disordered* initial conditions: $A(s_1, s_2, 0) = \pm 1$ with equal probability. If the sign order is stable, we expect the sign field to order spontaneously for $x < x_c$. This is in analogy to the 2D Ising model, which magnetizes spontaneously when quenched from high temperature to below T_c. Fig. 5.8 demonstrates this ordering for two representative concentrations x. Note that because of the symmetry in the initial conditions, we consider the order parameter

$$\Delta P_2(t) \equiv \sqrt{\mathbb{E}\left[\left(\frac{1}{L^2} \sum_{s_1,s_2} \sigma(s_1, s_2, t) \right)^2 \right]}. \tag{5.19}$$

At $x = 0.08$, well below the tentative x_c identified above, $\Delta P_2(t)$ approaches a constant value independent of L as $t \to \infty$. The timescale to reach the asymptotic value scales as L^2 (not shown), which is the same scaling as that of coarsening dynamics in the 2D Ising model [131]. At $x = 0.17$, in contrast, $\lim_{t\to\infty} \Delta P_2(t)$ decreases as the system size increases, consistent with lack of long-range order.

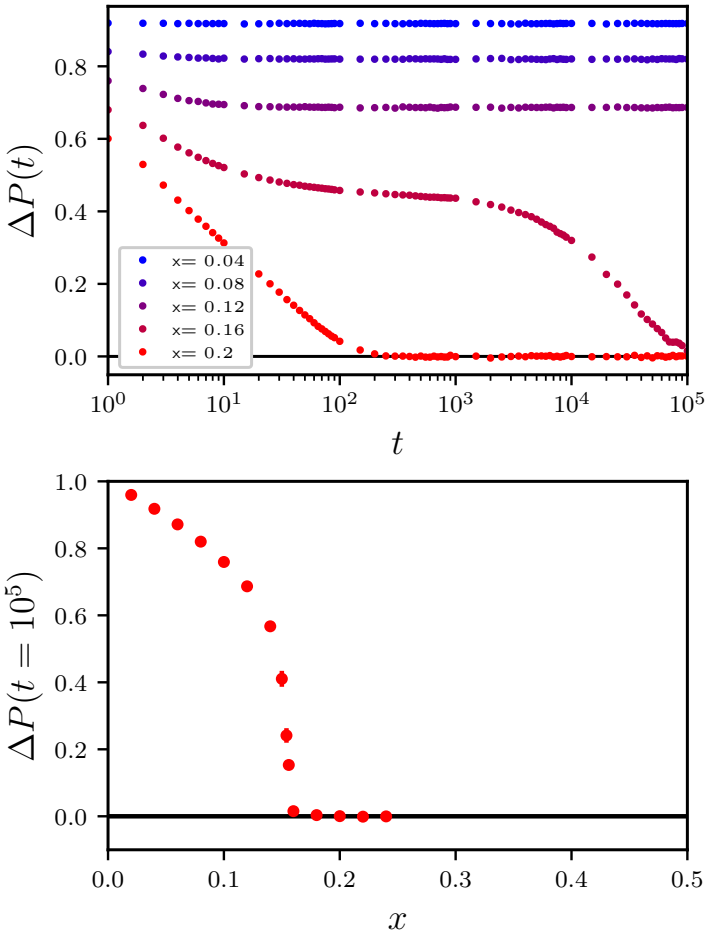

Figure 5.7: Decay of sign order in 3D from uniform initial conditions on the lattice of Eq. (5.18). (Top) The sign order parameter $\Delta P(t)$ as a function of t for various x at size $L = 80$. Errorbars are smaller than the marker size. (Bottom) ΔP evaluated at time $t = 10^5$ as a function of x. The sharpness of the crossover is suggestive of a transition at $x_c \approx 0.16$.

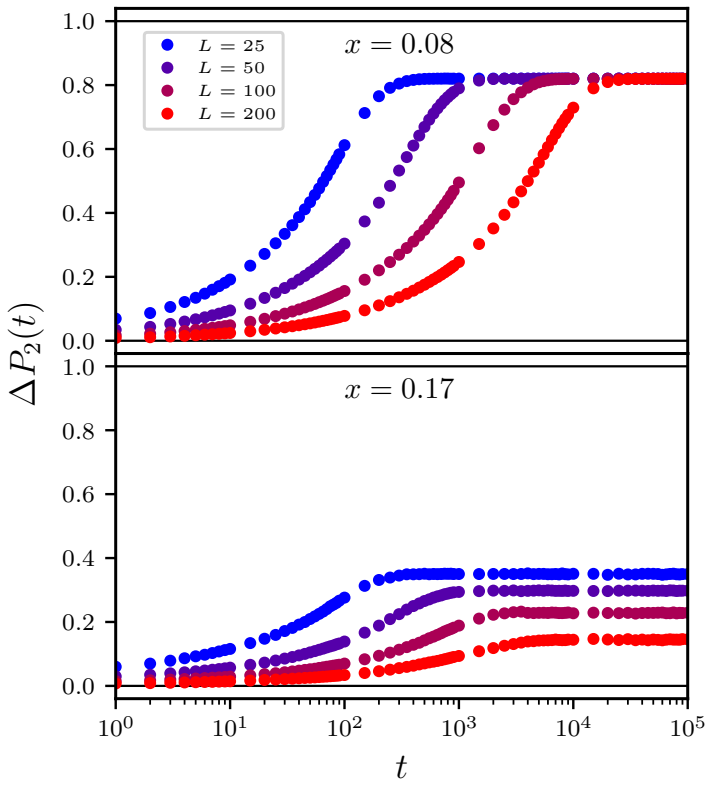

Figure 5.8: Spontaneous ordering of the sign field starting from disordered initial conditions, as shown by $\Delta P_2(t)$ (Eq. (5.19)) for various L. Errorbars are smaller than the marker size. (Top) For $x = 0.08$, the late-time value of $\Delta P_2(t)$ becomes independent of system size L, consistent with spontaneous long-range order. (Bottom) For $x = 0.17$, the late-time value of $\Delta P_2(t)$ decays with increasing system size.

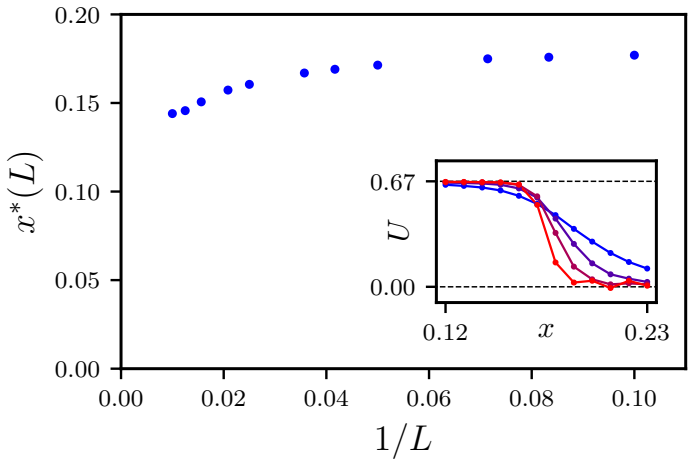

Figure 5.9: Convergence of the Binder cumulant crossing points to the location of the sign phase transition (at $t = 10^5$). $x^*(L)$ is the point at which the size-L and size-$2L$ cumulant curves cross, and the $1/L \to 0$ limit is the thermodynamic value x_c for the transition. Errorbars are imperceptible on this scale. (Inset) Representative cumulant curves for small systems (blue to red: $L = 10, 20, 40, 80$), together with the ordered and disordered limiting values of $2/3$ and 0.

These two complementary simulations, respectively observing the decay of ordered sign fields and the spontaneous ordering of disordered ones, together suggest that the sign field remains ordered at small x and only disorders at larger x. To quantitatively extract the critical x_c, we have carried out a crossing-point analysis of the Binder cumulant obtained from the uniform-initial-condition simulations. The sign Binder cumulant

$$U(t) \equiv 1 - \frac{\mathbb{E}\left[\left(\frac{1}{L^2}\sum_{s_1,s_2}\sigma(s_1,s_2,t)\right)^4\right]}{3\,\mathbb{E}\left[\left(\frac{1}{L^2}\sum_{s_1,s_2}\sigma(s_1,s_2,t)\right)^2\right]^2} \tag{5.20}$$

provides a dimensionless measure of the ordering transition in the sign field [132]. In a Gaussian ordered phase, $U = 2/3$ while in a disordered phase, $U = 0$. The Binder cumulant is especially useful for extracting x_c by the crossing point method described below because it has very small finite-size corrections [133].

The inset to Fig. 5.9 shows representative data for the Binder cumulant U computed at the longest times accessible to our simulations ($t_{\max} = 10^5$) as a function of x at several system sizes. At a given size L, U crosses over from its ordered value at small x to the disordered value at large x. There is significant finite size drift of the crossing points between consecutive system sizes L. The

main panel of Fig. 5.9 shows the crossing point $x^*(L)$ for the size-L and size-$2L$ curves as a function of $1/L$. We determine the crossing points by fitting the (x, U) data for each L to a second-order polynomial near the tentative location. Without further assumptions regarding the finite-size scaling of the transition, we cannot make a quantitatively accurate estimate of $x_c = \lim_{L\to\infty} x^*(L)$, but the data in Fig. 5.9 appear consistent with $x_c \approx 0.14$.

To summarize, at small x in 3D, the sign field orders spontaneously at long times even when initialized with a disordered configuration. At large x, on the other hand, the sign field disorders even when starting from an ordered configuration. As we increase the system size, the Binder cumulant of the sign field flows to the ordered limit at small x and the disordered limit at large x, and a crossing-point analysis shows that the transition persists into the thermodynamic limit.

These numerical results are robust but limited by finite computational resources. Moreover, we note that sign order is in some tension with the established marginal flow of the 3D *positive*-weight directed polymer to the pinned phase at arbitrarily small disorder. We speculate that there are three possible renormalization group scenarios for sign order in 3D:

- Sign order is consistent with pinned-phase fluctuations of the $\ln|A|$ field because of interference from subdominant paths.
- Negative amplitudes stabilize the Gaussian phase of the directed polymer in 3D and the sign-ordered phase coincides.
- Sign order is ultimately unstable in 3D due to the fluctuations in the strongly pinned phase. As the flow to strong pinning is only marginal, the disordering timescales are too long to be observable.

It would be very interesting to conclusively establish which of these scenarios holds and develop a theory of the associated fixed points.

5.3 Discussion

Our results have physical consequences for a variety of systems, which we now describe.

5.3.1 Magnetoresistance of variable-range hopping

In the variable range hopping regime of disordered semiconductors, electrons tunnel further than the typical distance between localized states [37, 134]. In this case, A in Eq. (5.1) is the electron tunneling amplitude given as a sum of partial amplitudes corresponding to different tunneling paths Γ [112, 122–126, 128]. In the presence of a magnetic field, each amplitude acquires a factor $\exp\left(i\frac{\Phi_\Gamma}{\Phi_0}\right)$, where $\Phi_\Gamma = BS_\Gamma$ is the flux enclosed between Γ and some fixed reference path, and Φ_0 is the flux quantum (see Fig. 5.1). It has been argued that the magnetoresistance is positive in the sign-ordered phase and negative in

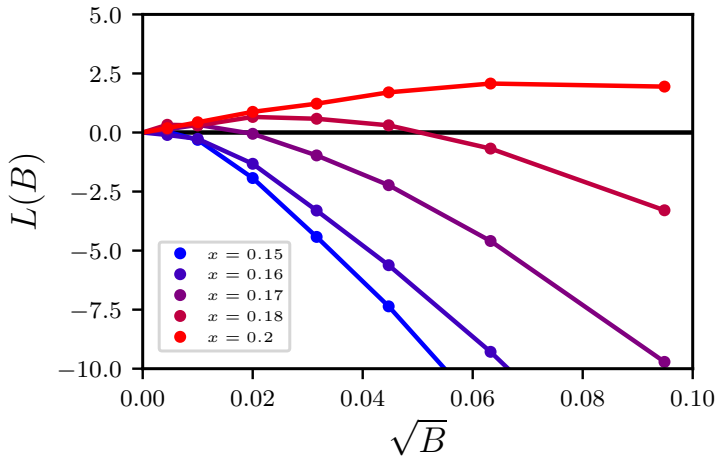

Figure 5.10: Proxy for the 3D magnetoresistance $L(B)$ (see Eq. (5.23)) as a function of the applied magnetic field B, for various x (system size $L = 1000$ and length $t = 1000$). Errorbars are smaller than the marker size, and the solid lines are guides to the eye.

the sign-disordered phase [127]. Thus, our results imply that in 2D systems at sufficiently small magnetic fields and low temperature, the magnetoresistance is always negative. In contrast, in 3D systems, the manetoresistance should change sign as a function of the concentration of negative scatterers x.

We have calculated the magnetoresponse for a 3D system with the lattice of Eq. (5.18). In the magnetic field corresponding to vector potential $\mathbf{A}(\mathbf{r})$, a hop from $\mathbf{r}_0$ to $\mathbf{r}_0 + \mathbf{b}$ acquires the phase $\frac{q}{\hbar}\int_{\mathbf{r}_0}^{\mathbf{r}_0+\mathbf{b}} \mathrm{d}\mathbf{r}\cdot\mathbf{A}(\mathbf{r})$, where q is the charge of the particle. That is,

$$\begin{aligned} &A(\mathbf{r}_0+\mathbf{b}) = \alpha_{\mathbf{r}_0+\mathbf{b}} A(\mathbf{r}_0) + \cdots \\ &\rightarrow A(\mathbf{r}_0+\mathbf{b}) = \alpha_{\mathbf{r}_0+\mathbf{b}} e^{i\frac{q}{\hbar}\int_{\mathbf{r}_0}^{\mathbf{r}_0+\mathbf{b}} \mathrm{d}\mathbf{r}\cdot\mathbf{A}(\mathbf{r})} A(\mathbf{r}_0) + \cdots . \end{aligned} \tag{5.21}$$

We set $q = \hbar = 1$ henceforth. To apply a field $\mathbf{B}(s_1, s_2, t) = B\hat{\mathbf{s}}_2$ to the cubic lattice, we choose vector potential $\mathbf{A}(s_1, s_2, t) = -Bt\,\hat{\mathbf{s}}_1$ (using the orientation $\hat{\mathbf{s}}_1 \times \hat{\mathbf{t}} = \hat{\mathbf{s}}_2$). The recursion relation becomes

$$\begin{aligned} A(s_1, s_2, t+1) = \alpha_{(s_1,s_2,t+1)}\Big(&A(s_1, s_2, t) + e^{-i\left(t+\frac{1}{2}\right)B} A(s_1-1, s_2, t) \\ &+ e^{i\left(t+\frac{1}{2}\right)B} A(s_1+1, s_2, t) + A(s_1, s_2-1, t) + A(s_1, s_2+1, t)\Big). \end{aligned} \tag{5.22}$$

The resulting magnetoresponse is illustrated in Fig. 5.10. We plot the quantity

$$L(B) \equiv \ln\left|\frac{A_B(0,t)}{A_0(0,t)}\right|^2, \tag{5.23}$$

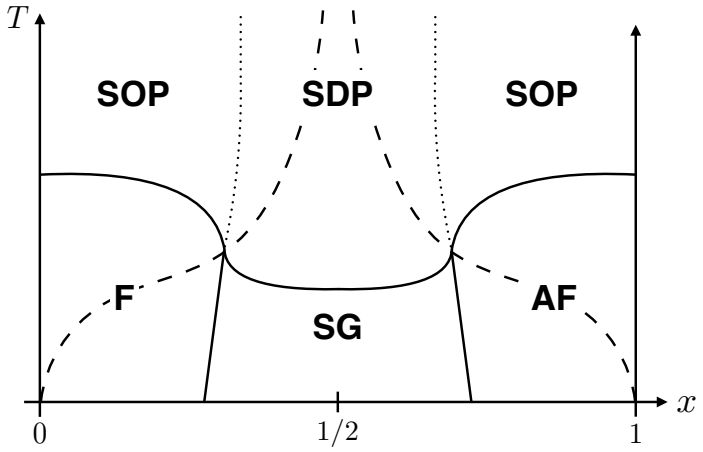

Figure 5.11: Schematic phase diagram of 3D $\pm J$ spin glass on a bipartite lattice. The sign-ordered paramagnet (SOP) and sign-disordered paramagnet (SDP) are separated by the sign phase transition (dotted line). The high temperature expansion implies a finite asymptotic x_c for this line at large temperature; its terminus at the multicritical point is conjectural. The low temperature ferromagnetic (F), antiferromagnetic (AF) and spin glass (SG) phases are separated by solid lines. For the $\pm J$ model, the Nishimori line is indicated by the dashed line. Boundaries capture topology of the phase diagram but are not drawn quantitatively accurately.

for a fixed large value of t. $A_B(s,t)$ is the path sum in the presence of a magnetic field B (see Appendix for details). $L(B) \sim t\Delta\xi/\xi^2$ measures the relative change $\Delta\xi = \xi(B) - \xi(0)$ in the effective localization length which enters into the hopping conductivity. $L(B) > 0$ indicates negative and $L(B) < 0$ indicates positive magnetoresistance (see Ref. [127] for details). The magnetoresistance at small B indeed changes sign as a function of x at x_c in agreement with our estimate of the sign phase boundary.

5.3.2 3D spin glass phase diagram

Consider a spin glass described by the Hamiltonian

$$H = \sum_{ij} J_{ij} S_i S_j, \tag{5.24}$$

where the S_i are spins (Ising, Heisenberg, etc.), and the exchange energies J_{ij} are random. For 3D spin glasses with $\Pr[J_{ij} > 0] = 1 - x$ and $\Pr[J_{ij} < 0] = x$, the existence of the sign phase transition implies new features of the phase diagram. This is qualitatively shown in Fig. 5.11 for the case of a bipartite (e.g. cubic) lattice.

The three low-temperature phases (ferromagnetic, spin-glass, and antiferromagnetic) are well-established, both for Ising and Heisenberg spins [135–140]. At high temperature $T \gg J_{ij}$, the system is paramagnetic. The high-temperature expansion for the spin correlation function,

$$\langle S_i S_f \rangle = \mathrm{Tr}\left[S_i S_f \frac{\exp\left(-\beta H\right)}{Z} \right], \tag{5.25}$$

can be expressed as a sum over interfering directed paths of the form Eq. (5.1). Thus, there is a sign phase transition in the statistical properties of $\langle S_i S_f \rangle$ at long distance. This is indicated by the dotted lines at high temperature in Fig. 5.11. Note that the line at $x > \frac{1}{2}$, corresponding to mainly antiferromagnetic bonds, is a transition in the Néel correlator $(-1)^{|i-f|} \langle S_i S_f \rangle$.

Sign order or disorder in the spin correlation function is well-defined at any temperature, not only high temperatures where a directed-path expansion holds. Furthermore, the sign phase transition divides phases with different symmetries in their correlators. Thus although we have only demonstrated the existence of the transition at high temperature, the boundary cannot terminate in the middle of the phase diagram and must persist to lower temperatures. We conjecture that it meets the triple point of the thermodynamic phases. In that sense, it is a continuation of the boundary separating the low temperature ferromagnetic and spin-glass phases. Keep in mind that all thermodynamic properties of the system are analytic across the sign phase transition. However, the sign phase transition may nevertheless be relevant for the thermodynamics and dynamics of spin glasses, particularly at lower temperatures near the triple point (cf. the "Widom line" that extends well beyond the critical point in classical fluids [141, 142]).

For the $\pm J$ model, the well-known Nishimori line [143] also intercepts the multicritical point in Fig. 5.11. The Nishimori line approaches $x = \frac{1}{2}$ as $T \to \infty$, thus it lies in the sign-disordered phase at high temperature. We conjecture that $\langle S_i S_f \rangle$ is sign-disordered throughout the entire paramagnetic portion of the Nishimori line, as sketched in Fig. 5.11. This is consistent with the identity

$$\mathbb{E}\left[\langle S_i S_f \rangle\right] = \mathbb{E}\left[\langle S_i S_f \rangle^2\right]. \tag{5.26}$$

which holds everywhere along the Nishimori line. In particular, in the paramagnetic phase, $\mathbb{E}\left[\langle S_i S_f \rangle\right]$ decays exponentially with distance so $\mathbb{E}\left[\langle S_i S_f \rangle\right] \ll 1$ for long-enough paths. The Nishimori identity Eq. (5.26) then implies

$$\mathrm{Var}\left[\langle S_i S_f \rangle\right] \sim \mathbb{E}\left[\langle S_i S_f \rangle\right] \gg \mathbb{E}\left[\langle S_i S_f \rangle\right]^2, \tag{5.27}$$

i.e., the relative fluctuations of $\langle S_i S_f \rangle$ diverge at large distance as expected in the sign-disordered phase.

In 2D, the phase diagram is much simpler (not shown). While the ferromagnetic phases still exist, there is no finite temperature spin glass. Similarly, our results show that there is no high temperature sign-ordered phase and thus no equivalent of the dotted line in the 3D phase diagram.

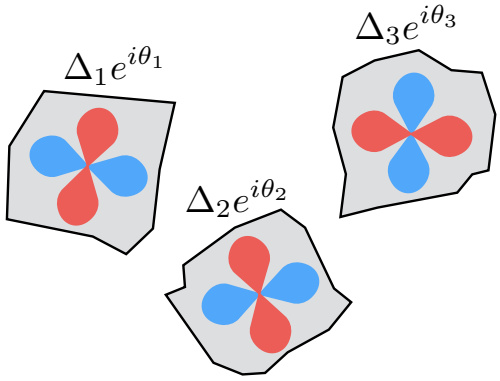

Figure 5.12: Sketch of D-wave superconducting grains embedded in a non-superconducting medium. The lobes on each grain reflect the random alignment of the D-wave order parameter $\Delta(\mathbf{k})e^{i\theta}$.

5.3.3 Composite D-wave superconductors

The existence of sign-ordered and -disordered phases manifests in properties of random composite D-wave superconductors, where superconducting grains are embedded into a metallic matrix (see Fig. 5.12). In the regime where the grain size is larger than the coherence length and the temperature is below the bulk T_c, fluctuations in the magnitude of the superconducting order parameter can be neglected. The superconducting phases θ_i on each grain are then described by the Josephson Hamiltonian,

$$H_d = \sum_{ij} J_{ij} \cos\left(\theta_i - \theta_j + \frac{2e}{c}\int_{\mathbf{r}_i}^{\mathbf{r}_j} \mathrm{d}\mathbf{r}\cdot\mathbf{A}(\mathbf{r})\right), \tag{5.28}$$

where $\mathbf{A}(\mathbf{r})$ is the vector potential. In D-wave systems with no applied field ($\mathbf{A}(\mathbf{r}) = 0$), the effective Josephson couplings J_{ij} may have random signs which depend on the separation and orientation of the embedded grains. For further details, see the discussion in [110].

The expansion of the correlation function $\chi = \langle \exp\left(i(\theta_i - \theta_j)\right)\rangle$ at high temperature reduces to Eq. (5.1), and the system can exhibit a sign phase transition as a function of the concentration of negative J_{ij}. On application of a magnetic field, this correlation function *increases* in the sign-disordered phase just like the negative magnetoresistance in hopping conductivity. This manifests as a general magnetic-field enhancement of the superconductivity.

Chapter 6

Magnetoenhancement of superconductivity in composite D-wave superconductors

In this chapter, we study composite D-wave superconductors consisting of randomly distributed and randomly oriented superconducting droplets embedded into a matrix. We show that the application of a small magnetic field can enhance superconductivity in these materials. This result was hinted at in Chap. 5. Here, we explore the phenomenon further under a wider range of conditions. The work is published in Ref. [144].

6.1 Background and model

In general, the superconducting order parameter is a function of two coordinates and two spin indices $\Delta_{\alpha,\beta}(\mathbf{r},\mathbf{r}')$. Conventional low-$T_c$ superconductors have a singlet order parameter with S-wave symmetry which can be described by a complex field $\Delta_s(\mathbf{r}) \equiv \Delta(\mathbf{r},\mathbf{r})$. Qualitatively, this describes the Bose condensation of Cooper pairs into a zero orbital momentum state. The propagation amplitude of a Cooper pair between two spatial points can be written as a sum of positive partial amplitudes corresponding to different Feynman paths. In the presence of a magnetic field, these amplitudes acquire phases and partially cancel one another. As a result, S-wave superconductivity is suppressed by the magnetic field. This qualitative picture is consistent with the corresponding solution of the Gorkov equations [145].

Over the last decades a number of superconductors have been discovered in which the order parameter changes sign under rotation. The primary examples are the high-T_c superconductors where the order parameter has singlet D-wave

symmetry (see, e.g., [146, 147]): $\Delta(\mathbf{r}, \mathbf{r}')$ changes sign under rotation by $\pi/2$, and consequently $\Delta(\mathbf{r}, \mathbf{r}) = 0$. This means that the Fourier transform $\Delta(\mathbf{k})$ changes sign under a $\pi/2$ rotation as well, as is shown schematically in Fig. 6.1. Still, the solution of the Gorkov equation in crystalline materials demonstrates that the application of a magnetic field suppresses superconductivity.

We shall study the magnetic properties of a composite of randomly shaped and randomly oriented D-wave superconducting grains embedded in a metallic matrix (see Fig. 6.1). In such systems, the nodes of the order parameter $\Delta(\mathbf{k})$ are locked to the crystalline axes of each grain. It is known that the macroscopic properties of such granular materials are distinct from both S- and D-wave superconductors [110,111,148]. Below we show that the application of a magnetic field enhances the superfluid stiffness N_s and the critical temperature T_c of such materials in certain parameter regimes.

Granular composites are characterized by the following lengths: the typical superconducting grain size R, the inter-grain distance r_G, the elastic electron mean free path in the metal l, the zero-temperature coherence length of the bulk superconductor ξ_0, and the coherence length of the normal metal $L_T = \sqrt{D/T}$. Here, $D \equiv l v_F/3$ is the diffusion coefficient, where v_F is the Fermi velocity in the metal.

In the regime where $R, r_G > \xi_0$, and the temperature $T \ll T_c^b$ is smaller than the critical temperature of the bulk superconductor, one can neglect the fluctuations of the modulus of the order parameter and reduce the Hamiltonian to that of a system of Josephson junctions,

$$H = \frac{\hbar}{2e} \Re \sum_{i \neq j} J_{ij} e^{i(\theta_i - \theta_j)}. \tag{6.1}$$

Here, J_{ij} is the Josephson coupling between grains i and j, and θ_i is the phase of the order parameter in the i-th grain. $\Re$ denotes taking the real part. Generally, J_{ij} is a complex number. However, in the absence of a magnetic field we may take all J_{ij} to be real (but not necessarily positive).

Since in random media all spatial symmetries are broken, the anomalous Green function $F(\mathbf{r}, \mathbf{r}')$ is an admixture of S, D and higher angular momentum components of the spin singlet state. In the metallic matrix, at distances from the nearest grain greater than l, only the singlet component survives. Thus, in the simplest case where the inter-grain distance $r_G \gg l$, the singlet component controls the value of the Josephson couplings J_{ij}.

In this diffusive regime and within the mean-field approximation, the S-components of the normal G and anomalous F Green functions satisfy the Usadel equation [149],

$$\begin{gathered} \epsilon F_\epsilon - \frac{D}{2} \hat{\nabla} \left(G_\epsilon \hat{\nabla} F_\epsilon - F_\epsilon \nabla G_\epsilon \right) = 0, \\ G_\epsilon^2 + |F_\epsilon|^2 = 1, \end{gathered} \tag{6.2}$$

where $\hat{\nabla} = \nabla + 2ei\mathbf{A}$ is the covariant derivative, $\mathbf{A}$ is the vector potential,

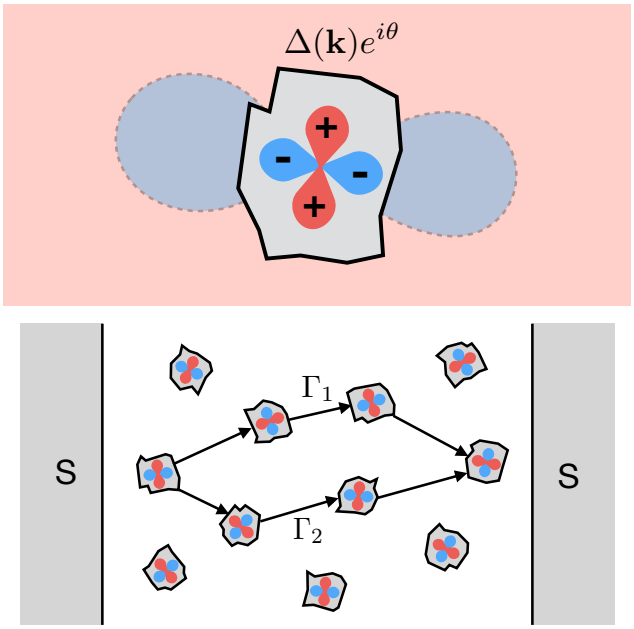

Figure 6.1: (Top) Pictorial representation of a D-wave superconducting grain and its normal-metallic environment. The grain, colored grey, hosts a non-zero order parameter having the form indicated above the grain. The wavevector dependence of the order parameter is represented by the red-and-blue rosette on the grain: red corresponds to $\Delta(\mathbf{k}) > 0$ and blue to $\Delta(\mathbf{k}) < 0$. The shading outside the grain represents the sign of the anomalous Green function produced by the proximity effect: red is again positive and blue negative. (Bottom) A granular D-wave superconductor sandwiched between two homogenous S-wave superconductors, shaded grey. Each individual grain has a randomly oriented order parameter owing to the random orientation of its crystalline axes. Γ_1 and Γ_2 indicate two directed paths across the granular system.

and $F_\epsilon(\mathbf{r})$ and $G_\epsilon(\mathbf{r})$ are Fourier transforms of the Matsubara Green functions $F(\mathbf{r},\mathbf{r},t-t')$ and $G(\mathbf{r},\mathbf{r},t-t')$.

In the case where $T \ll T_c^b$, the size of the grain is larger than ξ_0, and the Andreev reflection from its boundary is effective, the boundary conditions for Eq. (6.2) at the D-N boundary have been derived in Ref. [150]. The relevant energy for computing the Josephson coupling, $\epsilon \sim D/r_G^2$, is much smaller than the value of the order parameter in the puddles. Thus the boundary condition for $F_\epsilon(\mathbf{r})$ is independent of ϵ and depends only on the angle between the unit vectors $\mathbf{n}_\Delta$ and $\mathbf{n}(\mathbf{r})$, where $\mathbf{n}_\Delta$ is parallel to the direction of a gap node and $\mathbf{n}(\mathbf{r})$ is normal to the boundary at the point $\mathbf{r}$ on the surface. We write the boundary condition as $F_\epsilon(\mathbf{r}) = f[(\mathbf{n}_\Delta \cdot \mathbf{n}(\mathbf{r}))^2]$. Here $f(x)$ is a smooth function, which grows from $f(0) = 0$ to $f(1) \sim 1$.

In the absence of magnetic field $\mathbf{H}$, a typical spatial distribution of the solution of Eq. (6.2) for the anomalous Green function $F_{\epsilon\to 0}(\mathbf{r})$ due to an isolated grain is shown in Fig. 6.1. Red and blue colors are used to indicate the regions where $F_{\epsilon\to 0}(\mathbf{r})$ has positive and negative signs, respectively. The lines where $F = 0$ will be of particular interest to us.

At $\mathbf{H} = 0$, the phase diagram of the system of D-wave droplets embedded into a metal was studied in Refs. [110, 111, 148]. It has been shown that in the case where the droplets are randomly oriented, the Josephson couplings J_{ij} in Eq. 6.1 are real quantities which can be decomposed as

$$J_{ij} = \eta_i \eta_j I_{ij}^{(0)} + \eta_{ij} I_{ij}^{(1)} \tag{6.3}$$

Here

$$\eta_i = \mathrm{sgn}\ \left[\int_{s_i} F(\mathbf{r}) d\mathbf{r}\right] = \pm 1 \tag{6.4}$$

with the integral taken over the surface s_i of grain i, and the η_{ij} are random signs. The positive quantities $I_{ij}^{(0),(1)}$ are randomly distributed on the scales

$$I_{ij}^{(0)} \propto \frac{GD}{R^2}\frac{R^d}{r_{ij}^d} e^{-r_{ij}/L_T}, \qquad I_{ij}^{(1)} \propto \frac{R^2}{r_{ij}^2} I_{ij}^{(0)}, \tag{6.5}$$

where G is the conductance of a block of the metal of linear size R. Note that the two terms in Eq. (6.3) have different character. The first has its sign determined by a product of quantities that depend on the properties of each grain separately, roughly related to the shape of the grains. Conversely, the sign of the second term is determined by a joint property of the pair of grains i and j (related to the relative orientation of their crystalline axes). At large grain concentrations, where typically $I^{(0)} \ll I^{(1)}$, this problem is a version of the standard model of an XY spin glass [106], while in the opposite limit, the system reduces to the well-known Mattis model [151].

In the presence of a magnetic field the Josephson couplings J_{ij} in Eq. (6.1) become complex. We can generally represent the Josephson coupling at finite H by

$$J_{ij}(\mathbf{H}) = \pm e^{i\zeta_{ij}} \big| A_{ij} - B_{ij} e^{i\chi_{ij}} \big| I_{ij}. \tag{6.6}$$

This equation expresses J_{ij} as a coherent sum of probability amplitudes to transfer Cooper pairs between grains i and j. A_{ij} and B_{ij} are appropriately normalized sums of the positive and negative diffusive amplitudes in the absence of the magnetic field. The choice of sign in Eq. (6.6) is fixed by the sign of J_{ij} at $H = 0$. We separate two phase factors: the average phase $\zeta_{ij} = \mathbf{A}(\mathbf{r}) \cdot \mathbf{r}_{ij}$, where $\mathbf{r}_{ij}$ is a vector connecting the centers of grains i and j, and the relative phase $\chi_{ij} = HS_{ij}/\Phi_0$ between the positive and negative path amplitudes. Here, Φ_0 is the flux quantum and S_{ij} is the area associated with the diffusion paths. Finally, the overall scale I_{ij} depends on r_{ij}/R. It maps onto $I_{ij}^{(0)}$ from Eq. (6.3) in the limit $r_{ij} \gg R$ and onto $I_{ij}^{(1)}$ in the limit $r_{ij} \ll R$.

We will show that the magnetic field corrections to physical quantities of the system associated with Eq. (6.6) are asymptotically larger than H^2 for small $\mathbf{H}$. This is the reason why we neglect the quadratic-in-$\mathbf{H}$ suppression of A_{ij} and B_{ij} in Eq. (6.6).

The value of the area S_{ij} in Eq. (6.6) is also random. Its characteristic value S is not universal. For example, if the diffusion coefficient in the metal in Eq. (6.2) does not exhibit spatial fluctuations, $S \sim R^2$.

6.2 Magnetoenhancement in the Mattis regime

6.2.1 Enhancement in one dimension

To illustrate the physical origin of the magnetic field enhancement of superconductivity, let us first consider a quasi-one-dimensional case where the droplets are embedded into a metallic wire. In the absence of a magnetic field, the ground state of the system corresponds to $\theta_{i+1} = \theta_i$ if $J_{i,i+1} > 0$, and $\theta_{i+1} = \theta_i + \pi$ if $J_{i,i+1} < 0$. The superfluid stiffness N_s is defined by the usual equation

$$\langle \mathbf{j} \rangle = N_s \nabla \theta, \tag{6.7}$$

with $\langle \mathbf{j} \rangle$ the current density coarse-grained over a macroscopic scale. To calculate N_s, we expand Eq. (6.1) up to quadratic terms in $\theta_i - \theta_j$ near the ground state. As a result, we get the expression

$$\begin{aligned} \mathbb{E}\big[N_s(H)\big] &= \lim_{L\to\infty} \mathbb{E}\left[L \left(\sum_i \frac{1}{|J_{i,i+1}|} \right)^{-1} \right] \\ &= r_G \left(\int \frac{p(|J|)}{|J|} d|J| \right)^{-1} \end{aligned} \tag{6.8}$$

where the sum is taken over neighboring grains, L is the length of the wire, and $\mathbb{E}[\,\cdot\,]$ denotes averaging over the random distribution of J_{ij} .

At $H = 0$, the probability density $p(|J_{ij}|)$ for the random quantity $|J_{ij}|$ is finite at $|J_{ij}| = 0$. As a result the integral in Eq. (6.8) diverges logarithmically and the superfluid stiffness is 0. Physically, this follows from the presence of arbitrarily weak links in the long wire.

At $H \neq 0$, the cancellations which produce small $|J_{ij}|$ are less effective because they must cancel in the complex plane. The upshot is that $p(|J_{ij}|) = 0$ at $J_{ij} = 0$ when H is finite. This cuts off the logarithmic divergence in Eq. (6.8) and we obtain

$$\langle N_s(H) \rangle \sim \frac{N_s^{(0)}}{|\log(\phi^2)|}. \tag{6.9}$$

where $N_s^{(0)} = \mathbb{E}[|J_{ij}|]$ and $\phi \equiv HS/\Phi_0$ is a dimensionless measure of the characteristic flux between grains. According to Eq. (6.9), the magnetic field enhancement of the superfluid density is non-analytic, which justifies our neglect of the quadratic-in-H corrections to J_{ij}. Physically, the magnetic field suppresses the density of weak links in the long wire.

In higher dimensions, the disordered D-wave composite superconductor can be frustrated and form a superconducting glass. This complicates the theoretical analysis. Below we discuss several cases where we can nonetheless demonstrate the magnetoenhancement of superconductivity. We find that the enhancement is linear in $|H|$ in $d \geq 2$ and thus we neglect all quadratic and higher-order contributions.

6.2.2 Superfluid stiffness

If the typical intergrain distance is larger than their size and the normal metal coherence length, i.e., $r_G \gg R, L_T$, the second term in Eq. (6.3) can be neglected. In the absence of a magnetic field, the Hamiltonian in Eq. (6.1) reduces to a Mattis model, for which the random factors η_i can be gauged out [110, 111, 148]. Accordingly, in Eq. (6.6) we may take the $\pm$ sign to be always positive.

In this regime, the phases $\chi_{ij}(H)$ and $\zeta_{ij}(H)$ play different roles. We will show that the factors $\chi_{ij}(H)$ inside the modulus in Eq. (6.6) lead to linear-in-$|H|$ enhancement of the superfluid stiffness $N_s(H)$ and critical temperature $T_c(H)$. On the other hand, the $\zeta_{ij}(H)$ phases produce quadratic-in-H corrections to physical quantities and so we neglect them in the following analysis. Thus, in this section we take for $J_{ij}(\mathbf{H})$ the simpler expression

$$J_{ij}(\mathbf{H}) = \left|A_{ij} - B_{ij} e^{i\chi_{ij}}\right| J_0 e^{-r_{ij}/L_T}. \tag{6.10}$$

We take $A_{ij} + B_{ij} = 1$ with A_{ij} uniformly distributed in $[0, 1]$ and χ_{ij} uniformly distributed in $[-\pi|\phi|, \pi|\phi|]$. Finally, J_0 is the characteristic energy scale of the non-exponential front factors in Eq. (6.5). Neglecting the variation in J_0 is a valid approximation because the disorder in the front factors is subleading compared to that of the exponent.

It is convenient to represent the Josephson couplings in logarithmic variables,

$$J_{ij} = J_0 \exp(-\xi_{ij}), \tag{6.11}$$

where $\xi_{ij} = \xi_{ij}^{(0)} + \delta\xi_{ij}$ with

$$\xi_{ij}^{(0)} = r_{ij}/L_T, \quad \delta\xi_{ij} = -\ln\left|A_{ij} - B_{ij} e^{i\chi_{ij}}\right|. \tag{6.12}$$

This decomposition highlights that the distribution of $\delta\xi_{ij}$ is much narrower than that of $\xi_{ij}^{(0)}$ in the $r_G \gg L_T$ limit.

To calculate the superfluid stiffness of the system at $H = 0$, we expand the Mattis Hamiltonian in Eq. (6.1) up to quadratic terms in θ_i. Calculating the superfluid stiffness is then equivalent to calculating the macroscopic conductance of a random resistor network where θ_i and $|J_{ij}|$ are analogous to voltages and conductances, respectively. In the $r_G \gg L_T$ regime, the $|J_{ij}|$ are broadly distributed and we can estimate N_s using percolation theory, as is well known in the context of hopping conductivity [37]. In this approach, we consider switching on couplings J_{ij} from strongest to weakest until the network of bonds percolates. The critical coupling $J_c \equiv J_0 \exp(-\xi_c)$ sets the scale of the macroscopic superfluid stiffness. In other words, the value of N_s is controlled by the percolating cluster with links where $0 < \xi_{ij} < \xi_c$.

In the zeroth approximation, where $\delta\xi_{ij} = 0$, we obtain

$$N_s^{(0)} = J_0 r_G^{2-d} \left(\frac{L_T}{r_c^{(0)}}\right)^{\nu} e^{-\frac{r_c^{(0)}}{L_T}} \tag{6.13}$$

where $r_c^{(0)} = L_T \xi_c^{(0)}$ and ν is the exponent governing the correlation radius of the percolating cluster. See Ref. [37] for details.

To calculate the magnetic field correction to the superfluid density, we use the perturbation theory of percolation developed in Ref. [37]: The first-order correction $\delta\xi_c$ to the percolation threshold ξ_c for typical $\delta\xi_{ij} \ll \xi_c^{(0)}$ is given by the average perturbation, $\delta\xi_c = \mathbb{E}[\delta\xi_{ij}]$. Thus

$$\begin{aligned}
\delta\xi_c(H) &= -\mathbb{E}\Big[\ln\left|A_{ij} - B_{ij}e^{i\chi_{ij}}\right|\Big] \\
&= -\int_{-\pi\phi}^{\pi\phi} \frac{\mathrm{d}\chi}{2\pi\phi} \int_0^1 \mathrm{d}A \ln\left|A - (1-A)e^{i\chi}\right| \\
&\sim 1 - \frac{\pi^2}{8}|\phi|.
\end{aligned} \tag{6.14}$$

As a result, the superfluid density is enhanced at small magnetic field $\phi \ll 1$:

$$\frac{\Delta N_s(H)}{N_s(0)} \equiv \frac{N_s(H) - N_s(0)}{N_s(0)} \sim \frac{\pi^2}{8}\frac{|H|S}{\Phi_0} \tag{6.15}$$

The perturbative treatment of the problem which leads to Eq. (6.15) is valid when the relevant $\delta\xi_{ij} \ll \xi_c$. On the other hand, as $\phi \to 0$, the main contribution to Eqs. (6.14) and (6.15) comes from inter-grain couplings with $|A_{ij} - B_{ij}| \to 0$, for which $\delta\xi_{ij}$ diverges logarithmically. The magnetic field suppresses the probability of such events. This means that Eqs. (6.14) and (6.15) are valid if $\phi > \exp(-\xi_c)$. In the opposite limit, at very small magnetic field, the correction to the superfluid stiffness $\Delta N_s(H)/N_s(0) \sim c\phi^2 > 0$ is quadratic. However, even in this regime, we expect that the magnetic field correction to

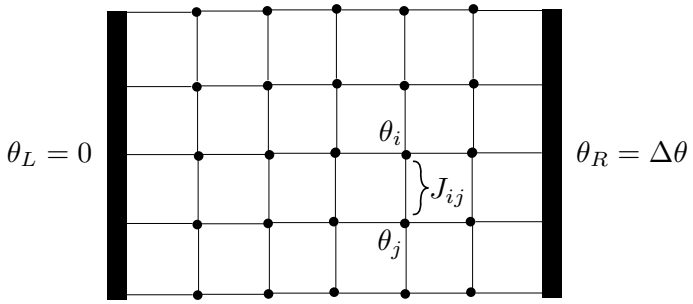

Figure 6.2: The lattice on which numerical calculations in the Mattis regime are carried out. Nearest-neighbor grains have random couplings J_{ij}. Two large superconducting leads are placed at either end, with $\theta_L = 0, \theta_R = \Delta\theta$. The system is periodic in the transverse direction.

the stiffness is still positive. Indeed, at $\phi_c \sim e^{-\xi_c}$ the linear and quadratic dependences should match. This gives us an estimate for the coefficient,

$$c \sim e^{\xi_c} \gg 1. \tag{6.16}$$

On the other hand, the conventional negative contributions to the magnetic field dependence of the superfluid density scale as $-a\phi^2$ with coefficient $a \sim O(1)$. Thus the magnetoenhancement discussed here dominates even for $\phi \lesssim e^{-\xi_c}$.

6.2.3 Numerical simulations

In order to verify the applicability of the perturbative analysis, we also study the Hamiltonian in Eq. (6.1) numerically in the Mattis regime. We carry out calculations on a regular square lattice of size $L \times L$ with Josephson couplings between nearest-neighbor grains as in Fig. 6.2. At the two boundaries in the x direction, the system is put in contact with a large superconducting reservoir at fixed phase. We use periodic boundary conditions in the y direction. The couplings take the form in Eq. (6.10), with $\xi_{ij} \equiv r_{ij}/L_T$ uniformly distributed in $[-W, W]$. The parameter W thus represents the typical distance between puddles in units of L_T.

We calculate the enhancement in N_S as a function of the dimensionless magnetic flux ϕ by considering the change in energy due to a small phase difference $\Delta\theta$. Since the Hamiltonian in the Mattis regime is essentially that of an XY ferromagnet, the ground state at $\Delta\theta = 0$ is having all $\theta_i = 0$. By continuity, all θ_i are small for $\Delta\theta \ll 1$, and we can write

$$H = \frac{1}{2} \sum_{ij} J_{ij}(\phi) \big(\theta_i - \theta_j\big)^2. \tag{6.17}$$

Denote the ground state for boundary condition $\Delta\theta$ by θ_i^*. The superfluid stiffness obeys

$$\frac{1}{2}\sum_{ij} J_{ij}(\phi)\big(\theta_i^* - \theta_j^*\big)^2 = \frac{1}{2}N_s(\phi)\Delta\theta^2. \tag{6.18}$$

Note that we can find θ_i^* by solving a linear equation: setting $\partial H/\partial\theta_i = 0$ gives

$$\sum_j J_{ij}(\phi)\big(\theta_i^* - \theta_j^*\big) = J_{iR}\Delta\theta. \tag{6.19}$$

We see that θ_i^* is proportional to $\Delta\theta$. Write $\theta_i^* = u_i\Delta\theta$. Then

$$N_s(\phi) = \sum_{ij} J_{ij}(\phi)\big(u_i - u_j\big)^2, \tag{6.20}$$

where u_i solves

$$\sum_j J_{ij}(\phi)\big(u_i - u_j\big) = J_{iR}. \tag{6.21}$$

It is straightforward to evaluate Eqs. (6.20) and (6.21) numerically. The main panel of Fig. 6.3 shows the resulting superfluid stiffness as a function of ϕ for representative values of W. Two regimes are clearly visible. For $\phi > \phi_c \sim e^{-\xi_c}$, the stiffness grows linearly with ϕ and even matches the prediction from the perturbative treatment, $\Delta N_S/N_S = \phi\pi^2/8$. For $\phi \ll \phi_c$, the curves cross over into quadratic behavior, as expected. The inset shows the crossover point ϕ_c versus W, where we find that ϕ_c is well-described by a curve e^{-pW} with $p = 0.4 \pm 0.1$. These results thus validate the understanding developed in Sec. 6.2.2.

Note that this numerical approach applies only in the Mattis regime, where we know that the ground state is ferromagnetic and thus that we can expand the Hamiltonian in $\theta_i - \theta_j$. In the glass regime, the ground state phase differences are no longer small. Furthermore, since the couplings are now frustrated, even finding the ground state is non-trivial. In Sec. 6.3, we instead study the glass regime in the high-temperature limit and find signatures of magnetoenhancement there, as we alluded to in Chap. 5.

6.2.4 The critical temperature

One can similarly estimate the change in the critical temperature T_c due to a magnetic field. At the mean-field level, all couplings J_{ij} greater than a given temperature T are "rigid", so that the phase on the grains connected by such couplings are locked. Therefore, the critical temperature may be found by determining when the set of rigid couplings defined by the condition

$$\frac{\hbar}{2e}|J_{ij}| > T_c(H) \tag{6.22}$$

percolates.

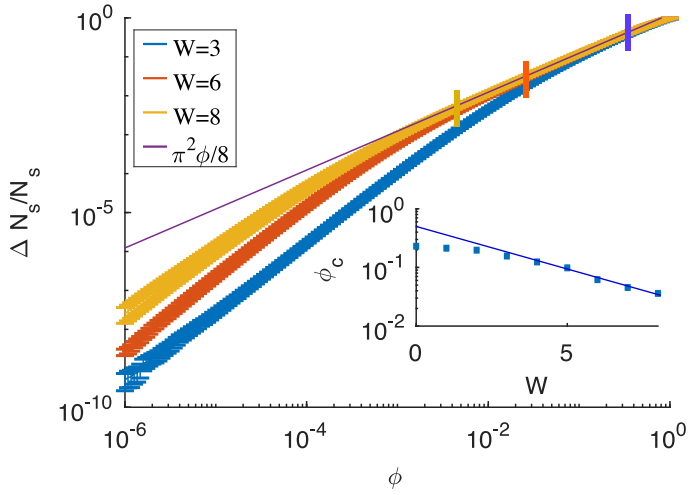

Figure 6.3: Relative enhancement of superconductivity $\Delta N_S/N_S$ as a function of dimensionless flux ϕ, for multiple disorder strengths W. The results are for a square lattice of linear dimension $L = 60$, averaged over 1000 disorder realizations per data point. Data for smaller sizes are indistinguishable. The line $\frac{\pi^2}{8}|\phi|$ is the perturbative prediction of Sec. 6.2.2, which should hold at large W over the range $\phi_c \sim e^{-\xi_c} < \phi < O(1)$. At smaller fields ϕ, the crossover to quadratic behavior is visible. The crossover point $\phi_c(W)$ is marked by vertical ticks. (Inset) The numerically extracted crossover point ϕ_c as a function of W. The straight line fit shows the exponential dependence expected at large W.

A similar procedure has been applied previously to calculate the critical temperature of disordered ferromagnets [152, 153]. The difference is that in the present case, $\xi_c \equiv r_c/L_T$ depends on temperature through L_T. Thus T_c is determined implicitly by the equation

$$T_c = \frac{\hbar}{2e} J_0 \, e^{-r_c/L_{T_c}}. \tag{6.23}$$

In the absence of the $\delta\xi_{ij}$, $r_c = r_c^{(0)}$ independent of temperature as previously discussed in Sec. 6.2.2. Including the $\delta\xi_{ij}$ then shifts r_c/L_T according to Eq. (6.14), thus the equation determining T_c is written

$$T_c = \frac{\hbar}{2e} J_0 \, e^{-r_c^{(0)}/L_{T_c} - 1 + \frac{\pi^2}{8}|\phi|}, \tag{6.24}$$

Expanding with respect to small ϕ, we obtain

$$\frac{T_c(H) - T_c(0)}{T_c(0)} \sim \frac{\pi^2}{4} \frac{L_{T_c(0)}}{r_c^{(0)}} \frac{|HS|}{\Phi_0}. \tag{6.25}$$

The above analysis has a mean-field character in that it neglects fluctuations of the phase between "rigid" couplings. However, we expect the conclusions to be correct in the strong-disorder limit ($W \gg L_T$), where all but a vanishing fraction of couplings in the percolating network are much stronger than the putative T_c. Indeed, the authors of Ref. [153] checked the validity of the percolation theory via Monte Carlo simulations, and found that T_c is given by Eq. (6.23) up to a factor of order 1.

This shows that the magnetoenhancement of T_c behaves analogously to the magnetoenhancement of N_s. Namely, the linear dependence on $|H|$ applies for fields larger than the previously mentioned exponentially small cutoff $\phi > e^{-\xi_c}$, but the change in T_c is still positive below the cutoff.

6.3 High-temperature magnetoenhancement

In the superconducting glass regime ($r_G \lesssim R$), the couplings J_{ij} in Eq. (6.1) have random signs in the absence of a magnetic field. The frustration thus induced makes the theoretical problem difficult at low temperature. As with spin glasses, most physical properties are out-of-equilibrium and time-dependent. It is not even clear how to define the superfluid density in general. Therefore, in this section we restrict ourselves to the case of high temperatures $T \gg (\hbar/2e)|J_{ij}|$, where the system is in the normal state, and show that the superconducting correlation function,

$$A_{kl} = \left\langle e^{i(\theta_k - \theta_l)} \right\rangle = \mathrm{Tr}\left[e^{i(\theta_k - \theta_l)} \frac{e^{-\beta H}}{Z} \right], \tag{6.26}$$

is enhanced by a magnetic field. Here, the Hamiltonian H (not to be confused with the magnetic field) is given by Eq. (6.1), $\beta = 1/T$, and Z is the partition function.

This correlation function controls the critical current in a junction composed of two S-wave bulk superconductors forming a sandwich around a granular D-wave composite (see Fig. 6.1) in the regime where the temperature is below the critical temperature of the S-wave leads.

The sign of the coupling J_{ij} in the glass regime depends on the relative orientation of the order parameter between the two grains. We model this dependence by including a factor $\cos 2(\Theta_i - \Theta_j)$ in Eq. (6.6), where Θ_i is the orientation of the positive node of the order parameter on grain i. This factor respects the D-wave symmetry of the grains: it retains its sign if either grain rotates by π and changes sign if either grain rotates by $\pi/2$. Furthermore, since the enhancement of the correlation function relies on long-distance universal behavior, as discussed below, we neglect the variation in all other quantities affecting J_{ij} for simplicity. This includes the relative phases χ_{ij} in Eq. (6.6). Thus we model the Josephson couplings as

$$J_{ij} = J_0\, e^{i\zeta_{ij}} \cos 2\big(\Theta_i - \Theta_j\big), \tag{6.27}$$

where $\zeta_{ij} = \mathbf{A}(\mathbf{r}) \cdot \mathbf{r}_{ij}$ and Θ_i is uniformly distributed in $[-\pi, \pi]$.

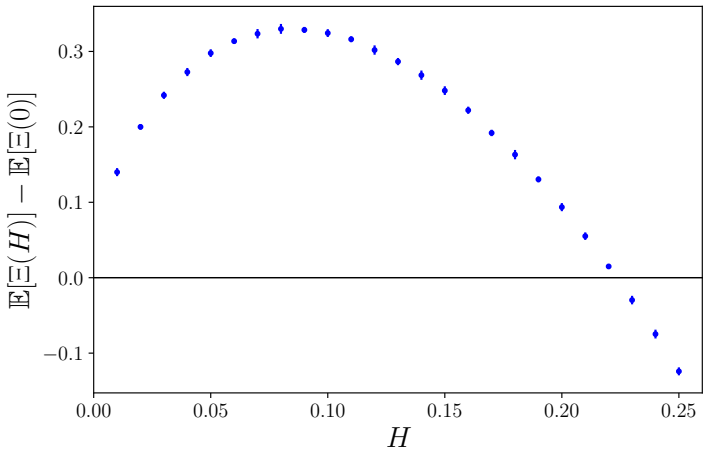

Figure 6.4: The disorder-averaged change in correlation length as a function of magnetic field H.

The standard high-temperature expansion of Eq. (6.26) gives the correlation function as a sum over paths Γ from grain k to grain l:

$$A_{kl} = \sum_{\Gamma} A_{\Gamma}, \quad A_{\Gamma} \equiv \prod_{\langle ij\rangle \in \Gamma} \left(\frac{\pi\hbar\beta}{2e} J_{ij} \right). \tag{6.28}$$

The product over $\langle ij\rangle \in \Gamma$ runs over all links along path Γ. Furthermore, since $(\hbar\beta/e)|J_{ij}| \ll 1$, the leading-order terms in the path sum Eq. (6.28) correspond to *directed* paths. See Fig. 6.1 for a qualitative example of such directed paths. In the high-temperature regime, the correlation function decays exponentially at large distance: $\ln|A_{kl}| \sim -r/\Xi(H)$.

It follows from Eq. (6.28) that

$$\frac{1}{\Xi(H)} = \ln\frac{2e}{\pi\hbar\beta J_0} - \lim_{r\to\infty}\frac{1}{r}\ln\left|\sum_{\Gamma}\prod_{\langle ij\rangle\in\Gamma} e^{i\zeta_{ij}}\cos 2\big(\Theta_i - \Theta_j\big)\right|. \tag{6.29}$$

We have conducted numerical simulations of this model on a 2D square lattice in a uniform perpendicular magnetic field. The average change in correlation length, $\mathbb{E}[\Xi(H)] - \mathbb{E}[\Xi(0)]$, is plotted as a function of H in Fig. 6.4. At low magnetic field, Ξ increases in a non-analytic way:

$$\frac{\Xi(H) - \Xi(0)}{\Xi(0)} \sim \left(\frac{\Xi(0)^2\,|H|}{\Phi_0}\right)^{\alpha}, \tag{6.30}$$

with $\alpha = 0.59 \pm 0.03$. This non-analyticity derives from the statistics of directed paths in disordered media. Indeed, as we have discussed in depth in Chap. 5, the

model defined by Eqs. (6.27) and (6.28)) belongs to the same universality class as that used to describe negative magnetoresistance in hopping conductivity [108, 112, 121, 127]. Thus the exponents at small field are the same. The universality of the long-distance behavior justifies our use of Eq. (6.27), since the exact microscopic details do not matter.

However, at short distances, the model given by Eq. (6.27) has much more constructive interference than in hopping conduction problems, because the sign of the paths going to grain i are all correlated with the orientation Θ_i. Thus at large field, where the magnetic length becomes comparable to the "sign disordering length" of Eq. (6.28) (see Chap. 5), the magneto-correction to Ξ becomes negative. We see this in Fig. 6.4.

To summarize, we have shown that in certain parametric regimes, the application of a magnetic field leads to non-analytic enhancement of both the superfluid stiffness and the critical temperature in disordered D-wave composites. Heuristically, the magnetoenhancement stems from the suppression of destructive interference between Cooper pairs carrying positive and negative amplitudes, although the length scale on which this suppression takes place varies between the cases which we have considered: it is short compared to the inter-grain spacing in the Mattis regime, and large in the glass regime. This picture does not rely on any specific microsopic model, and we view these results as proof of principle for the magnetoenhancement of superconductivity.

Bibliography

[1] The Nobel Prize in Physics 1989. http://www.nobelprize.org/nobel_prizes/physics/laureates/1989/.

[2] The Nobel Prize in Physics 1997. http://www.nobelprize.org/nobel_prizes/physics/laureates/1997/.

[3] The Nobel Prize in Physics 2001. http://www.nobelprize.org/nobel_prizes/physics/laureates/2001/.

[4] The Nobel Prize in Physics 2012. http://www.nobelprize.org/nobel_prizes/physics/laureates/2012/.

[5] Michael Schreiber, Sean S. Hodgman, Pranjal Bordia, Henrik P. Lüschen, Mark H. Fischer, Ronen Vosk, Ehud Altman, Ulrich Schneider, and Immanuel Bloch. Observation of many-body localization of interacting fermions in a quasirandom optical lattice. *Science*, 349(6250):842–845, 2015.

[6] S. S. Kondov, W. R. McGehee, W. Xu, and B. DeMarco. Disorder-induced localization in a strongly correlated atomic hubbard gas. *Phys. Rev. Lett.*, 114:083002, Feb 2015.

[7] J. Smith, A. Lee, P. Richerme, B. Neyenhuis, P. W. Hess, P. Hauke, M. Heyl, D. A. Huse, and C. Monroe. Many-body localization in a quantum simulator with programmable random disorder. *Nat Phys*, 12(10):907–911, 10 2016.

[8] Martin Gärttner, Justin G. Bohnet, Arghavan Safavi-Naini, Michael L. Wall, John J. Bollinger, and Ana Maria Rey. Measuring out-of-time-order correlations and multiple quantum spectra in a trapped-ion quantum magnet. *Nature Physics*, 13:781 EP –, 05 2017.

[9] J. Zhang, G. Pagano, P. W. Hess, A. Kyprianidis, P. Becker, H. Kaplan, A. V. Gorshkov, Z. X. Gong, and C. Monroe. Observation of a many-body dynamical phase transition with a 53-qubit quantum simulator. *Nature*, 551:601 EP –, 11 2017.

[10] Ken Xuan Wei, Chandrasekhar Ramanathan, and Paola Cappellaro. Exploring localization in nuclear spin chains. *Phys. Rev. Lett.*, 120:070501, Feb 2018.

[11] J. M. Deutsch. Quantum statistical mechanics in a closed system. *Phys. Rev. A*, 43:2046–2049, Feb 1991.

[12] Mark Srednicki. Chaos and quantum thermalization. *Phys. Rev. E*, 50:888–901, Aug 1994.

[13] Luca D'Alessio, Yariv Kafri, Anatoli Polkovnikov, and Marcos Rigol. From quantum chaos and eigenstate thermalization to statistical mechanics and thermodynamics. *Advances in Physics*, 65(3):239–362, 2016.

[14] Mark Srednicki. Thermal fluctuations in quantized chaotic systems. *Journal of Physics A: Mathematical and General*, 29(4):L75, 1996.

[15] Mark Srednicki. The approach to thermal equilibrium in quantized chaotic systems. *Journal of Physics A: Mathematical and General*, 32(7):1163, 1999.

[16] Marcos Rigol, Vanja Dunjko, and Maxim Olshanii. Thermalization and its mechanism for generic isolated quantum systems. *Nature*, 452:854 EP –, 04 2008.

[17] Ehsan Khatami, Marcos Rigol, Armando Relaño, and Antonio M. García-García. Quantum quenches in disordered systems: Approach to thermal equilibrium without a typical relaxation time. *Phys. Rev. E*, 85:050102, May 2012.

[18] Hyungwon Kim, Tatsuhiko N. Ikeda, and David A. Huse. Testing whether all eigenstates obey the eigenstate thermalization hypothesis. *Phys. Rev. E*, 90:052105, Nov 2014.

[19] Adam M. Kaufman, M. Eric Tai, Alexander Lukin, Matthew Rispoli, Robert Schittko, Philipp M. Preiss, and Markus Greiner. Quantum thermalization through entanglement in an isolated many-body system. *Science*, 353(6301):794–800, 2016.

[20] Rubem Mondaini, Keith R. Fratus, Mark Srednicki, and Marcos Rigol. Eigenstate thermalization in the two-dimensional transverse field ising model. *Phys. Rev. E*, 93:032104, Mar 2016.

[21] Anatoly Dymarsky, Nima Lashkari, and Hong Liu. Subsystem eigenstate thermalization hypothesis. *Phys. Rev. E*, 97:012140, Jan 2018.

[22] M. L. Mehta. *Random Matrices and the Statistical Theory of Energy Levels*. Academic Press, 1967.

[23] Norbert Rosenzweig and Charles E. Porter. "repulsion of energy levels" in complex atomic spectra. *Phys. Rev.*, 120:1698–1714, Dec 1960.

[24] L. P. Gorkov and G. M. Eliashberg. Minute metallic particles in an electromagnetic field. *JETP*, 21(5):940, 1965.

[25] H. S. Camarda and P. D. Georgopulos. Statistical behavior of atomic energy levels: Agreement with random-matrix theory. *Phys. Rev. Lett.*, 50:492–495, Feb 1983.

[26] O. Bohigas, M. J. Giannoni, and C. Schmit. Characterization of chaotic quantum spectra and universality of level fluctuation laws. *Phys. Rev. Lett.*, 52:1–4, Jan 1984.

[27] C. W. J. Beenakker. Brownian-motion model for parametric correlations in the spectra of disordered metals. *Phys. Rev. Lett.*, 70:4126–4129, Jun 1993.

[28] Arijeet Pal and David A. Huse. Many-body localization phase transition. *Phys. Rev. B*, 82:174411, Nov 2010.

[29] David J. Luitz, Nicolas Laflorencie, and Fabien Alet. Many-body localization edge in the random-field heisenberg chain. *Phys. Rev. B*, 91:081103, Feb 2015.

[30] Maksym Serbyn and Joel E. Moore. Spectral statistics across the many-body localization transition. *Phys. Rev. B*, 93:041424, Jan 2016.

[31] Vadim Oganesyan and David A. Huse. Localization of interacting fermions at high temperature. *Phys. Rev. B*, 75:155111, Apr 2007.

[32] Lea F. Santos and Marcos Rigol. Onset of quantum chaos in one-dimensional bosonic and fermionic systems and its relation to thermalization. *Phys. Rev. E*, 81:036206, Mar 2010.

[33] Corinna Kollath, Guillaume Roux, Giulio Biroli, and Andreas M Läuchli. Statistical properties of the spectrum of the extended bose–hubbard model. *Journal of Statistical Mechanics: Theory and Experiment*, 2010(08):P08011, 2010.

[34] D.J. Thouless. Electrons in disordered systems and the theory of localization. *Physics Reports*, 13(3):93 – 142, 1974.

[35] Patrick A. Lee and T. V. Ramakrishnan. Disordered electronic systems. *Rev. Mod. Phys.*, 57:287–337, Apr 1985.

[36] E. Abrahams. *50 Years of Anderson Localization*. World Scientific, 2010.

[37] A. L. Efros and B. I. Shklovskii. *Electronic Properties of Doped Semiconductors*. Springer Series in Solid-State Sciences. Springer-Verlag, 1984.

[38] P. W. Anderson. Absence of diffusion in certain random lattices. *Phys. Rev.*, 109:1492–1505, Mar 1958.

[39] R Abou-Chacra, D J Thouless, and P W Anderson. A selfconsistent theory of localization. *Journal of Physics C: Solid State Physics*, 6(10):1734, 1973.

[40] E. Abrahams, P. W. Anderson, D. C. Licciardello, and T. V. Ramakrishnan. Scaling theory of localization: Absence of quantum diffusion in two dimensions. *Phys. Rev. Lett.*, 42:673–676, Mar 1979.

[41] J T Edwards and D J Thouless. Numerical studies of localization in disordered systems. *Journal of Physics C: Solid State Physics*, 5(8):807, 1972.

[42] D. C. Licciardello and D. J. Thouless. Constancy of minimum metallic conductivity in two dimensions. *Phys. Rev. Lett.*, 35:1475–1478, Nov 1975.

[43] A. MacKinnon and B. Kramer. One-parameter scaling of localization length and conductance in disordered systems. *Phys. Rev. Lett.*, 47:1546–1549, Nov 1981.

[44] A. De Luca, B. L. Altshuler, V. E. Kravtsov, and A. Scardicchio. Anderson localization on the bethe lattice: Nonergodicity of extended states. *Phys. Rev. Lett.*, 113:046806, Jul 2014.

[45] Francesca Pietracaprina, Valentina Ros, and Antonello Scardicchio. Forward approximation as a mean-field approximation for the anderson and many-body localization transitions. *Phys. Rev. B*, 93:054201, Feb 2016.

[46] Juliette Billy, Vincent Josse, Zhanchun Zuo, Alain Bernard, Ben Hambrecht, Pierre Lugan, David Clément, Laurent Sanchez-Palencia, Philippe Bouyer, and Alain Aspect. Direct observation of anderson localization of matter waves in a controlled disorder. *Nature*, 453:891 EP –, 06 2008.

[47] Giacomo Roati, Chiara D'Errico, Leonardo Fallani, Marco Fattori, Chiara Fort, Matteo Zaccanti, Giovanni Modugno, Michele Modugno, and Massimo Inguscio. Anderson localization of a non-interacting bose–einstein condensate. *Nature*, 453:895 EP –, 06 2008.

[48] G. Semeghini, M. Landini, P. Castilho, S. Roy, G. Spagnolli, A. Trenkwalder, M. Fattori, M. Inguscio, and G. Modugno. Measurement of the mobility edge for 3d anderson localization. *Nature Physics*, 11:554 EP –, 06 2015.

[49] V. Ros, M. Müller, and A. Scardicchio. Integrals of motion in the many-body localized phase. *Nuclear Physics B*, 891:420 – 465, 2015.

[50] Boris L. Altshuler, Yuval Gefen, Alex Kamenev, and Leonid S. Levitov. Quasiparticle lifetime in a finite system: A nonperturbative approach. *Phys. Rev. Lett.*, 78:2803–2806, Apr 1997.

[51] D.M. Basko, I.L. Aleiner, and B.L. Altshuler. Metal–insulator transition in a weakly interacting many-electron system with localized single-particle states. *Annals of Physics*, 321(5):1126 – 1205, 2006.

[52] John Z. Imbrie. On many-body localization for quantum spin chains. *Journal of Statistical Physics*, 163(5):998–1048, 2016.

[53] Timothy C. Berkelbach and David R. Reichman. Conductivity of disordered quantum lattice models at infinite temperature: Many-body localization. *Phys. Rev. B*, 81:224429, Jun 2010.

[54] Jens H. Bardarson, Frank Pollmann, and Joel E. Moore. Unbounded growth of entanglement in models of many-body localization. *Phys. Rev. Lett.*, 109:017202, Jul 2012.

[55] A. De Luca and A. Scardicchio. Ergodicity breaking in a model showing many-body localization. *EPL (Europhysics Letters)*, 101(3):37003, 2013.

[56] Shankar Iyer, Vadim Oganesyan, Gil Refael, and David A. Huse. Many-body localization in a quasiperiodic system. *Phys. Rev. B*, 87:134202, Apr 2013.

[57] Jonas A. Kjäll, Jens H. Bardarson, and Frank Pollmann. Many-body localization in a disordered quantum ising chain. *Phys. Rev. Lett.*, 113:107204, Sep 2014.

[58] N. Y. Yao, C. R. Laumann, S. Gopalakrishnan, M. Knap, M. Müller, E. A. Demler, and M. D. Lukin. Many-body localization in dipolar systems. *Phys. Rev. Lett.*, 113:243002, Dec 2014.

[59] Maksym Serbyn, Z. Papić, and Dmitry A. Abanin. Local conservation laws and the structure of the many-body localized states. *Phys. Rev. Lett.*, 111:127201, Sep 2013.

[60] David A. Huse, Rahul Nandkishore, and Vadim Oganesyan. Phenomenology of fully many-body-localized systems. *Phys. Rev. B*, 90:174202, Nov 2014.

[61] M. Mézard, G. Parisi, and M.Á. Virasoro. *Spin Glass Theory and Beyond*. Lecture Notes in Physics Series. World Scientific Publishing Company, Incorporated, 1987.

[62] R. Monasson. *Introduction to phase transitions in random optimization problems*, volume 85 of *Les Houches*, pages 1 – 65. Elsevier, 2007.

[63] M. Mézard and A. Montanari. *Information, Physics, and Computation*. Oxford Graduate Texts. OUP Oxford, 2009.

[64] C. Moore and S. Mertens. *The Nature of Computation*. Oxford University Press, 2011.

[65] Jean-Philippe Bouchaud, Leticia F. Cugliandolo, Jorge Kurchan, and Marc Mezard. *Out of Equilibrium Dynamics in Spin-Glasses and Other Glassy Systems*, pages 161–223. World Scientific, 2011.

[66] M. E. J. Newman and G. T. Barkema. *Monte Carlo Methods in Statistical Physics*. Clarendon Press, 1999.

[67] M. Mezard, G. Parisi, and R. Zecchina. Analytic and algorithmic solution of random satisfiability problems. *Science*, 297(5582):812–815, 2002.

[68] David J. Earl and Michael W. Deem. Parallel tempering: Theory, applications, and new perspectives. *Phys. Chem. Chem. Phys.*, 7:3910–3916, 2005.

[69] G. Biroli, R. Monasson, and M. Weigt. A variational description of the ground state structure in random satisfiability problems. *The European Physical Journal B - Condensed Matter and Complex Systems*, 14(3):551–568, Apr 2000.

[70] R. Mulet, A. Pagnani, M. Weigt, and R. Zecchina. Coloring random graphs. *Phys. Rev. Lett.*, 89:268701, Dec 2002.

[71] M. Mézard, F. Ricci-Tersenghi, and R. Zecchina. Two solutions to diluted p-spin models and xorsat problems. *Journal of Statistical Physics*, 111:505, 2003.

[72] M. Mézard, T. Mora, and R. Zecchina. Clustering of solutions in the random satisfiability problem. *Phys. Rev. Lett.*, 94:197205, May 2005.

[73] Jack Raymond, Andrea Sportiello, and Lenka Zdeborová. Phase diagram of the 1-in-3 satisfiability problem. *Phys. Rev. E*, 76:011101, Jul 2007.

[74] Lenka Zdeborova and Florent Krzakala. Phase transitions in the coloring of random graphs. *Phys. Rev. E*, 76:031131, Sep 2007.

[75] B. Derrida. Random-energy model: Limit of a family of disordered models. *Phys. Rev. Lett.*, 45:79–82, Jul 1980.

[76] D.J. Gross and M. Mezard. The simplest spin glass. *Nuclear Physics B*, 240(4):431 – 452, 1984.

[77] E. Gardner. Spin glasses with p-spin interactions. *Nuclear Physics B*, 257:747 – 765, 1985.

[78] V. Bapst, L. Foini, F. Krzakala, G. Semerjian, and F. Zamponi. The quantum adiabatic algorithm applied to random optimization problems: The quantum spin glass perspective. *Physics Reports*, 523(3):127 – 205, 2013.

[79] T. R. Kirkpatrick and D. Thirumalai. p -spin-interaction spin-glass models: Connections with the structural glass problem. *Phys. Rev. B*, 36:5388–5397, Oct 1987.

[80] G. Biroli and J. P. Bouchaud. *The Random First-Order Transition Theory of Glasses*. John Wiley & Sons, Inc., 2012.

[81] A.B. Finnila, M.A. Gomez, C. Sebenik, C. Stenson, and J.D. Doll. Quantum annealing: A new method for minimizing multidimensional functions. *Chemical Physics Letters*, 219(5):343 – 348, 1994.

[82] Edward Farhi, Jeffrey Goldstone, Sam Gutmann, Joshua Lapan, Andrew Lundgren, and Daniel Preda. A quantum adiabatic evolution algorithm applied to random instances of an np-complete problem. *Science*, 292(5516):472–475, 2001.

[83] C.R. Laumann, R. Moessner, A. Scardicchio, and S.L. Sondhi. Quantum annealing: The fastest route to quantum computation? *The European Physical Journal Special Topics*, 224(1):75–88, Feb 2015.

[84] A. Messiah. *Quantum Mechanics, vol. 2*. Elsevier Science B. V., 1961.

[85] Thomas Jörg, Florent Krzakala, Jorge Kurchan, and A. C. Maggs. Simple glass models and their quantum annealing. *Phys. Rev. Lett.*, 101:147204, Oct 2008.

[86] Boris Altshuler, Hari Krovi, and Jérémie Roland. Anderson localization makes adiabatic quantum optimization fail. *Proceedings of the National Academy of Sciences*, 107(28):12446–12450, 2010.

[87] A. P. Young, S. Knysh, and V. N. Smelyanskiy. First-order phase transition in the quantum adiabatic algorithm. *Phys. Rev. Lett.*, 104:020502, Jan 2010.

[88] Edward Farhi, David Gosset, Itay Hen, A. W. Sandvik, Peter Shor, A. P. Young, and Francesco Zamponi. Performance of the quantum adiabatic algorithm on random instances of two optimization problems on regular hypergraphs. *Phys. Rev. A*, 86:052334, Nov 2012.

[89] C. L. Baldwin and C. R. Laumann. Quantum algorithm for energy matching in hard optimization problems. *Phys. Rev. B*, 97:224201, Jun 2018.

[90] C. L. Baldwin, C. R. Laumann, A. Pal, and A. Scardicchio. The many-body localized phase of the quantum random energy model. *Phys. Rev. B*, 93:024202, Jan 2016.

[91] C. L. Baldwin, C. R. Laumann, A. Pal, and A. Scardicchio. Clustering of nonergodic eigenstates in quantum spin glasses. *Phys. Rev. Lett.*, 118:127201, Mar 2017.

[92] C. R. Laumann, A. Pal, and A. Scardicchio. Many-body mobility edge in a mean-field quantum spin glass. *Phys. Rev. Lett.*, 113:200405, Nov 2014.

[93] Yadin Y. Goldschmidt. Solvable model of the quantum spin glass in a transverse field. *Phys. Rev. B*, 41:4858–4861, Mar 1990.

[94] David A. Huse, Rahul Nandkishore, Francesca Pietracaprina, Valentina Ros, and Antonello Scardicchio. Localized systems coupled to small baths: From anderson to zeno. *Phys. Rev. B*, 92:014203, Jul 2015.

[95] J. J. Sakurai and J. Napolitano. *Modern Quantum Mechanics*. Addison-Wesley, 2011.

[96] M. W. Johnson, M. H. S. Amin, S. Gildert, T. Lanting, F. Hamze, N. Dickson, R. Harris, A. J. Berkley, J. Johansson, P. Bunyk, E. M. Chapple, C. Enderud, J. P. Hilton, K. Karimi, E. Ladizinsky, N. Ladizinsky, T. Oh, I. Perminov, C. Rich, M. C. Thom, E. Tolkacheva, C. J. S. Truncik, S. Uchaikin, J. Wang, B. Wilson, and G. Rose. Quantum annealing with manufactured spins. *Nature*, 473(7346):194–198, 05 2011.

[97] Sergio Boixo, Troels F. Ronnow, Sergei V. Isakov, Zhihui Wang, David Wecker, Daniel A. Lidar, John M. Martinis, and Matthias Troyer. Evidence for quantum annealing with more than one hundred qubits. *Nat Phys*, 10(3):218–224, 03 2014.

[98] Sergey Bravyi, David P. DiVincenzo, and Daniel Loss. Schrieffer–wolff transformation for quantum many-body systems. *Annals of Physics*, 326(10):2793 – 2826, 2011.

[99] I. Kh. Zharekeshev and B. Kramer. Scaling of level statistics at the disorder-induced metal-insulator transition. *Phys. Rev. B*, 51:17239–17242, Jun 1995.

[100] J. Kurchan, G.Parisi, and M.A. Virasoro. Barriers and metastable states as saddle points in the replica approach. *J. Phys. I France*, 3(8):1819–1838, 1993.

[101] Silvio Franz and Giorgio Parisi. Recipes for metastable states in spin glasses. *J. Phys. I France*, 5(11):1401–1415, 1995.

[102] Silvio Franz and Giorgio Parisi. Phase diagram of coupled glassy systems: A mean-field study. *Phys. Rev. Lett.*, 79:2486–2489, Sep 1997.

[103] H. Sompolinsky and Annette Zippelius. Dynamic theory of the spin-glass phase. *Phys. Rev. Lett.*, 47:359–362, Aug 1981.

[104] V Dobrosavljevic and D Thirumalai. 1/p expansion for a p-spin interaction spin-glass model in a transverse field. *Journal of Physics A: Mathematical and General*, 23(15):L767, 1990.

[105] M. A. Nielsen and I. L. Chuang. *Quantum Computation and Quantum Information*. Cambridge University Press, 2000.

[106] K. H. Fischer and J. A. Hertz. *Spin Glasses*. Cambridge University Press, 1991.

[107] C. L. Baldwin, C. R. Laumann, and B. Spivak. Sign phase transition in the problem of interfering directed paths. *Phys. Rev. B*, 97:014203, Jan 2018.

[108] B. I. Shklovskii and B. Z. Spivak. *Hopping Transport in Solids*, chapter 9. Elsevier Science Publishers B.V., 1991.

[109] Mehran Kardar. *Statistical Physics of Fields*. Cambridge University Press, 2007.

[110] B. Spivak, P. Oreto, and S. A. Kivelson. Theory of quantum metal to superconductor transitions in highly conducting systems. *Phys. Rev. B*, 77:214523, Jun 2008.

[111] S. A. Kivelson and B. Spivak. Macroscopic character of composite high-temperature superconducting wires. *Phys. Rev. B*, 92:184502, Nov 2015.

[112] V. L. Nguyen, B. Spivak, and B. I. Shklovskii. Tunnel hopping in disordered systems. *Sov. Phys. JETP*, 89:1770 – 1784, 1985.

[113] Y. Shapir and X.-R. Wang. Absence of h/e periodicity of the aharonov-bohm oscillations in square metallic lattices. *EPL (Europhysics Letters)*, 4(10):1165, 1987.

[114] Ernesto Medina, Mehran Kardar, Yonathan Shapir, and Xiang Rong Wang. Interference of directed paths in disordered systems. *Phys. Rev. Lett.*, 62:941–944, Feb 1989.

[115] Ernesto Medina and Mehran Kardar. Quantum interference effects for strongly localized electrons. *Phys. Rev. B*, 46:9984–10006, Oct 1992.

[116] S Roux and A Coniglio. Interference of directed paths. *Journal of Physics A: Mathematical and General*, 27(16):5467, 1994.

[117] V. Lien Nguyen and Arturo D. Gamietea. Crossover in tunneling hops in systems of strongly localized electrons. *Phys. Rev. B*, 53:7932–7936, Mar 1996.

[118] B. Spivak, S. Feng, and F. Zeng. Sign phase transition and directed paths in random media. *JETP Letters*, 64(4):312, 1996.

[119] Eduardo G. Aponte and Ernesto Medina. Directed paths on hierarchical lattices with random sign weights. *Phys. Rev. E*, 58:4246–4253, Oct 1998.

[120] Hyungwon Kim and David A. Huse. Interfering directed paths and the sign phase transition. *Phys. Rev. B*, 83:052405, Feb 2011.

[121] L. Ioffe and B. Spivak. Giant magnetoresistance in the variable-range hopping regime. *Journal of Experimental and Theoretical Physics*, 117(3):551 – 569, 2013.

[122] B. I. Shklovskii. Variable-range hopping conductivity in a strong magnetic field. *JETP Letters*, 36(2):43, 1982.

[123] B. I. Shklovskii and A. L. Efros. Tunnel transparency of disordered systems in a magnetic field. *JETP*, 57(2):470, 1982.

[124] B. I. Shklovskii and B. Z. Spivak. Effect of impurity scattering of a tunneling electron on variable-range hopping conduction. *Journal of Statistical Physics*, 38(1):267–272, 1985.

[125] U. Sivan, O. Entin-Wohlman, and Y. Imry. Orbital magnetoconductance in the variable-range˘hopping regime. *Phys. Rev. Lett.*, 60:1566–1569, Apr 1988.

[126] Ernesto Medina, Mehran Kardar, Yonathan Shapir, and Xiang Rong Wang. Magnetic-field effects on strongly localized electrons. *Phys. Rev. Lett.*, 64:1816–1819, Apr 1990.

[127] Hui Lin Zhao, Boris Z. Spivak, Martin P. Gelfand, and Shechao Feng. Negative magnetoresistance in variable-range-hopping conduction. *Phys. Rev. B*, 44:10760–10767, Nov 1991.

[128] Anirban Gangopadhyay, Victor Galitski, and Markus Müller. Magnetoresistance of an anderson insulator of bosons. *Phys. Rev. Lett.*, 111:026801, Jul 2013.

[129] Daniel S. Fisher and David A. Huse. Directed paths in a random potential. *Phys. Rev. B*, 43:10728–10742, May 1991.

[130] Timothy Halpin-Healy and Yi-Cheng Zhang. Kinetic roughening phenomena, stochastic growth, directed polymers and all that. aspects of multidisciplinary statistical mechanics. *Physics Reports*, 254(4):215 – 414, 1995.

[131] Leticia F. Cugliandolo. Topics in coarsening phenomena. *Physica A: Statistical Mechanics and its Applications*, 389(20):4360 – 4373, 2010.

[132] K. Binder. Critical properties from monte carlo coarse graining and renormalization. *Phys. Rev. Lett.*, 47:693–696, Aug 1981.

[133] Hui Shao, Wenan Guo, and Anders W. Sandvik. Quantum criticality with two length scales. *Science*, 352(6282):213–216, 2016.

[134] N. F. Mott. *Metal-Insulator Transitions*. Taylor & Francis, 1990.

[135] Pierre Le Doussal and A. Brooks Harris. Location of the ising spin-glass multicritical point on nishimori's line. *Phys. Rev. Lett.*, 61:625–628, Aug 1988.

[136] K. Hukushima. Random fixed point of three-dimensional random-bond ising models. *Journal of the Physical Society of Japan*, 69(3):631–634, 2000.

[137] L. A. Fernandez, V. Martin-Mayor, S. Perez-Gaviro, A. Tarancon, and A. P. Young. Phase transition in the three dimensional heisenberg spin glass: Finite-size scaling analysis. *Phys. Rev. B*, 80:024422, Jul 2009.

[138] Martin Hasenbusch, Francesco Parisen Toldin, Andrea Pelissetto, and Ettore Vicari. Critical behavior of the three-dimensional $\pm j$ ising model at the paramagnetic-ferromagnetic transition line. *Phys. Rev. B*, 76:094402, Sep 2007.

[139] Dao Xuan Viet and Hikaru Kawamura. Monte carlo studies of chiral and spin ordering of the three-dimensional heisenberg spin glass. *Phys. Rev. B*, 80:064418, Aug 2009.

[140] Giacomo Ceccarelli, Andrea Pelissetto, and Ettore Vicari. Ferromagnetic-glassy transitions in three-dimensional ising spin glasses. *Phys. Rev. B*, 84:134202, Oct 2011.

[141] Limei Xu, Pradeep Kumar, S. V. Buldyrev, S. H. Chen, P. H. Poole, F. Sciortino, and H. E. Stanley. Relation between the widom line and the dynamic crossover in systems with a liquid-liquid phase transition. *Proceedings of the National Academy of Sciences of the United States of America*, 102(46):16558–16562, 2005.

[142] G. G. Simeoni, T. Bryk, F. A. Gorelli, M. Krisch, G. Ruocco, M. Santoro, and T. Scopigno. The widom line as the crossover between liquid-like and gas-like behaviour in supercritical fluids. *Nat Phys*, 6(7):503–507, 07 2010.

[143] Hidetoshi Nishimori. Internal energy, specific heat and correlation function of the bond-random ising model. *Progress of Theoretical Physics*, 66(4):1169–1181, 1981.

[144] Mauro Schiulaz, Christopher L. Baldwin, Chris R. Laumann, and Boris Z. Spivak. Magnetoenhancement of superconductivity in composite d-wave superconductors. *Phys. Rev. B*, 98:094508, Sep 2018.

[145] A. A. Abrikosov, L. P. Gorkov, and I. E. Dzyaloshinski. *Methods of Quantum Field Theory in Statistical Physics*. Dover Publications, 1963.

[146] D. J. Van Harlingen. Phase-sensitive tests of the symmetry of the pairing state in the high-temperature superconductors¯evidence for $d_{x^2-y^2}$ symmetry. *Rev. Mod. Phys.*, 67:515–535, Apr 1995.

[147] C. C. Tsuei and J. R. Kirtley. Pairing symmetry in cuprate superconductors. *Rev. Mod. Phys.*, 72:969–1016, Oct 2000.

[148] B. Spivak, P. Oreto, and S.A. Kivelson. d-wave to s-wave to normal metal transitions in disordered superconductors. *Physica B: Condensed Matter*, 404(3):462 – 465, 2009.

[149] Klaus D. Usadel. Generalized diffusion equation for superconducting alloys. *Phys. Rev. Lett.*, 25:507–509, Aug 1970.

[150] Y. Tanaka, Yu. V. Nazarov, A. A. Golubov, and S. Kashiwaya. Theory of charge transport in diffusive normal metal/unconventional singlet superconductor contacts. *Phys. Rev. B*, 69:144519, Apr 2004.

[151] D.C. Mattis. Solvable spin systems with random interactions. *Physics Letters A*, 56(5):421 – 422, 1976.

[152] I.Ya. Korenblit, E.F. Shender, and B.I. Shklovsky. Percolation approach to the phase transition in very dilute ferromagnetic alloys. *Physics Letters A*, 46(4):275 – 276, 1973.

[153] A. Kaminski, V. M. Galitski, and S. Das Sarma. Ferromagnetic and random spin ordering in dilute magnetic semiconductors. *Phys. Rev. B*, 70:115216, Sep 2004.